The Field Induced Melting of Charge Order in the Manganites

By

Anamitra Mukherjee

Harish-Chandra Research Institute, Allahabad

A Thesis submitted to the
Board of Studies in Physical Science Discipline
In partial fulfilment of requirements
For the degree of

DOCTOR OF PHILOSOPHY
of
Homi Bhabha National Institute

June 2009

Certificate

This is to certify that the Ph.D. thesis titled " The Field Induced Melting of Charge Order in the Manganites" submitted by Anamitra Mukherjee is a record of bona fide research work done under my supervision. It is further certified that the thesis represents independent work by the candidate and collaboration was necessitated by the nature and scope of the problems dealt with.

Prof. Pinaki Majumdar
Thesis Advisor
Date:

Declaration

This thesis is a presentation of my original research work. Whenever contributions of others are involved, every effort is made to indicate this clearly, with due reference to the literature and acknowledgement of collaborative research and discussions. The work is original and has not been submitted earlier as a whole or in part for a degree or diploma at this or any other Institution or University. This work was done under guidance of Prof. Pinaki Majumdar, at Harish-Chandra Research Institute, Allahabad.

Anamitra Mukherjee
Ph.D. Candidate
Date:

To My Family and Teachers....

Acknowledgments

To begin, Begin

–**William Wordsworth**

Synopsis

Correlated materials such as the transition metal oxides involve strong coupling between spin, charge, orbital and lattice degrees of freedom. This leads to complex phases, with cooperative ordering in all these variables, and (often) first order boundaries between the phases. Phase transitions in these materials share some common features: (i) the small energy difference between phases makes it easy to transform one phase to another via external fields, (ii) the possibility of phase separation makes 'disorder' a crucial player in the physics, and (iii) the 'first order' transitions create a possibility of metastability and hysteresis. This thesis studies the features above in the context of the manganites where there is a close interplay of correlation effects, disorder, and thermal fluctuations.

Our focus is on the 'half-doped' manganites, materials of the form $\mathrm{A}_{0.5}\mathrm{A'}_{0.5}\mathrm{MnO}_3$, where A is a rare earth, La, Nd, Pr, etc, and A' is an alkaline earth, e.g, Ca, Sr or Ba. These materials involve strong electron-phonon (Jahn-Teller) interaction, and a large Hunds coupling on Mn between the t_{2g} core spin and the e_g valence electron. The mean radius r_A of the A and A' ions controls the bandwidth (BW), larger r_A gives a larger BW. At large BW the electron-phonon interaction is not crucial and the half-doped material is a ferromagnetic metal (FM-M). At low BW, however, the electron-phonon interaction can 'localise' electrons and create a checkerboard charge order pattern. The associated suppression of kinetic energy promotes a peculiar antiferromagnetic (AF) pattern - the CE phase - with ferromagnetic zigzag chains having AF interchain ordering. At intermediate BW, between the CE charge ordered insulator (CE-CO-I) and the FM-M, there is usually a layered AF phase.

The stability of the phases above, and their transition temperature, is also strongly dependent on the cation disorder σ_A that arises from the size mismatch of the A and A' ions. It has been experimentally demonstrated that the 'clean' phases can be weakened, or completely suppressed, by moderate cation disorder. The long range order is replaced by a nanoscale correlated glassy phase.

While the 'clean' phases are well understood, the impact of cation disorder had been explored only tentatively. In addition, the CE-CO-I can be metallised by an applied magnetic field - converting it to a FM-M. The field response of the CE phase has several intriguing features: (i) the field induced 'melting' of charge order is hysteretic, (ii) there are indications that the field melted state is inhomogeneous, with CO regions surviving in the FM background, and (iii) the melting fields reduce with reducing bandwidth in the disordered manganites, in contrast to a rapid growth in the 'clean' systems. The aim of the thesis is to construct a qualitative explanation of the observations above, using a realistic starting model, provide detailed and spatially resolved information on the melting process, and capture materials systematics to the extent possible.

We studied a model involving degenerate e_g electrons Hunds coupled to t_{2g} core spins, and to the Jahn-Teller modes of the MnO_6 octahedra. We included weak AF superexchange between the core spins, and a random 'on site' potential to mimic the cation disorder. This model was studied in two dimensions and 'half-doping' as a function of JT coupling (or inverse bandwidth), disorder, temperature (T), and applied magnetic field (h). The core spins and phonons were treated as classical.

Since the problem involves electrons strongly coupled to 'random' background fields (arising from the spins, phonons, etc), we used a recently developed variant of the exact diagonalization based Monte Carlo (ED-MC). Our method, the travelling cluster approximation (TCA) to Monte Carlo, handles thermal and spatial fluctuations accurately and being an $\mathcal{O}(N)$ method can handle system sizes $\sim 40 \times 40$ with ease. We studied a 2D system for ease of visualisation (and used due caution in comparing with experiments).

Our first study was on the distinct effects of 'A site' and 'B site' disorder on the CE-CO-I phase. While modest A site disorder, σ_A, converts the CE-CO state to a nanoscale correlated glass, suitable Mn site (B site) dopants lead to phase separation and the emergence of FM-M droplets in the CE-CO matrix. At B doping of a few % these FM-M droplets percolate leading to an insulator-metal transition. We were able to reproduce these distinct qualitative effects using simple models for A site and B site disorder. While K. Pradhan followed up with a detailed study of B dopants on various manganite phases, the problems in this thesis are on the impact of a magnetic field on the 'clean' or 'A site disordered' CE state.

In the 'clean' problem, we studied the $h - T$ phase diagram as a function of Jahn-Teller (JT) coupling (i.e inverse BW), mapping out the 'switching fields' $h_c^{\pm}$ at which CE-CO-I converts to FM-M and vice-versa. The results were consistent with experiments on the Ca based manganites, where σ_A is small. We discovered that beyond a critical JT coupling, λ_c, say, the CO does not melt on increasing field, although the CE magnetic order converts to FM. A close examination of the experimental data suggests a similar trend with decreasing r_A. Fine-tuning the electronic parameters could yield small values of $h_c^{\pm}$ compared to CO melting temperatures, as seen in some manganites. However we were more interested in the apparently inhomogeneous nature of the field melted state. Beyond the field driven CE to FM transition there seemed to be residual charge order, and spatial examination revealed that the 'metallic' state is of percolative origin! This is seen even without any external disorder. Since there are metastable states in the vicinity of a first order transition, we tried to probe the underlying finite h *equilibrium state* to separate out effects of metastability. We discovered that on increasing h the CE state converts to FM through 'progressive melting' rather than an abrupt transition - phase separating into FM and AF regions at finite h with the FM phase volume growing with increasing field. The underlying inhomogeneous equilibrium state, and the proximity of metastable FM-CO states, leads to residual CO even at large fields. This unusual character of the melted state has been verified in recent experiments.

The primary puzzle in the 'disordered' (Sr based) manganites that we sought to clarify is the collapse of T_{CO} and $h_c^{\pm}$ scales with increasing JT coupling. Naively, stronger JT coupling would have led to a more robust CO state. Our numerical results capture the correct trend, and we propose a qualitative understanding of this effect in terms of the competition between the CO stiffness (which actually reduces at large JT coupling) and the 'random fields' induced by A site disorder.

Overall, the thesis is based on a detailed exploration of the process of field induced melting of charge order in the manganites, probing for the first time the non equilibrium

aspects of this phenomenon. We have explored the parameter space of the electronic model in detail, compared our results to a large body of experimental data, and made predictions about the spatial character of the melted state. Recent measurements seem to confirm our view of this melting process.

Publications and preprints

1. Distinct Effects of Homogeneous Weak Disorder and Dilute Strong Scatterers on Phase Competition in the Manganites.
   K. Pradhan, A. Mukherjee, and P. Majumdar
   Phys. Rev. Lett. **99**, 147206 (2007).

2. Exploiting B Site Disorder for Phase Control in the Manganites.
   K. Pradhan, A. Mukherjee and P. Majumdar
   Europhys. Lett. **84**, 37007 (2008).

3. Conductance Switching and Inhomogeneous Field Melting in the Charge Ordered Manganites.
   A. Mukherjee, K. Pradhan and P. Majumdar
   Europhys. Lett. **86**, 27003 (2009).

4. A Real Space Description of Field Induced Melting in the Charge Ordered Manganites: I. The Clean Limit.
   A. Mukherjee and P. Majumdar
   arXiv:0811.3563

5. A Real Space Description of Field Induced Melting in the Charge Ordered Manganites: II. The Disordered case.
   A. Mukherjee and P. Majumdar
   arXiv:0811.3746

6. Adiabatic charge pumping through a dot at the junction of N quantum wires.
   S. Banerjee, A. Mukherjee, S. Rao, and A. Saha
   Phys. Rev. **B75**, 153407 (2007).

Contents

Chapter 1

Introduction

Chapter summary: This chapter serves as an introduction to the physics of the manganites and also to the overall thesis. We begin with a discussion of the physical ingredients that make up manganite phenomena. We then discuss a typical manganite phase diagram, highlight the issue of phase competition, and identify agencies that can drive phase transitions. We end by discussing how disorder affects manganite phenomena, and provide an outline of the problems tackled in the thesis.

1.1 Introduction to the manganites

Manganese is a transition metal with five $3d$ and two $4s$ electrons in its outer shells. The 'parent' manganites are oxides with the general formula $\mathrm{AMnO_3}$, where 'A' is a rare earth (RE) element and 'O' is oxygen. Historically, Jonker and van Santen [1] were the first to prepare the mixed valent manganite, $\mathrm{RE_{1-x}AE_xMnO_3}$, where the alkaline earth elementi AE controls the hole doping.

Consider the canonical mixed valent manganite $\mathrm{La_{1-x}Ca_xMnO_3}$. La is in a 3+ oxidation state, Ca in a 2+ state, and oxygen in the 2- state. The requirement of charge neutrality forces Mn to be in the +3 oxidation state in the undoped ($x = 0$) material. As Ca replaces La the Mn valence changes towards 4+. Here x controls the amount of Ca and hence the mean electron density on the Mn outer orbitals.

Let us describe the most celebrated property of the mixed valent manganites. When $\mathrm{La_{1-x}Ca_xMnO_3}$ at $x \sim 1/3$ is cooled from a high temperature, the resistivity initially rises with lowering temperature and then around $T \sim 250$K it falls rapidly. Moreover,

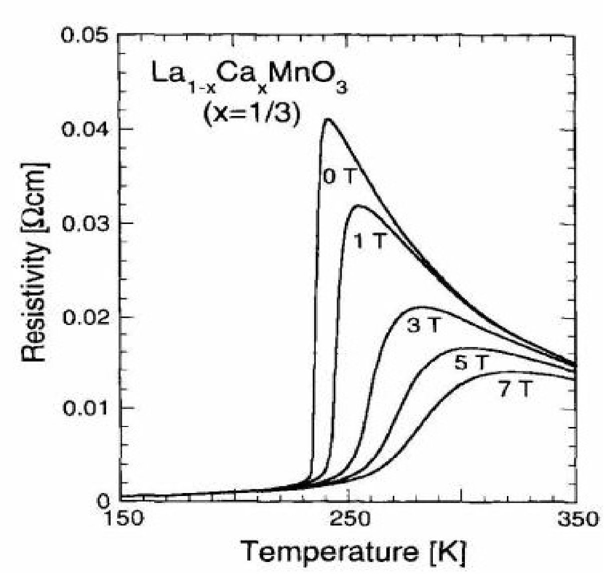

Figure 1.1: Temperature dependence of the resistivity in a $La_{1-x}Ca_xMnO_3$ single crystal at $x = 1/3$. The resistivity is shown for several fields strengths, with the magnetic field applied parallel to the electric current. (From S. Jin *et. al.*, Science **264** 413 (1994).)

the application of a moderate magnetic field, $\sim$ 7T, in this temperature regime, makes the resistivity drop sharply [2, 3, 4]. The effect is shown in Fig. 1.1. The unusually large negative magnetoresistance was dubbed 'colossal magnetoresistance' (CMR). This observation of a large change in resistivity on application of a modest magnetic field triggered an intense experimental and theoretical effort.

It was soon realized that there was more to the manganites than just CMR. In particular, these compounds provide a stage to study the cooperative ordering of strongly coupled charge, spin, lattice and orbital degrees of freedom. In the 'clean' systems the collective behaviour of these variables lead to competing ordered phases, with small energy difference between them. The first order boundary between different phases leads to windows of phase separation (PS) and, in the presence of disorder, can lead to an inhomogeneous phase coexistent state.

The structural disorder in these materials has several effects. (i) It interplays with the strong electron-phonon interaction present in these materials to enhance polaronic tendencies. (ii) Disorder on the 'B site' (the Mn site) can metallize insulators, or create a 'charge ordered' state out of a benign metal! Finally, (iii) it can lead to an equilibrium cluster coexistent state of competing phases, or arrest the kinetics associated with the

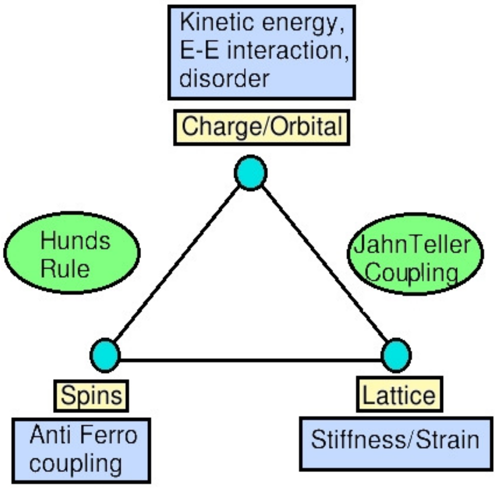

Figure 1.2: Schematic showing the various interactions in the manganites.

first order phase transition and freeze the system into long lived metastable states.

The broader theme brought to the fore by the manganites is phase competition and its manipulation by weak external perturbations. These materials serve as a laboratory for studying phase transitions in a strongly correlated system in the background of disorder.

This thesis explores such issues in the context of magnetic field induced 'melting' of charge order in the half doped manganites. The lack of analytic techniques, beyond mean field and variational approaches [5, 6, 7] to tackle this strong coupling problem forces one to employ numerical methods in such investigations. We employ one such approach, discussed later, to study the effect of thermal fluctuations, disorder and a magnetic field on ordered states in half doped manganites. Let us begin with a discussion of the building blocks in manganite physics.

1.2 Interactions and energy scales

The manganites involve spin, charge, orbital and lattice degrees of freedom. These interact via various mechanisms. The various interactions are schematically shown in Fig 1.2. Further, some of the interactions favor electron delocalisation while others aid electron localisation. The kinetic energy obviously prefers to delocalise electrons. The electron-spin interaction, arising from large Hunds coupling on Mn, favours a ferromagnetic core

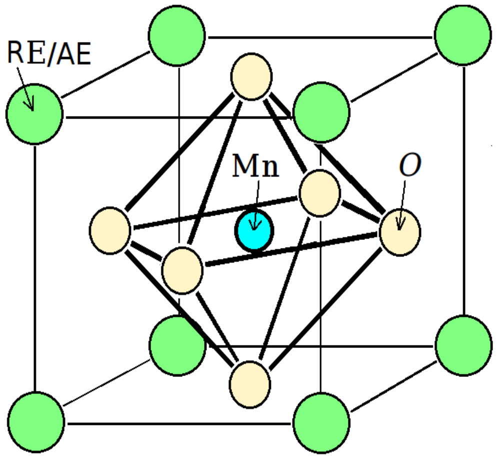

Figure 1.3: The perovskite structure. The central Mn is surrounded, by an octahedral cage of six oxygen (O) atoms. This octahedra sits in a cubic arrangement of (RE/AE) elements.

spin background since that aids electron delocalisation. Antiferromagnetic interaction among core spins tends to suppress ferromagnetic (FM) order and so disfavours electron localisation. Further, strong electron-lattice interaction aids electron localisation by forming lattice polarons. The electron-electron (Hubbard) interaction suppresses 'double occupancy' of orbitals and also aids localisation at integer filling. We will examine these interactions in some detail in the next section and also discuss their relative importance in the manganites.

1.2.1 Electronic structure

The perovskite structure is shown in Fig. 1.3. This comprises of a cubic arrangement of rare earth element, and within each cube, a MnO_6 octahedron is embedded. At the center of the octahedron sits the Mn atom. Any hopping from one Mn to another is via a bridging oxygen. The geometry of the local Mn-O-Mn bond plays a key role in hopping.

Consider the electronic levels of the Mn atom in the octahedral coordination. Fig. 1.4 on the right shows the energy levels for the $3d$ orbitals. The (free space) degeneracy of the five d levels is lifted partially due to the crystal field. The lower orbitals, dubbed t_{2g}, are d_{xy}, d_{yz} and d_{zx}, while the higher 'e_g' orbitals are $d_{x^2-y^2}$ and $d_{3z^2-r^2}$. The orbitals are shown in Fig. 1.4 on the left. The crystal field splitting between the e_g and t_{2g} levels is about 1 eV. In the Mn^{3+} based compounds, the Mn ions are in a $t_{2g}^3 e_g^1$ state. All $3d$

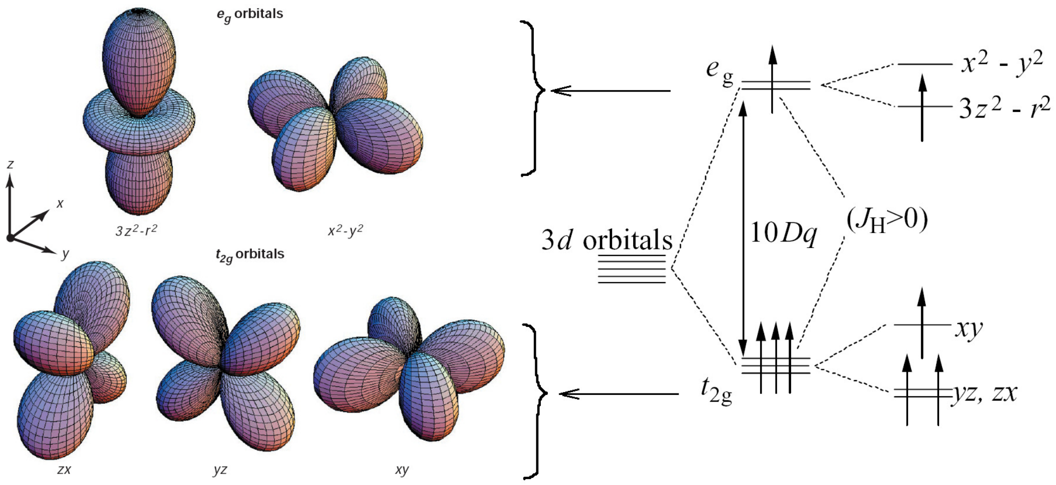

Figure 1.4: The electronic structure of the Mn ion in the octahedral environment. On the left we show the shapes of the e_g and the t_{2g} orbitals. On the right we show the actual energy level scheme. The crystal field splitting, due to the octahedral surrounding, is of magnitude of $10Dq \sim 1eV$. This splits the 3d orbital into three t_{2g} and two e_g orbitals. In the Mn^{3+} or Mn^{4+} state, the t_{2g} electrons form a $S = 3/2$ local spin while the e_g electron is itinerant. In the Mn^{3+} state, the presence of the electron in the e_g state further splits the e_g into two states, namely the $d_{x^2-y^2}$ and $d_{3z^2-r^2}$ orbitals.

electrons including the e_g ones (which strongly hybridize with the oxygen $2p$ states) are strongly affected by Coulomb repulsion and Hunds coupling. Despite the e_g band being partially filled, the parent manganite, with Mn in 3+ state, is an insulator due to electron correlation. On doping, however, the e_g electron can become itinerant and participate in conduction. The t_{2g} electrons hybridize less with the oxygen states and can be treated as localised. The presence of their oppositely aligned partners is prohibited by a large Coulomb cost, and Hunds coupling effectively produces a $S = 3/2$ local moment.

1.2.2 Hunds coupling

The ferromagnetic Hunds coupling J_H among Mn $3d$ electrons is $\sim 2 - 3$eV. This causes the spins of the t_{2g} electrons in an Mn ion to align parallel to each other. Since $J_H \gg t$, where t is the typical hopping scale of the e_g electrons, the e_g electron spins are constrained to align with the local t_{2g} spin. It is easy to see that, for example, the hopping of e_g electrons between an Mn^{3+} and an Mn^{4+} site would be suppressed if the 'core' t_{2g} spins are anti-aligned. The core spin configuration affects the effective bandwidth and the kinetic energy. This is the origin of coupling between spin and charge degrees of freedom in the manganites.

1.2.3 Spin dependent hopping

The effective hopping amplitude between two neighbouring sites i and j is proportional to the relative angle between the core spins, $\mathbf{S}_i$ and $\mathbf{S}_j$. If the spins are indexed by their polar and azimuthal angles θ_i and ϕ_i, the intersite hopping picks up the following configuration dependence [8] for $J_H/t \rightarrow \infty$:

$$t_{ij}^{eff}(\theta_i, \phi_i, \theta_j, \phi_j) = t_{ij}^0[cos(\theta_i/2)cos(\theta_j/2) + e^{\phi_i - \phi_j} sin(\theta_i/2)sin(\theta_j/2)]$$

Here t^0 is the 'bare' hopping amplitude. Neglecting Berry phase effects, one can write $t_{ij}^{eff} \longrightarrow t_{ij}^0\ cos[(\theta_{ij}/2]$, where $cos\theta_{ij}$ is the relative angle between the spins at sites i and j.

It is obvious that the hopping amplitude and hence the gain in kinetic energy is maximised if all core spins are parallel. This ferromagnetic interaction via the exchange of *conduction* electrons, whose spin have an onsite coupling with the core spin, is known as 'double exchange'. We note in passing that the Berry phase effects (related to the phase of the hopping amplitude that we neglected) is important in studying Anderson localisation [9] in these materials and also gives rise to the 'anomalous Hall' response [10].

1.2.4 Electron-phonon coupling

We again refer to Fig. 1.4. For the Mn^{3+} state, the e_g electron can choose a linear combination of the two degenerate orbitals, $d_{x^2-y^2}$ and $d_{3z^2-r^2}$. However, it turns out that in order to reduce Coulomb energy arising out of the repulsion between the e_g electron and the oxygen (in -2 oxidation state), it is favourable for the oxygen octahedra to spontaneously distort. For example, if the e_g electron occupies the $d_{x^2-y^2}$ orbital, the four planar oxygen atoms are symmetrically pushed out. Similarly, if the $d_{3z^2-r^2}$ is occupied, the state with lower Coulomb energy is that of the two apical oxygen atoms being symmetrically pushed out. Further, to minimize elastic energy (due to distortions) both kinds of distortions are volume preserving. So, while an isolated octahedron with a central Mn^{4+} is undistorted, one with Mn^{3+} is spontaneously distorted. The two distortions shown in Fig.1.5(a)-(b) are

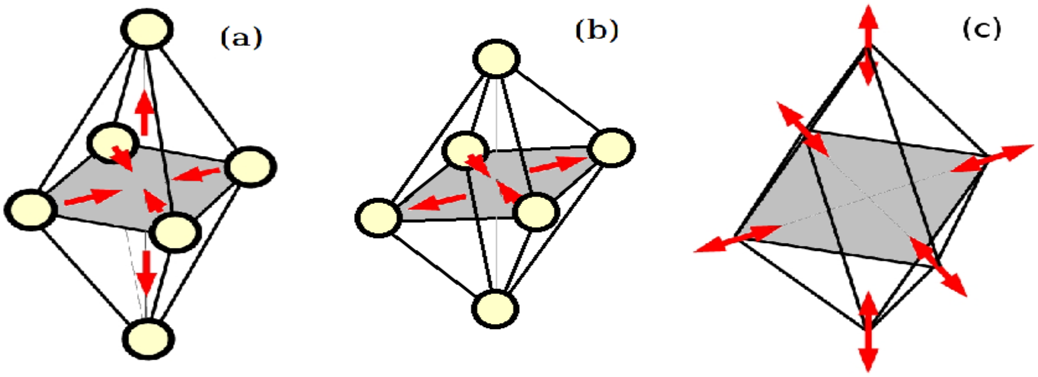

Figure 1.5: The most important phonon modes that couple with the electrons. The first two from left are volume preserving ('Jahn-Teller') distortions of the octahedra, in which either the apical or the planar oxygen atoms are pushed out. To preserve the volume the others are pulled in. The one on the right is a 'breathing mode' where all the oxygen atoms are simultaneously pushed out or pulled in.

called Jahn-Teller distortions. Among the other possible modes of octahedral distortion, only the 'breathing mode' (in which all the six oxygen atoms are pushed out or pulled in simultaneously) couple to e_g electrons. This is shown in Fig.1.5.(c).

The exact form of electron-phonon coupling will be given in Chapter.3. While the phonons modes have intrinsic quantum dynamics, the phonon fluctuations are slow on electronic timescales, and this motivates use of the 'adiabatic' limit where phonons are treated as (annealed) classical distortions. Needless to say this simplifies calculations significantly. In the present thesis we assume this adiabatic limit. We also note that octahedra are connected to each other via corner shared oxygen, so the distortion of one octahedron creates a strain field that affects other octahedra. The lattice distortions are 'cooperative' in nature.

1.2.5 Superexchange interaction

Another interaction, of importance in some doping regimes, is antiferromagnetic superexchange (SE) between t_{2g} core spins on nearest neighbour sites. The phenomenological evidence for the presence of SE interaction is the 'G type', $\mathbf{q} = \{\pi, \pi, \pi\}$, antiferromagnetic order in CaMnO$_3$ [11]. The Mn ions in CaMnO$_3$ are in a 4+ state so there are no e_g electrons, and the magnetic order has to arise from SE couplings. Hatree-Fock calculations [12], estimates of superexchange coupling in $LaMnO_3$ [13] and local spin density approximation (LSDA) calculations [14] all lend support to the presence of weak AF superexchange coupling in the manganites.

1.2.6 Electron-electron interaction

The e_g electrons also interact via Coulomb repulsion. The repulsive 'Hubbard' cost U is a measure of the energy difference between states with different electronic configurations. For two Mn^{3+} ions, U would be difference in energy between the following two states: (i) each Mn site having one e_g electron and three t_{2g} electrons ($2d^4$), and (ii) one site having both e_g electrons and the other none ($d^5 d^3$).

Photoemission data [15] suggest $U \sim 10eV$, but the effective U between the e_g electron has been suggested to be smaller but $\sim 3eV$. This can happen if low energy processes involving transfer of electrons from Mn to some appropriately hybridized oxygen ligand orbital takes place rather than from Mn to Mn. Insulators stabilized by such a mechanism are classified as charge transfer insulators [16], where the effective repulsion scale is rather small compared to that for a Mott insulator with the same U.

It has been suggested that $LaMnO_3$ is a charge transfer insulator (**reference ..**). There is some evidence that the effective repulsion in the manganites is weaker than the 'bare' value quoted above. Even after this reduction, the U scale that emerges is about 3eV (for $LaMnO_3$) to 5eV (for $CaMnO_3$). While still the largest scale in the problem, some of its effects (notably supression of 'double occupancy') can be mimicked by JT distortion. We discuss this in detail in Chapter.3. However, the Hubbard interaction does play an important role in describing the ferromagnetic metallic state[17, 18, 19, 20, 21], where the Jahn-Teller distortion is not appreciable. In our calculations, U is not considered. While Coulomb interactions certainly have a quantitative impact, retaining the large Hunds coupling and strong Jahn-Teller interaction captures much of the qualitative physics in these materials.

1.2.7 Adiabaticity

At low enough temperature quantum fluctuations of the lattice become important and the quantum dynamics of the phonons need to be considered. However, primarily for keeping the problem tractable, these quantum fluctuations are disregarded in our calculation. It is necessary to check the quality of this approximation. The phonon adiabaticity parameter γ is defined as the ratio of the Jahn-Teller phonon frequency to the hopping scale. This ratio is about 0.1-0.2 [22, 23, 24]. Experimental work probing charge localisation by static and dynamic lattice distortions [25] and through electric and thermal transport measurements [26] indicate the importance of both the static and dynamic distortions, though the static effect remains dominant at room temperature.

The adiabatic approximation has been discussed in earlier theoretical work [27], where it was concluded that for $T \gtrsim T_{ord}$, where T_{ord} is the typical magnetic ordering temperature $\sim$ 200K, the use of classical phonons is acceptable. For example, the estimates of T_C using quantum and classical phonons lead to very similar results [27]. In this spirit we consider only static phonons. At low temperature and in an ideally clean system the phonon dynamics will affect the electronic spectrum and transport. In the presence of disorder, however, these effects are apt to be smeared out.

1.2.8 Energy scales

Let us conclude this section by discussing the hierarchy of energy scales in the manganites.

The largest scale is the effective onsite Coulomb repulsion, estimated to be about 5.2 ± 0.3eV and 3.5 ± 0.3eV, for $CaMnO_3$ and $LaMnO_3$ respectively[28]. Next in the hierarchy is the Hunds coupling $\sim$ 2eV, much larger than the hopping scale[29]. Then comes the crystal-field splitting between the e_g and t_{2g} levels, estimated [11] to be about 1 eV. The hopping t was earlier estimated to be between 0.2eV and 0.5eV [30, 31, 32], however more recent experiments estimate this value to be about 0.2eV [11]. The static Jahn-Teller energy, corresponding to polaron binding, is $\sim$ 0.25eV. Further the ratio of the breathing mode frequency to that of the Jahn-Teller mode is about 2 [33]. As long as this ratio is larger than 1, the qualitative results are not affected on ignoring the breathing mode.

We will consider only the JT mode. The superexchange scale J is the smallest

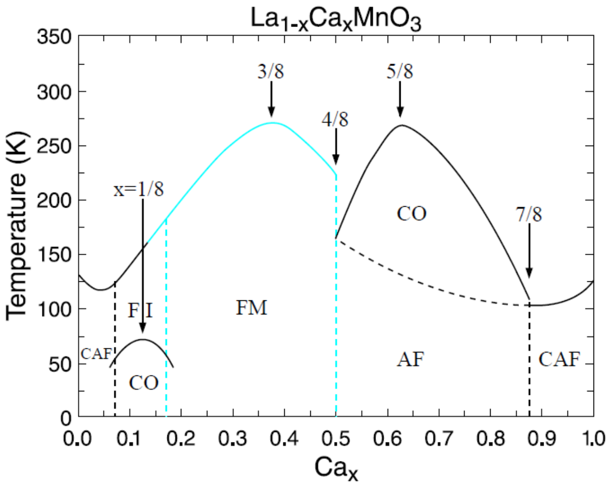

Figure 1.6: Phase diagram of $La_{1-x}Ca_xMnO_3$. FM: ferromagnetic metal, FI: ferromagnetic insulator, AF: antiferromagnetism, CAF: canted antiferromagnet, CO: charge/orbital order. (From S-W Cheong *et. al.*, in *Colossal Magnetoresistive Oxides, edited by Y. Tokura, Gordon and Breach, Amsterdam* (2000).)

among the set of couplings considered here. For $CaMnO_3$, which is a G-type insulator at low temperatures, fitting to 3D Heisenberg model yields JS^2 to be about $0.05t$ in hopping units, for $S = 3/2$.

With this background let us look at typical phase diagrams to identify various phases, highlight phase competition, and locate variables that can allow us to tune the balance between phases.

1.3 Complex ordered phases

1.3.1 Phase competition

The complexity of the manganite phase diagrams is visible in Fig 1.6. Here we show the $x - T$ phase diagram for $La_{1-x}Ca_xMnO_3$. This shows the various phases that arises as one changes the carrier concentration in the (La,Ca) combination, while Fig 1.8 shows $x - T$ phase diagrams for materials with different cation combinations (and so different bandwidth). There the three manganites shown, $La_{1-x}Sr_xMnO_3$, $Nd_{1-x}Sr_xMnO_3$ and $Pr_{1-x}Ca_xMnO_3$, with successively smaller mean cation radius, *i.e.*, average radii of the AE and the RE ions, from (a) to (c). This implies a decrease in bandwidth (BW) as we move from (a)-(c). Clearly at any given carrier concentration, BW variation leads to new phases. Given the richness and complexity of the $x - T$ phase diagrams and their evolution with changing BW, let us explore them systematically. We first look at (i) the evolution of the phases with changing doping and later (ii) compare $x-T$ phase diagrams in different BW materials. Let us start with the obvious question:

Why do change in carrier concentration and BW lead to phase competition ?

(i) Carrier Doping : The carrier density (hole doping x) plays a crucial role in this process since the double exchange interaction depends on carrier density. While the strength of double exchange should increase as the ratio of Mn^{4+} to Mn^{3+} increases, peaking at $x = 0.5$, the charge and orbital ordering tendencies are strong at commensurate doping, leading to a dip in the FM T_c near $x = 0.5$.

(ii) Varying BW : As we discuss in detail in Chapter.2, the bandwidth reduces with reduction in the mean cation radius. A reduction in the BW enhances the tendency to localise the e_g electrons via electron-phonon interaction. Moreover, the suppression of kinetic energy weakens the ferromagnetic exchange, allowing the appearance of antiferromagnetic order.

Let us now discuss the $x - T$ phase diagram of a $La_{1-x}Ca_xMnO_3$ [37], Fig 1.6, in some detail . It has the largest BW among the Ca based manganites and has been studied intensively in the field melting problem. Here we explore the phases that arise as one changes the carrier concentration.

Doping dependence: $La_{1-x}Ca_xMnO_3$

Starting from the undoped material, which is an insulator with A-type magnetic order, we see from Fig 1.6, that a number of complex phases arise at low temperature. For $x < 0.17$, the system remains insulating, with a variety of magnetic states, these we discuss below. Between $x = 0.17$ and $x < 0.5$, the system is a ferromagnetic metal. At $x = 0.5$ the system becomes an insulator with long range charge, orbital and spin order. Beyond $x = 0.5$, while the system remains insulating all through to $x = 1$, the magnetic state evolves from CE type at $x = 0.50$ to G type at $x = 1.0$. The doped carriers in this regime, $x = 0.5 - 1.0$, form charge stripes, discussed below. We also note that at commensurate filling, $p/8$, $p = 1, 2, 3, 4, 5$, and 7, there are certain features that we will

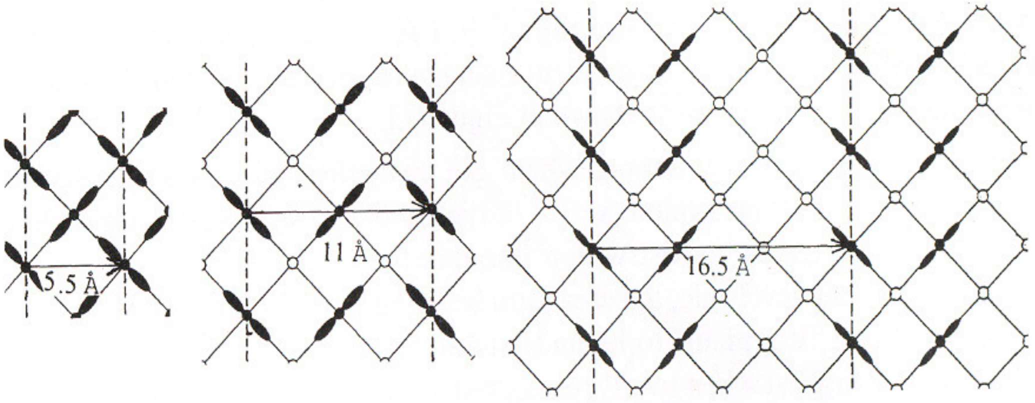

Figure 1.7: The charge and orbital ordering configurations in the orthorhombic basal plane for x=0, 1/2 and 2/3 for $La_{1-x}Ca_xMnO_3$). Open circles show Mn^4+. Lobes show orbital ordering of e_g electrons of Mn^3+. The charge modulation waves lengths are 5.5, 11 and 16.5 Å for x=0, 1/2 and 2/3 respectively.

touch on below.

Undoped compound: The insulating compound $LaMnO_3$ ($x = 0$) is strongly affected both by cooperative Jahn-Teller distortion and electron correlation, as the e_g band is fully filled. The collective Jahn-Teller distortion leads to orbital ordering, with alternating $d_{3x^2-r^2}$ and $d_{3y^2-r^2}$ orbitals on the $a-b$ plane. Here, the x and y axes are taken along the orthogonal Mn-O bond directions on the $a-b$ plane. The orbital order sets in at $T_{OO} \sim$ 780K. In this Jahn-Teller distorted and orbital-ordered state $LaMnO_3$ undergoes an antiferromagnetic transition at T_N = 120K. The spin ordering is layered ($A-type$), ferromagnetic in the $a-b$ plane with antiferromagnetic order along the c-axis. The schematic of the charge and orbital pattern in the $a-b$ plane, is shown in Fig 1.7.(a).

Light to intermediate doping $x < 0.5$: Hole-doping by substitution of La with Ca (Fig. 1.6) causes the ordered spins to cant. This happens because canting allows for hopping, taking advantage of the empty sites. With increase in the doping level above $x \sim 0.07$, the system is ferromagnetic, due to local excursion of the e_g electrons. The compound, however, remains in an orbital ordered insulating state up to, $x \sim 0.17$, the critical doping for the insulator-metal transition. This low doped insulating state appears to be a mixture of hole rich FM regions and hole poor antiferromagnetic regions.

For x between 0.07 and 0.17, the doped holes order leading to an AF-CO state, which is most stable at $x = 1/8$. Such hole ordering is also seen in low doped $La_{1-x}Sr_xMnO_3$ [38]. This AF-CO state gives way to a ferromagnetic insulator on increasing temperature. The insulator to metal transition at $x \sim 0.17$ is also accompanied with a decrease in the static Jahn-Teller distortions. The state beyond $x = 0.17$ is a ferromagnetic metal (FM-M). The T_c increases with x up to $x = 3/8$ and then drops. This drop in T_c is indicative of the presence of competing magnetic phases for $x \rightarrow 0.5$. As mentioned before, contrary to the expectation of the T_c being highest at $x = 0.5$, from purely double exchange considerations, the strong tendency of charge-orbital order stemming form the electron lattice coupling, suppresses the T_c as x increases beyond 3/8.

Around half doping: At half doping, there is a change from the FM-M to a peculiar spin, charge and orbital ordered state. The spin order is that of zigzag ferromagnetic chains coupled antiferromagnetically in the $a - b$ plane (CE pattern). This pattern is repeated in the c direction such that the zig-zag ferromagnetic chains couple antiferromagnetically in the c direction. The charge occupation forms a checkerboard pattern in the $a - b$ plane and this pattern is stacked in the c direction. The orbital occupancy of the occupied sites has alternating $d_{3x^2-r^2}/d_{3x^2-r^2}$ order (OO) in the a-b plane. The in plane (a-b), schematic of the charge and orbital pattern in shown in Fig 1.7.(b). Beyond $x > 0.5$ the doped carriers localise and order with stripe modulations at low T, along with antiferromagnetic occurring. The stripelike CO exists over a large window of doping, for $x \geq 0.5$, and is most robust at $x = 5/8$. Detailed measurements [39] have revealed that that the CO at $x = 5/8$ is a mixture of the CO at $x = 1/2$ (Fig 1.7.(b)) and $x = 2/3$ (Fig 1.7.(c)), though it is not clear why the CO is most robust in this case. The AF-CO beyond $x = 5/8$, begins to weaken and forms a canted antiferromagnetic (C-AF) insulating phase.

Overdoped regime ($7/8 \leq x \leq 1$*):* The state at $x = 1$ is a G-type insulator [62]. From this end to $x = 7/8$, the CAF insulating phase can be understood as weak FM state, driven by local excursion of electrons, as opposed to the CAF-I driven by delocalisation of holes for $x \sim 0.1$.

Having seen how changing doping can lead to phase transitions, Fig. 1.8.(b) and Fig. 1.9 show several phases and their schematic spin and orbital order. One can also stay at fixed doping and explore the effects of changing BW, say, by comparing the

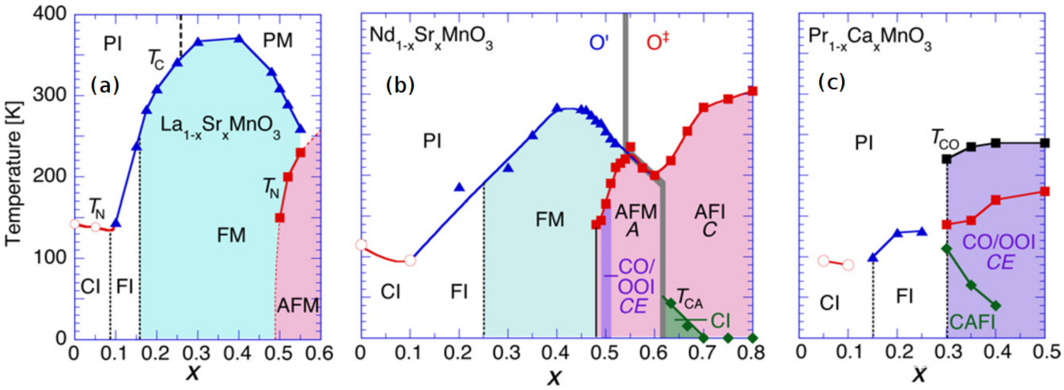

Figure 1.8: The magnetic as well as electronic phase diagrams of (a) $La_{1-x}Sr_xMnO_3$, (b) $Nd_{1-x}Sr_xMnO_3$ and (c) $Pr_{1-x}Ca_xMnO_3$. PI, PM and CI stand for the paramagnetic insulating, paramagnetic metallic and spin-canted insulating states, respectively. FI, FM and AFM denote the ferromagnetic insulating, ferromagnetic metallic and antiferromagnetic (A-type) metallic states, respectively. At $x = 0.5$ $Nd_{1-x}Sr_xMnO_3$, the charge-orbital ordered insulating (CO-OO-I) phase has CE-type spin order. For $0.3 \leq x \leq 0.5$ in $Pr_{1-x}Ca_xMnO_3$, the antiferromagnetic insulating (AFI) state exists in the CO-OO-I phase. The canted antiferromagnetic insulating (CAFI) state also shows up below the AFI state in the CO-OO-I phase for $0.3 \leq x \leq 0.4$. (From Tokura *et. al.*, J. Magn. Magn. Mater. **200**, **1**, (1999).)

$x = 0.5$ state in the three phase diagrams shown in Fig. 1.8. Let us now discuss such BW dependent features.

Bandwidth dependence

As we go from (a) to (c) in Fig. 1.8 we notice that reducing BW changes the windows for the various phases, and sometimes brings in new phases. As one would expect, the metallic window observed at intermediate doping in $La_{1-x}Sr_xMnO_3$, shrinks in $Nd_{1-x}Sr_xMnO_3$ and is absent in $Pr_{1-x}Ca_xMnO_3$.

The other important feature is the change in the commensurate doping $x = 0.5$ state. At half doping there is a delicate balance between the kinetic energy and localisation tendencies. Small BW can lead to a π, π planar charge ordered phase with CE type magnetic order and orbital stripes. This $a - b$ planar pattern is stacked in the c-direction. For notational simplicity we shall refer to this phase as the CE-CO-I phase. We will discuss this phase in detail in the next chapter and it will be central to this thesis.

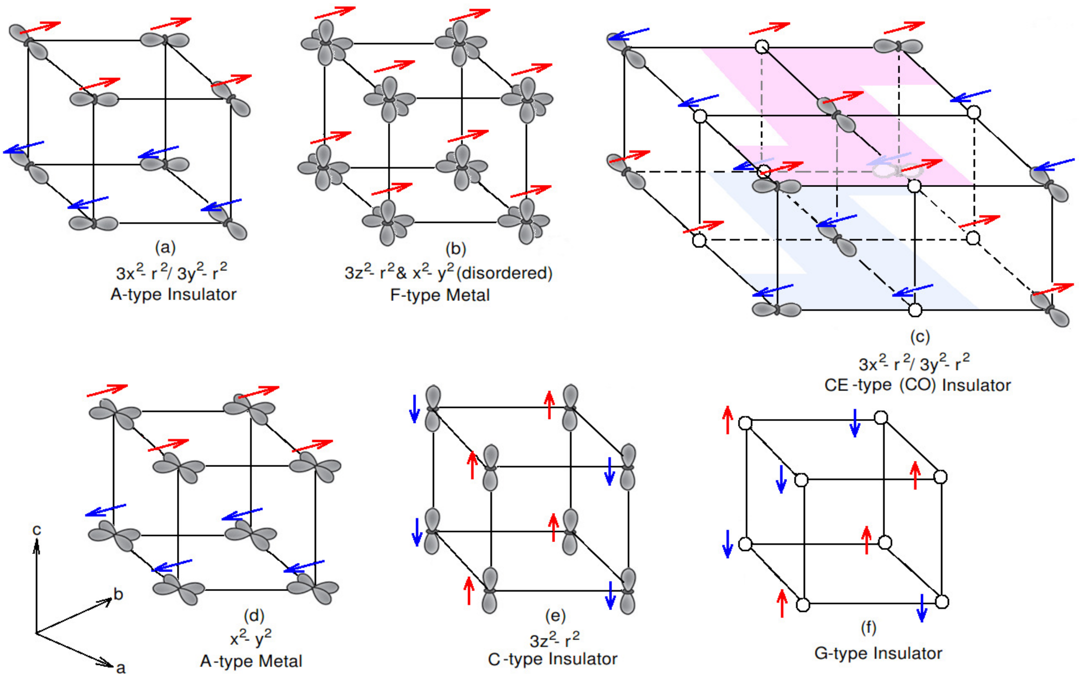

Figure 1.9: Schematic of orbital and spin order for various phases that occur with changing doping in $Nd_{1-x}Sr_xMnO_3$. (a)-(f) are representative of the low temperature phases that appear in Fig. 1.8.(b). The lobes show the e_g orbital occupancy and arrows depict the spin direction. (a) Orbital ordered A-type insulator occurring for $x \leq 0.1$. (b) Orbital disordered, FM-M for $0.25 < x < 0.5$, (c) CE phase in a narrow window around $x = 0.50$, in plane (a-b) checkerboard charge order and orbital order. The zig-zag nature of the ferromagnetic chains is shown in color bands in the two planes. The spins in successive planes are antiferromagnetically locked, whereas the orbital and the charge patterns are stacked in the c-direction. (d)-(e) A type orbital ordered metal between $x = 0.50$ and 0.60, and C-type orbital ordered insulator for x between $0.60 - 0.80$. (f) The G-type insulator at $x = 1$.

Let us just look at the broad trend in the stability of this phase. In the largest BW material $La_{1-x}Sr_xMnO_3$, we find that this state is not stabilized at all. It makes an appearance with decreasing BW in $Nd_{1-x}Sr_xMnO_3$ at $x = 0.5$ and has a broad window of stability for $Pr_{1-x}Ca_xMnO_3$, which has the smallest BW among the three. Also the T_{CO} grows with reducing BW from $Nd_{1-x}Sr_xMnO_3$ to $Pr_{1-x}Ca_xMnO_3$.

Thus even when we just focus at half doping, there is a systematic increase in the stability of the CE-CO-I phase with decreasing BW. However, the situation is actually more complicated. As we will see in Chapter.2, detailed material trends indicate a more complex relation between the reduction of BW and the stability of the CO state. As will

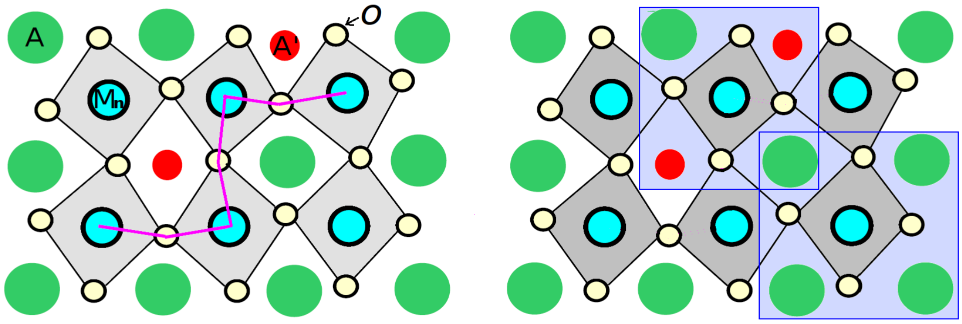

(a) (b)

Figure 1.10: Schematic showing ways in which A-site doping aids in generating disorder. (a) shows a system where few A sites have been substituted with A' of different radii. The size mismatch causes the oxygen octahedra to tilt and this suppresses the hopping between the octahedra around the A site that has been substituted. (b) Consider the local charge environment of the Mn sites in the two squares. In comparison to the lower one in which the central Mn site has only A ions around it, the one on the top, has two A and two A' around it. If the valence state of the A' is different from that of A, which is typically the case, the Mn site will see a Coulomb potential that is different from other Mn sites, such as the one in the lower square. This creates random scattering centers on the Mn lattice.

turn out, the role of quenched disorder is vital in understanding the stability of the CO state. With this in mind let us briefly touch upon the role of disorder.

1.3.2 Role of disorder

Consider the generic parent compound $AMnO_3$. In this all Mn-O-Mn bond angles are 180^o, even in the presence of cooperative Jahn-Teller distortions. For hole doping A ions are replaced by A' ions and the size mismatch of the ions makes the oxygen octahedra adjust to the new situation. This causes the octahedra to tilt as shown in Fig. 1.10.(a). As we discuss later, this suppresses the hopping amplitude roughly as $\sim cos^2\theta$, where θ is the Mn-O-Mn bond angle. This reduces the overall BW and also creates random fluctuation in the hopping amplitudes. Further, the different local environment of different Mn ions, shown in the schematic in Fig. 1.10.(b), leads to a random potential on the Mn ions due to the Coulomb interaction with the neighbouring A, A' ions. The hopping modulation and scattering potential are the two primary sources of A-site disorder. We will discuss these and their implication on the half doped state in more detail in Chapter.2.

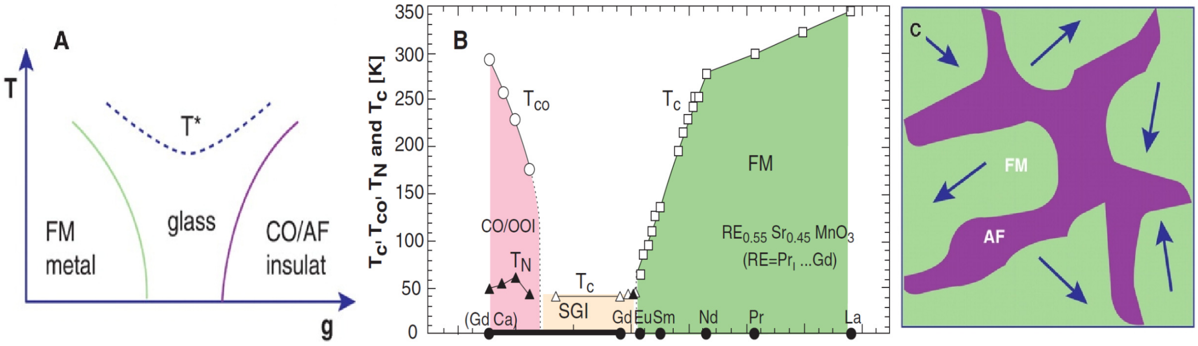

Figure 1.11: (a) Generic phase diagram of two competing states, a FM-M and an AF-CO-I in the presence of quenched disorder. g is a generic variable to move from one phase to the other (e.g., electronic density or bandwidth). A glassy mixed-phase state is created and a glass transition temperature scale (T$_G$) appears. (b) Experimental phase diagram of manganites with moderate disorder [41, 49]. Note the disorder-induced suppression of the ordering temperatures and the appearance of a glass state, as predicted by schematic shown in (a). (c) Typical sketch of the CMR state for the manganites containing FM clusters with randomly oriented moments separated by regions where a competing AF-CO-I phase is stabilized [42, 43, 44]. (From E. Dagotto, Science, **309**, 257 (2005).)

Another kind of disorder is that obtained by randomly substituting on the Mn site (the ‘B site’). Weak disorder of this kind creates many interesting and novel effects. Although we have worked on this, it is discussed in detail in the thesis of K. Pradhan from HRI. In the present thesis we will consider only the effects of A-site disorder.

1.4 Phase separation

In the previous section we looked at phase transitions that can arise from changing BW, doping and temperature. Here we look at the occurrence of phase coexistence (PC) that arises from phase separation (PS) tendency in these materials. This happens when phases compete across a first order boundary especially in the presence of disorder. In the process, we will also discuss the impact of disorder on ordered states in manganites and on their response to applied magnetic fields and temperature.

Phase coexistence and CMR: Careful experimental [40, 41, 42] and theoretical [43, 44, 45, 46, 47] work has lead to the consensus that phase coexistence plays a role in CMR behavior. While phase *separation* (PS) can occur without disorder, and would be

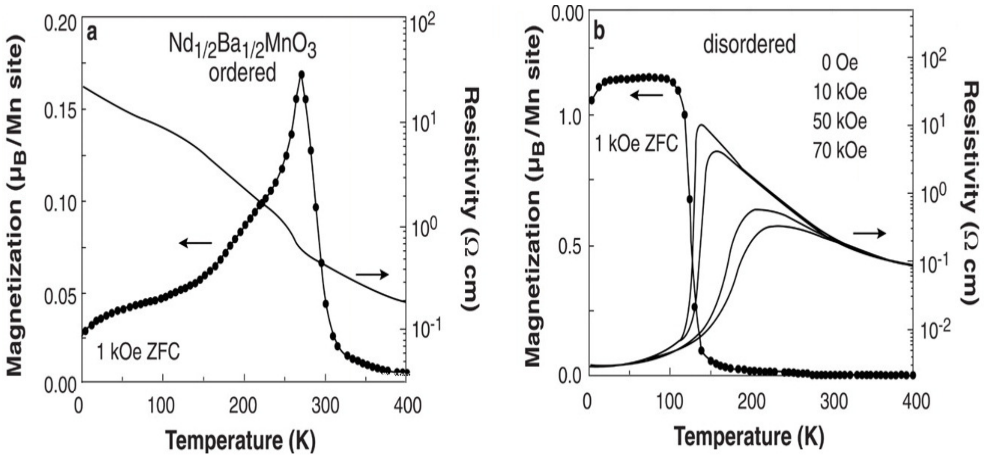

Figure 1.12: Resistivity and magnetization versus temperature for the ordered (a) and disordered (b) structures of $Nd_{0.5}Ba_{0.5}MnO_3$. Only the disordered crystal shows the CMR effect. (From D. Akahoshi, et al., Phys. Rev. Lett. **90**, 177203 (2003).)

regulated by long range Coulomb forces, etc, in the manganites the actual phase *coexistent* (PC) state is crucially affected by disorder [48].

Fig 1.11.(a), shows a schematic of the view that has gradually emerged from theoretical work[43]. In the presence of disorder (such as A-type disorder), neither of the FM-M or the AF-CO-I appear to occur globally over a window of coupling, g, say. This in clearly contrary to what would have happened in the clean system, where phases are separated by first order boundaries at low temperature. There, beyond a critical value of g causing the first order transition, the system would go from being a FM-M to a AF-CO-I or vice versa, when g is varied slowly enough. However, in the presence of disorder, the system breaks up into a mixture of the two phases, with short range order of both phases existing together. Experimental results on such systems as shown in Fig 1.11.(b), bears out this possibility. Further, transport measurements has shown that such PS state shows glassy behaviour. A schematic of a 'cluster glass' is shown in Fig 1.11.(c). The randomly oriented ferromagnetic domains are hole rich. In response to small applied magnetic field they point in the same direction. If they can percolate, a 'colossal' response in transport can occur.

In $Nd_{0.5}Ba_{0.5}MnO_3$, the CMR is seen only in the disordered case while in the ordered material, Fig 1.12(a,b), it is not seen (we will discuss what 'ordered' materials are in the next chapter). This clearly brings out the importance of disorder to CMR effect.

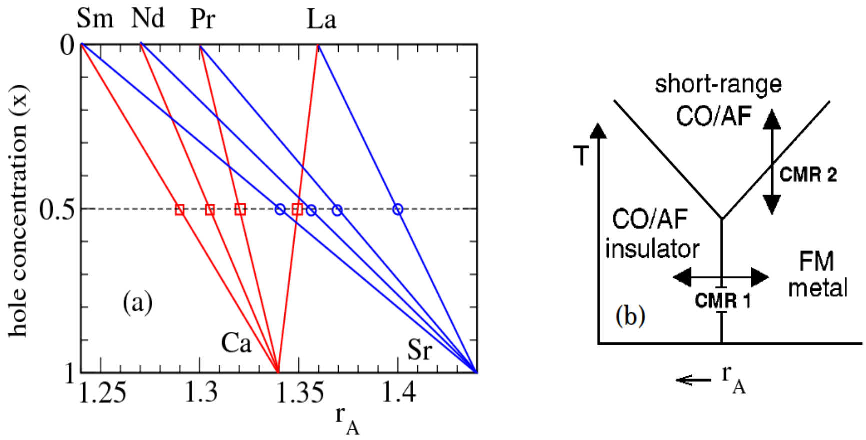

Figure 1.13: (a) Variations of the hole concentration x vs the effective one electron BW on the x axis with substitution at the perovskite A- site. The A-site cations with various RE^3+ and AE^2+ are plotted on the upper and lower x-axis, respectively. Substitution of La with Sr corresponds to a line connecting between La and Sr. The radii of the two families, the Ca-family and the Sr-family are shown in red and blue colors respectively. (From Tomioka *et. al.*, *Colossal Magnetoresistive Oxides, edited by Y. Tokura, Gordon and Breach, Amsterdam* (2000).) (b) A representative r_A vs T phase diagram showing a tricritical point, with various bicritical phase boundaries: 'CO/AF-I' - 'FM-M at low temperature, 'short range CO/AF' - 'CO/AF-I (long range)' at high temperature and low r_A, and 'short range CO/AF' - 'FM-M' at high temperature and large r_A (or large BW). Magnetic field induced melting of low temperature CO/AF-I into an FM-M leads to CMR without the need of disorder (CMR-1), while for that around T_c (CMR-2), disorder is crucial. (From E. Dagotto, Science, **309**, 257 (2005).)

While, the above scenario is now accepted as a basic description of CMR related effects, a lot remains to be clarified. There has been very little analysis of the dynamics associated with phase coexistent states. Given the first order nature of transitions, there is a possibility of systems remaining trapped in metastable states if enough relaxation time is not allowed for. Even if the transition is carried out quasi-statically, the presence of disorder can pin phases locally leading to coexistence. In real systems disorder is always present, and intrinsic relaxation times are also large [51, 52], so both the effects are relevant. This thesis is primarily concerned with such effects, especially in half doped manganites.

Disorder effects and CMR at half doping : These issues can be conveniently addressed at half doping where, as we will see, one can get a CMR (around T_c) by tuning the BW or r_A. Decreasing r_A reduces the BW and accordingly a large r_A material like

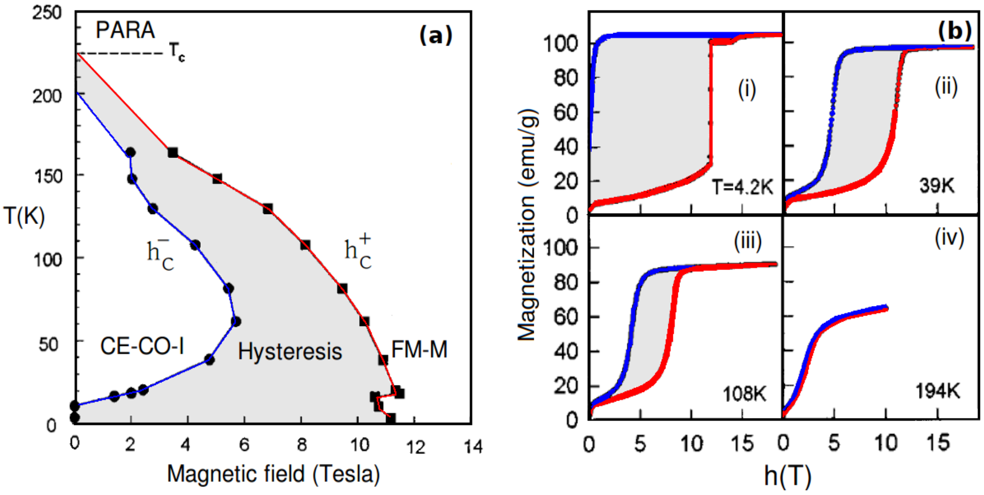

Figure 1.14: (a) Phase diagram of La$_{0.5}$Ca$_0$.5MnO$_3$ in the magnetic field (h)-T plane. h_c^+ (red line) and h_c^- (blue line) are critical fields for the 'CE-CO-I' - 'FM-M' and 'FM-M' - 'CE-CO-I' transitions respectively. The shaded region shows hysteresis. This window widens at low T, shrinks at intermediate T and tapers off and vanishes at T_{CO} (b) Magnetization vs field at various temperatures. Note that at low T, the CE-CO-I state is not recovered even when the field if swept back to zero. (From G. Xiao et. al. Phys. Rev. **B 54**, 6073 (1996).)

La$_{0.5}$Sr$_{0.5}$MnO$_3$ (LSMO) has a FM-M ground state at half doping while smaller BW material like Nd$_{0.5}$Sr$_{0.5}$MnO$_3$ (NSMO) has a CE-CO-I ground state.

The radii of the materials for various compositions of RE and AE elements is shown in Fig 1.13.(a). We focus on the radii at half doping only, which gives a systematic material composition for changing r_A. Changing r_A in this manner one can approach the phase boundary between FM-M and CE-CO-I schematically shown in Fig. 1.13.(b). On the CE-CO-I side being close to the bicritical boundary implies that the free energies of the CE-CO-I and FM-M states are close by. Thus if a small magnetic field is applied the Zeeman energy is sufficient to overcome the free energy barrier and the CE-CO-I state can melt to an FM-M. This magnetic field induced low temperature insulator to metal transition is another example of MR, where the response can be colossal (denoted as CMR-2) in Fig. 1.13.(b). One can go very close to the bicritical boundary thereby reducing the applied field necessary to very small values. Note that in contrast to disorder being crucial to CMR that happens around T_c (denoted as CMR-1) in Fig. 1.13.(b), here the CMR can be achieved even in clean samples.

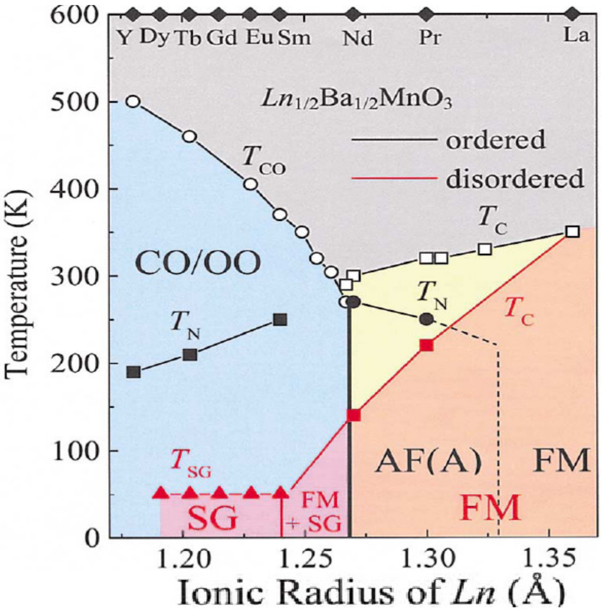

Figure 1.15: Electronic phase diagrams for the A-site ordered (black line and symbols) and disordered (red line and symbols; the region shaded in red) perovskites with half doping $Ln_{0.5}Ba_{0.5}MnO_3$, as a function of the ionic radius of Ln. CO/OO, FM, and SG stand for the charge/orbital ordered, ferromagnetic, and spin-glass states, respectively. T_{CO}, T_C and T_{SG} represent the respective transition temperatures. The data for the mixed crystal compounds with Ln=(Nd, Sm) and (La, Nd), both Ln=Ba ordered and disordered, are also shown. (D. Akahoshi, *et al.*, Phys. Rev. Lett. **90**, 177203 (2003).)

Of course, this is not the full story, and, as we will soon see, the BW is not the only parameter deciding the response of these half doped materials. However, before introducing further complications let us see what happens when we apply a magnetic field to the CE-CO-I state at low T and perform a field cycle $[0 \rightarrow h_{max} \rightarrow 0]$. Fig. 1.14.(a) shows the magnetic field (h) vs temperature phase diagram for $La_{0.5}Ca_{0.5}MnO_3$ [53] obtained from such fixed T field sweeps. Typical sweeps depicting magnetization as a function of h are shown in Fig. 1.14.(b). The red line in Fig. 1.14.(a) denotes the critical field needed to melt the CE-CO-I state in the forward part of the sweep (h_c^+). Similarly, the blue line denotes the field at which the CE-CO-I state is recovered in the backward sweep. The area between the two lines is the window of hysteresis. Fig. 1.14.(b) shows magnetization as a function of field sweep at various temperatures. At low T the system finds it diffcult to get out of metastable states, resulting in the wide hysteresis window, but at higher T the window shrinks, vanishing at T_{CO}. While the hysteresis itself is expect around a first order phase transition, there are several puzzling features.

At low T, from Fig. 1.14.(a) and Fig. 1.14.(b)-(i), we see that the CE-CO-I state is not recovered when the field is swept back to zero. Similar experiments on progressively smaller BW materials ($\mathrm{Ln_{0.5}Ca_{0.5}MnO_3}$), using different Ln atoms, shown in Fig. 1.13, indicate that (a) the systems with smaller BW can recover the CE-CO-I state and (b) there is a gradual increase in the melting fields with reducing BW. Finally there are materials where the CO does not melt at all. These systematics can be attributed to the growing difference between the 'FM-M' - 'CE-CO-I' free energies as one moves away from the phase boundary deeper in the CE-CO-I phase with decreasing BW. While this seems reasonable, similar experiments on the $\mathrm{Ln_{0.5}Sr_{0.5}MnO_3}$ family shows a dramatic suppression of the melting fields with reducing BW, in clear contrast to the rationale given for the Ca family. Since the BW of these two families do not differ by a great amount (there are material of both families with very similar r_A, Fig. 1.13), this clearly shows that BW by itself can not explain the observed systematics in the response of the charge ordered state to an applied field.

The systematics of the non equilibrium response (non recovery vs recovery of the CO in field sweep experiments), the striking difference in response of similar BW materials, and the spatial nature of the melted state, will be explored in the thesis. One needs to take disorder into account for consistently understanding these issues.

With this view let us look at the effects of disorder on the CE-CO-I state. Fig. 1.15, shows the superposed $r_A - T$ phase diagrams of 'ordered' and 'disordered' perovskite manganites at half doping, belonging to the family $\mathrm{Ln_{0.5}Ba_{0.5}MnO_3}$. In the 'ordered case' (black lines), as discussed above, the CE-CO-I state competes with the FM-M state. The phase boundary is tricritical, with the FM-M, CE-CO-I and AF-M competing with each other at $r_A \sim 1.27$. This AF-M phase, a metal with line like A type magntic phase, sits between the FM-M and CE-CO-I phases and puts a lower bound to the smallest magnetic field that can melt the CE-CO-I phase at low temperature. This issue discussed in Chapter.4. Further, with increasing BW, the double exchange driven FM phase is progressively stabilized, as seen in the increase of T_c with increasing BW. Also, enhancement of the localisation tendencies (due to reducing BW or r_A), causes the charge ordered state to be more stable, leading to increasing of T_{CO}. Note on the other hand the T_{CE} decreases with decreasing r_A. This has origin in the fact that with decreasing BW as electrons get more strongly site localised, the kinetic energy gain from local hopping of the electrons get suppressed. and the delicate balance between the kinetic energy anf the AF superexchange that stabilized the CE phase is destroyed weakening the CE phase.

If we look at the phase diagram of the 'disordered' material (red lines) the CE-CO-I state is completely destroyed. The CE-CO correlations are broken down to nanoscale leading to loss long range order. This state has been explored in recent experiments [54], in particular, $Eu_{0.5}Ba_{0.5}MnO_3$. It has been established that the disorder transforms the CE-CO-I state to a spin glass with short range charge and orbital correlations. It also shows memory, aging and rejuvenation typical to glasses. On the FM-M side the T_c is suppressed but the system still remains a disordered FM-M. In attempt to understand the full systematics of field melting of the CE-CO-I state in presence of disorder we first reproduced these results, which actually is at large disorder. As mentioned, of the three families, the Ba family has the largest disorder, then comes the Sr-family while the Ca family has the least disorder. To study the effect of disorder on field melting in the Ca and Sr families, we also studied systems at weaker disorder. Weak disorder ensures that the CE-CO-I state is not completely destroyed, but is weakened nonetheless. Then on field sweeping, disorder effects such as pinning and arrested kinetics of the first order transition, comes to fore, and will be shown to dictate most of the observed material systematics in Chapter.5.

While strong disorder, as in the Ba-family, converts the CE-CO-I in to a glassy state, it is natural to ask about the fate of the CE-CO-I state in presence of weak disorder. This will also provide valuable insight in the study of magnetic field melting of the CE-CO-I state in materials where disorder is inevitable.

Small disorder and of phase separation: The 'low' disorder induced trapping in the metastable FM-M on field cycling for $La_{0.5}Ca_{0.5}MnO_3$ at low temperature, shown in Fig. 1.14.(a) and (b)-(i) points towards the non equilibrium nature of disorder effects. Recent experiments [55, 56, 57, 58, 59, 60] have probed the nature of such nonequilibrium phenomena both at half doping [56, 57, 59] and away from half doping [55, 60] on weakly disordered (Ca-family) [59] and intermediate disorder (Sr-family) [56] using real space imaging as well as bulk indicators like magnetization. Unfortunately, real space data is

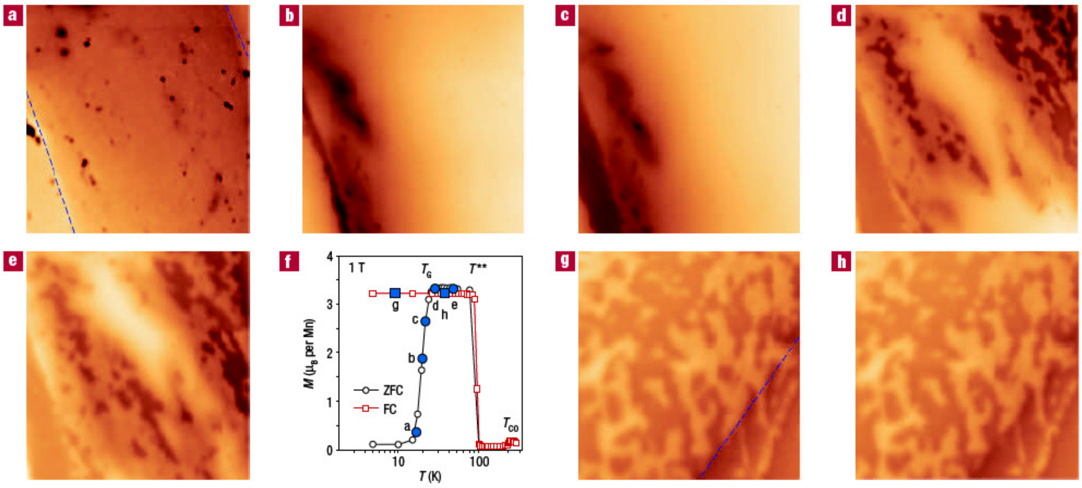

Figure 1.16: Magnetic force microscopy (MFM) images and magnetization. (a-e), g, h, MFM images taken at two locations during field warming (FW) (at 1 Tesla) around glass transition temperature (T_G) after zero field cooling (ZFC) (a-e) and field cooling (FC) (g,h), respectively. The magnetic field is out-of-plane. (f) Temperature dependence of the magnetization (M vs T) during FW after ZFC (open circles) and FC (open squares). The filled symbols mark the temperature of the corresponding MFM images. The glass transition occurs around $T_G \sim 25K$ where the ZFC-FW curve rises sharply to approach the FC-FW curve. The MFM images taken across the glass transition during FC-FW show a relatively *static* phase pattern with a large FM-M volume fraction (which develops during FC). Some CO domains (bright contrast) on the sample surface are visible in these images, indicating an incomplete transformation to the FM-M state. Note the dark regions are FM-M while the bright are AF-CO. (From W. Wu *et. al.* , Nat. Mater., **5**, 881, (2006).)

not available at present for half doped cases. While we will discuss the measurements at half doping in Chapter.2, here we present the results on $La_{5/8-y}Pr_yCa_{3/8}MnO_3$ (LPCMO) [55, 60]. The general conclusions hold at half doping [56, 57, 59] as well, as will be discussed in Chapter.2.

LPCMO has small cation mismatch, so disorder is small. It has a state that is mostly AF-CO at high temperatures [60], and a phase coexistent state (small randomly oriented FM-M clusters in AF-CO matrix) at low T [55, 60]. The experiment on LPCMO, that we discuss, comprises of cooling the system at various fields starting from $h = 0$ and through imaging the magnetic pattern on the lattice, infer about the volume fractions of the AF-CO and FM-M phases found in the system. It also images the magnetic pattern during warming the sample in a fixed field, for samples previously cooled at various cooling fields.

Fig. 1.16 shows a series of real space snapshots of the magnetic state in LPCMO during field warming (FW) for both zero field cooled (ZFC) and field cooled (FC) samples. Fig. 1.16.(f) shows the magnetization for these, the points corresponding to the snapshots are denoted by ellipses. The ZFC data in (f) shows a sharp rise in magnetization around the T_G on warming the sample in 1 Tesla field. This correlates with the real space image showing a significant increase in the FM-M fraction (dark regions). Note that the FM-M regions tend to grow into stripelike structures during the transition due to strain effects. For this choice of warming field (1 Tesla), some CO regions *persist* above T$_G$ (bright colour at the top centre of the frame in Fig 1.16.(d) and (e). In contrast, the FC-FW images Fig 1.16.(g) and (h) spanning the *same* temperature range show a relatively static local phase configuration. We thus see that one gets different amounts of FM-M and AF-CO regions at low T (below T_G), by initially cooling in zero and 1 Tesla fields. Infact, as is concluded in the paper, the coexisting volumes of the AF-CO and FM-M at low T can be tuned continuously by cooling the system in different magnetic fields.

While, conventional trapping in metastable states can be gotten rid off by waiting long enough, in the present case, the FC coexistent state persists at low T even when the cooling field is isothermally set to zero. Thus, the tunneling time to the ZFC state becomes macroscopic in the presence of weak disorder.

The temperature which marks the onset of this multivalued 'long lived' coexistent state is defined as the glass transition temperature. This is denoted by T$_G$. While we will discuss this glassy state in some detail in Chapter.2, here we mention that the existence of the glassy state in LPCMO had been established through transport studies earlier [42, 61].

These results allow one to make the following observations (i) the real space data shows that at weak disorder, the CO or FM correlations in the ground state although not long range, is not broken down to atomic scales, (ii) below T$_G(H)$, the magnetization of the sample is not unique, due to trapping in metastable states, and (iii) that the low T, path dependent 'tunable' coexistent state has macroscopic life times. As we will see in Chapter.5, such disorder assisted trapping in metastable states nearby in the free energy landscape play an important role in understanding the field melting of the half doped CE-CO-I state too.

To summarize, we have seen that by changing doping and bandwidth one can tune a system close to a phase boundary and drive a phase transition. We also saw that hole doping inevitably introduces A site disorder, unless very special techniques are used. Moreover, given the correlation between different degrees of freedom, most visible at half doping, applying a magnetic fields coupling to the core spins, can nontrivially affect charge, orbital and lattice degrees of freedom. Disorder can also lead to nonequilibrium coexistent states, with tunable phase fractions. Given the difficulty of exploring the entire parameter space, we opted to stay at half doping and explored the effects of bandwidth variation, disorder, thermal fluctuations, and an applied magnetic field on the ordered states at this filling. Our primary focus is on the complex CE-CO-I state, and we study the problem using an essentially exact Monte Carlo technique.

1.5 Plan of the report

We discuss the key experimental results in Chapter.2. In Chapter.3 we discuss the model and the method of solution. This is followed by the results on the magnetic field melting of charge order in 'clean' half doped manganites, in Chapter.4. Chapter.5 discusses the results of charge order melting in disordered systems. We conclude the thesis in Chapter.6.

Chapter 2

Phenomenology of the charge ordered state

Chapter summary: In this chapter we discuss the nature of the CE-CO-I ground state in the low and intermediate bandwidth half doped manganites. We identify control parameters that destabilize the CE-CO-I ground state, discuss the neighbouring metastable states, and organise the experimental data for comparison with theory. We begin with a discussion of the CE-CO-I state in 'clean' systems, and then examine the origin and types of disorder that affect the CE-CO-I and competing states. We show how 'A-site' disorder is quantified, and classify materials according to the extent of disorder. We discuss the effects of A-site disorder on the ordered states, the response of the CE-CO-I state to an applied magnetic field and, finally, disorder effects on the kinetics of the first order phase transition. We end with a summary of the experimental issues that this thesis seeks to address.

2.1 The zero field state

Fig. 2.1 shows results that are typical on cooling a low bandwidth half doped manganite. The left panel shows the evolution of resistivity (ρ) with temperature for $\mathrm{Pr_{0.5}Sr_{0.5}MnO_3}$. The right panel shows the variation of magnetization with temperature. In the left panel, the system is paramagnetic (PM) above T_c. There is a rapid drop in $\rho(T)$ on cooling below T_c, but an abrupt increase and insulating behaviour for $T \leq T_\nu$. The resistivity anomalies at T_c and T_ν are accompanied by changes in the magnetization as shown in the right panel. The zero field magnetization (open squares) show that between T_c and T_ν the

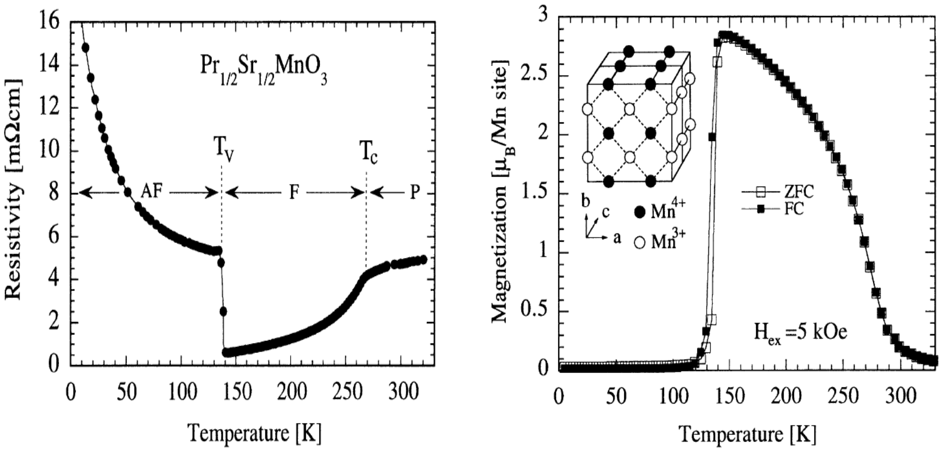

Figure 2.1: Left: The temperature dependence of resistivity (along the c axis) in absence of magnetic field for $Pr_{0.5}Sr_{0.5}MnO_3$ crystal. P for $T > T_C$, F for $T_\nu < T < T_C$ and AF for $T < T_\nu$, denote paramagnetic, ferromagnetic and antiferromagnetic states respectively. Right: The zero field cooled (ZFC; open squares) and field cooled (FC; filled squares), at $5kOe$, magnetisation. Inset shows the feature of the charge ordering in which only the Mn sites are shown from neutron diffraction on polycrystals. (From, T. Nakajima, *et. al.* J. Phys. Soc. Jpn. **71**, 2843 (2002).)

magnetization grows with reduction in temperature, but drops almost discontinuously to zero at T_ν. The low temperature state is an antiferromagnetic insulator, to which the system makes a abrupt transition at T_ν. We will see later, Fig. 2.9, that thermal cycling on this leads to hysteresis around T_ν, confirming that the transition is first order in nature. Moreover, the spatial nature of the insulating state, as inferred from neutron diffraction [36], shows a checkerboard organization in the $a - b$ crystallographic plane, with stacking along the c axis. This is shown in the inset of the right panel, Fig. 2.1. The intermediate temperature ferromagnetic metal (FM-M) is the major competitor of the CE-CO-I phase. For now, however, let us focus on the CE-CO-I state.

Based on the early experimental work [62, 63, 64] and theoretical analysis [65], the schematic spin-charge-orbital ordered state at half doping is depicted in Fig. 2.2. It shows the planar order in the $a - b$ plane. Panel (a) shows the alternating $\{\mathbf{q} = \pi, \pi\}$ charge order. (b) Shows the zig-zag ferromagnetic chains coupled antiferromagnetically with each other. The magnetic structure factor has peaks at $\mathbf{q} = \{0, \pi\}$, $\{\pi, 0\}$, and $\{\pi/2, \pi/2\}$. Panel (c) shows the alternate $d_{3x^2-r^2}/d_{3y^2-r^2}$ orbital occupancy (on sites with

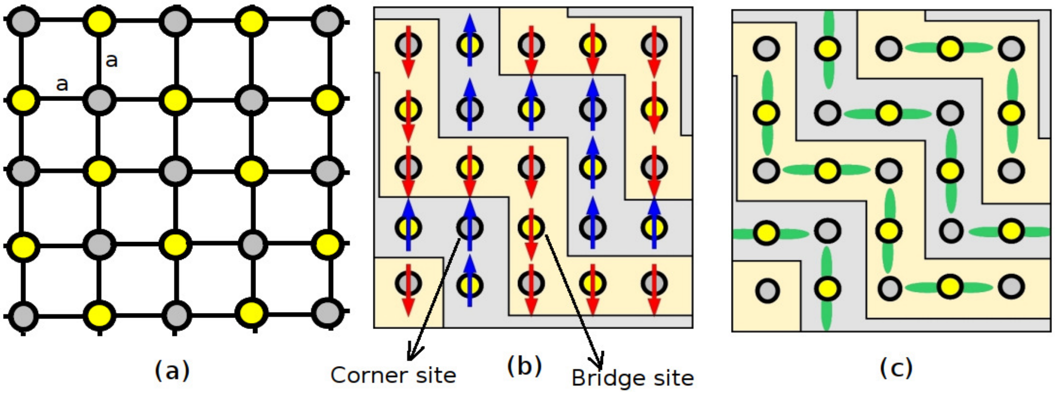

Figure 2.2: Schematic of the CE-CO-I state. (a) The in-plane checkerboard charge order for low bandwidth half doped manganites. The yellow filled positions depict Mn sites with larger charge disproportionation $3.5 + \delta$ and the grey ones with $3.5 - \delta$. (b) The accompanying CE-type magnetic order with zigzag ferromagnetic chains coupled antiferromagnetically and (c) the concomitant orbital order consisting of alternate $d_{3x^2-r^2}/d_{3y^2-r^2}$ orbital occupancy on sites with larger charge disproportionation δ.

larger charge density). While the same charge and orbital pattern is stacked in the c direction, the zig-zag FM chains are antiferromagnetically ordered in alternating planes along the c direction.

In a departure from Goodenough's picture [65] the $\{\mathbf{q} = \pi, \pi\}$ charge order is not alternating Mn^{3+} and Mn^{4+} but 'softer'. The charge modulation is $0.5 - \delta/0.5 + \delta$, with $\delta \sim 0.2$. This is estimated mainly through model calculations with the inclusion of Coulomb interactions [5, 66, 67] and Jahn-Teller phonons [6, 68].

This CE-CO-I state involves cooperative ordering of the spin, charge, lattice and orbital degrees of freedom, and the kinetic energy and localization tendencies are delicately balanced. It is reasonably easy to destabilize the CE-CO-I state by a host of agencies, both 'internal' and 'external'. The internal control parameters are bandwidth (BW) and disorder, while the main external ones are magnetic field, temperature and pressure. The next subsection is devoted to the effects of varying BW and temperature on the A site 'ordered' half doped manganites. After that we introduce the different sources of disorder and discuss the effect of BW variation for different degrees of disorder. We discuss results on the magnetic field response of the CE-CO-I at the end.

2.1.1 Bandwidth dependence

Let us first discuss how the bandwidth can be tuned in the manganites. The undoped manganite, $AMnO_3$, where A is a rare earth (RE) element, is hole doped using alkaline earth elements (AE). At half doping the manganites have a chemical formula $A_{0.5}A'_{0.5}MnO_3$. We will discuss several 'families' of manganites. For example the Ca family at half doping has the general formula $Ln_{0.5}Ca_{0.5}MnO_3$. The most investigated are the Ca, Sr and Ba families, with Ln, the RE element, being La, Pr, Nd, Sm, Eu, Gd, Tb, Ho and Y. These Ln ions have their radii either close to the AE element or are smaller. The radii for these RE and AE elements are given in Table 1.

Ca	Sr	Ba						
1.34	1.44	1.61						
La	Pr	Nd	Sm	Eu	Gd	Tb	Ho	Y
1.36	1.29	1.27	1.24	1.23	1.21	1.20	1.18	1.18

Table 2.1: Ionic radii (in Angstroms) for various AE^{2+} and RE^{3+} ions in the perovskite manganites. (From Tokura Y., Rep. Prog. Phys. **69**, 797 (2006).)

For these materials the mean ionic radius is $r_A = (1/2)(r_{RE} + r_{AE})$. When one substitutes A' in place of A the radius mismatch leads to change in the electrostatic and elastic forces and, in the new equilibrium structure, there is some tilting of the MnO_6 octahedra. Moreover as discussed in Chapter.1 the Mn-Mn hoping integral between two neighbouring sites varies as $cos^2(\theta)$, where θ is the Mn-O-Mn bond angle. Thus, with half of the A ions replaced by A' randomly, there will be a suppression of the average hopping amplitude. The local fluctuation of the hopping amplitude about the mean value is a source of disorder. For a fixed A', Ca say, if we consider the $Ln_{0.5}Ca_{0.5}MnO_3$ family, the smaller the dopant radius, the greater the tilt and larger the suppression of the BW. As a rule of thumb, within a family (defined by a fixed A'), smaller r_A or r_{AE} imply smaller BW while larger r_A or r_{AE} imply larger BW.

Remarkably, it has been possible to synthesize samples that avoid the disorder above. This is due to the recent ability [49] to create A-A' *ordered* half doped materials with alternate stacking of $AMnO_3$ and $A'MnO_3$ planes. One can tune the BW by using different AE dopants in a given RE family, still avoiding disorder! This allows access to detailed

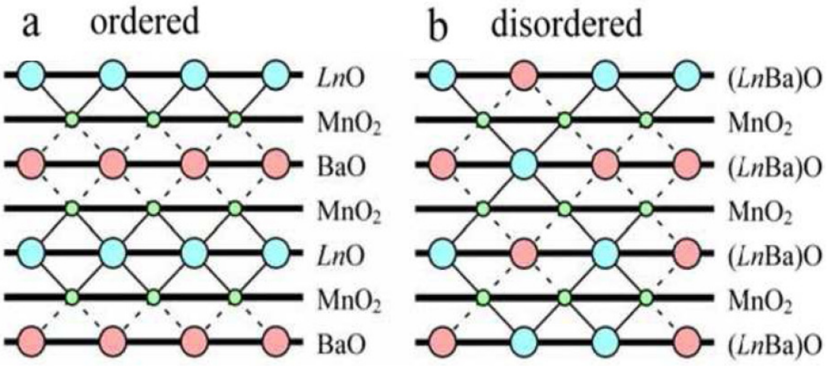

Figure 2.3: Schematic structures of half-doped perovskite, $Ln_{0.5}Ba_{0.5}MnO_3$, viewed along the b axis: (a) the A-site ordered perovskite with the alternate stack of LnO and BaO layers along the c axis, and (b) the A-site disordered (solid-solution) perovskite with cubic structure. (From D. Akahoshi, *et. al.* Phys. Rev. Lett. *90*, 177203 (2003).)

material systematics, uncomplicated by effects of disorder. We turn to these now.

It is known that at large BW, the half doped systems prefer to be ferromagnetic metals, because the energy gain from electron delocalization is larger than that obtained by localization. The FM-M state is preferred at large r_A. At low r_A, localization tendencies and the commensurate (half) filling leads to the insulating CE-CO-I phase. By varying r_A one can conveniently tune the system from a FM-M to a CE-CO-I state. This is achieved by making separate materials with appropriately chosen A so that with each different A there occurs an incremental change in the average ionic radii.

Fig. 2.3.(a) shows the schematic structure of the 'ordered' $Ln_{0.5}Ba_{0.5}MnO_3$ samples as opposed to the random substitution of the dopant A (Ln), as shown in Fig. 2.3.(b), from a recent experiment [49]. Let us start with the ordered case, and take up the disordered case in the next section. Fig. 2.4 shows the $r_{Ln} - T$ phase diagram from the above experiment.

For the ordered structure, r_A variation can be used to tune the BW. The $r_{Ln} - T$ phase diagram shows the various low temperature phases, their thermal evolution, and locate the critical Ln radius (hence r_A) below which the manganite will have a CE-CO-I ground state. Since decreasing r_A reduces BW, the x-axis of Fig. 2.4 also indicates the evolution of the CE-CO-I state with varying BW. Also note, while Fig. 2.4 uses r_{Ln} to plot the phase diagram, we prefer to describe the trends in terms of the average cation

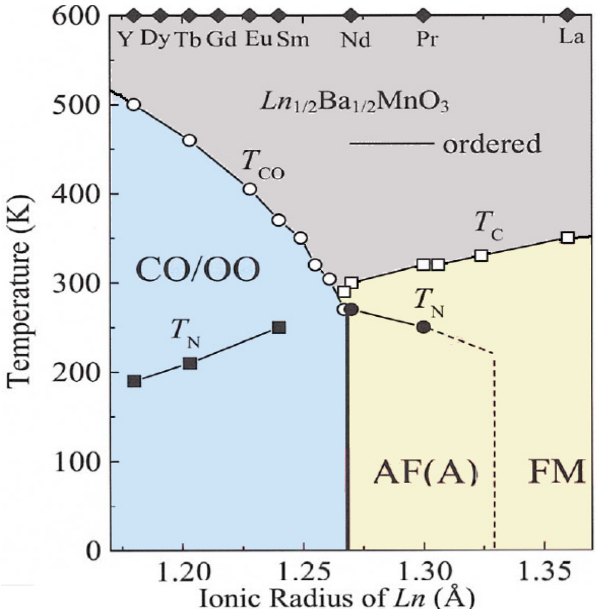

Figure 2.4: Electronic phase diagrams for the A-site ordered (black line and symbols) perovskites with half doping $Ln_{0.5}Ba_{0.5}MnO_3$, as a function of the ionic radius of Ln. CO/OO and FM stand for the charge/orbital ordered and ferromagnetic states, respectively. T_{CO} and T_C represent the respective transition temperatures. The data for the mixed crystal compounds with Ln=(Nd, Sm) and (La, Nd), is also shown. On the CO/OO side, the T_N refers to the CE ordering temperature. (From D. Akahoshi, *et. al.* Phys. Rev. Lett. **90**, 177203 (2003).)

radius r_A.

With increasing r_A, the system remains in the CE-CO-I state up to Ln=Nd. Beyond this, at low temperature, the system has an A-type magnetic ground state with no long range CO but insulating character. For even larger r_A (beyond Ln=Pr) the half doped system prefers a FM-M state. The various transition temperatures are indicated in the figure. With reducing r_A the temperature T_N for CE magnetic order decreases but the T_{CO} increases. The temperature window of CO-OO without any CE order grows with decreasing r_A. This indicates that the CO state is more stable with decreasing r_A and may be stable even *without the CE magnetic background* below some critical r_A. All the phase boundaries shown are first order.

The above summarizes the response of the ordered half doped manganites to bandwidth variation. We discuss the effects of disorder in the next section.

2.1.2 A site disorder

The most common kind of disorder arises from the A-site substitution that is done to control the doping. The other sources of disorder are those due to B site substitution and due to oxygen vacancies. While we have done work on the effects of both A and B site disorder this thesis will concentrate on the effects of A site disorder.

For a fixed AE ion, changing the Ln atom changes both the bandwidth and the cation size mismatch σ_A, varying the structural disorder. The disorder arises, in the first place, because random substitution of RE by AE randomizes the local hopping [11]. The other possible effect is from the different ionic environment of different Mn ions in the randomly substituted background. This can generate a scattering potential on the Mn site via short range Coulomb interaction with the neighbouring A, A' ions.

The disorder is experimentally quantified via the A site variance $\sigma_A = \langle r_A^2 \rangle - \langle r_A \rangle^2$ [71, 72]. Employing this as a measure, careful experiments [73, 72, 74] have mapped out physical properties for varying r_A and σ_A, at a fixed doping level.

Fig. 2.5 shows the $\sigma_A - r_A$ plot at $x = 0.45$, for the Ca, Sr and Ba families. While the data is for $x = 0.45$, the results would be similar for $x = 0.5$. From the figure we see that there is a systematic increase in disorder as one changes from Ca to Sr to Ba (keeping the RE ion fixed) or on reducing the RE ion size keeping the AE ion fixed. The Ba based materials have the largest $\sigma_A \sim 10^{-1} A^2$. As explained below in the context of Fig. 2.6, this amount of disorder completely kills CE-CO-I order and weakens the FM-M state. Based on the σ_A values we can classify the three families as follows:

- The Ca based manganites have low disorder ($\sigma_A \sim 10^{-3} A^2$), for us they will define the ‘clean’ limit.
- The Sr based materials have intermediate disorder, with $\sigma_A \sim 10^{-2} A^2$. The disorder suppresses but does not destroy CE-CO-OO.
- The Ba based manganites are strongly disordered, and destroy CE-CO-OO.

We will describe the effect of weak and intermediate disorder further on, let us examine the effect of strong disorder here. Fig. 2.6 shows the same $r_{Ln} - T$ phase diagram [49] as in Fig. 2.4, for the disordered half doped Ba family as shown in the schematic Fig. 2.3.(b).

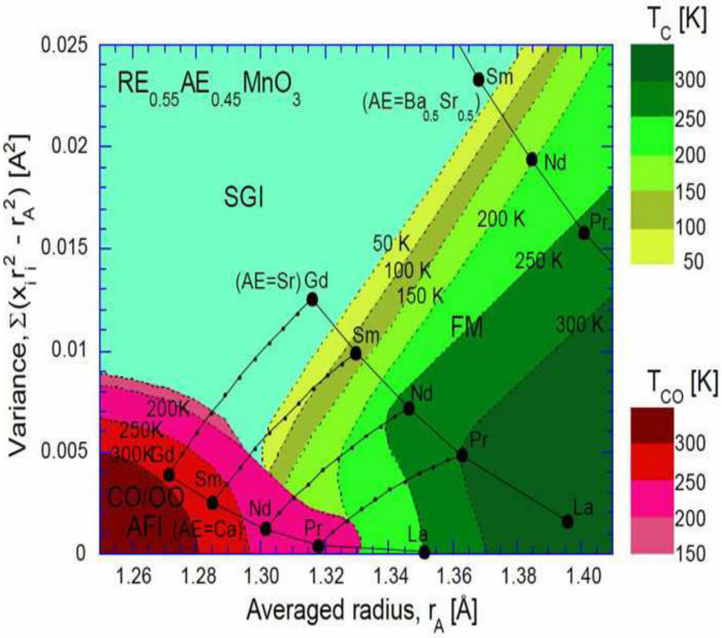

Figure 2.5: The electronic phase diagram of various $\mathrm{RE}_{1-x}\mathrm{AE}_x\mathrm{MnO}_3$ $x = 0.45$ crystals in the plane of r_A and σ_A. Apart from standard abbreviations SGI stands for spin glass insulator. Most data are from measurements on single crystal samples. Notice that among the three families for which data is shown, Ba has the highest disorder, then Sr family and finally the Ca family. Moreover within each family disorder increases with decreasing r_A or greater size mismatch. (From Tokura Y., Rep. Prog. Phys. *69*, 797 (2006).)

For comparison, in Fig. 2.6, the disordered system data is superposed on the clean data. The T_{CO} is about $500K$ for the A site *ordered* samples of $\mathrm{Y}_{0.5}\mathrm{Ba}_{0.5}\mathrm{MnO}_3$, which has the smallest r_A, and decreases with increasing RE ionic size. On the other hand, the T_C decreases with decreasing RE size. T_{CO} and T_c are roughly equal for Ln=Nd, defining the 'bicritical' point. The disordered samples have their ferromagnetic T_c suppressed with respect to the A site ordered case. For Ln=Nd T_c is suppressed the most on disordering. Further, for low r_A materials with Ln=Sm-Dy, the disorder converts the CE-CO-I state to a nanoscale correlated glass below 50K as observed [49, 54] in the frequency dependence of the ac susceptibility. Among them, x-ray diffuse scattering [54] yields the correlation length of charge and orbital order to be $\sim 2nm$ in the glass. Thus, the "phase separation" in presence of strong A-site disorder is in the nanoscale regime. As a starting point for our calculation we have reproduced this result. This will be discussed in Chapter.4.

We now discuss the cases where the disorder is not so detrimental to the CE-CO-

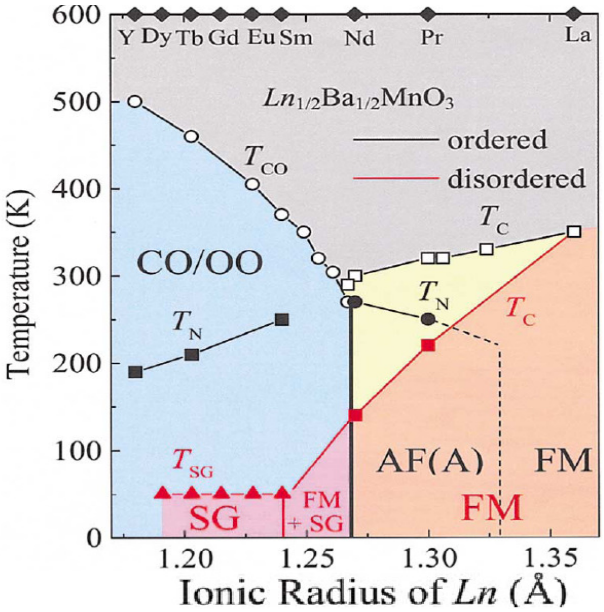

Figure 2.6: Electronic phase diagrams for the A-site ordered (black line and symbols) and disordered (red line and symbols; the region shaded in red) perovskites with half doping $Ln_{0.5}Ba_{0.5}MnO_3$, as a function of the ionic radius of Ln. CO/OO, FM, and SG stand for the charge/orbital ordered, ferromagnetic, and spin-glass states, respectively. T_{CO}, T_C and T_{SG} represent the respective transition temperatures. The data for the mixed crystal compounds with Ln=(Nd, Sm) and (La, Nd), both Ln=Ba ordered and disordered, are also shown. (From D. Akahoshi, *et. al.* Phys. Rev. Lett. **90**, 177203 (2003).)

I state, *i.e* the Ca and Sr based manganites. As was indicated by real space data in $(LaPr)CaMnO_3$ in Chapter.1, and experiments on half doped systems with weak disorder [50], the CE-CO-I state survives for a range of r_A values (or bandwidth). The same holds even for intermediate disorder. However, the effect of A-site disorder shows up in the response to temperature and magnetic fields. We turn to these in the next section.

It is pertinent to ask about the real space nature of the CE-CO-I state at weak and intermediate disorder for these systems. Fig. 2.7 shows the spatial images of $La_{0.5}Ca_{0.5}MnO_3$, at three different temperatures. The bright regions are the CO regions that grow with reducing temperature at the expense of the dark (FM-M) regions. In the first two panels, the coexistence of FM-M and AF-CO is visible, with typical domain sizes $\sim 20-30$nm above T_N, $\sim$ 135K, and 50-60nm just below T_N. Further below T_N, at $T \sim 95K$, the CO covers most of the lattice with some residual discommensurations. We will look at the fate of such states on field sweeping in the next section. Next, for

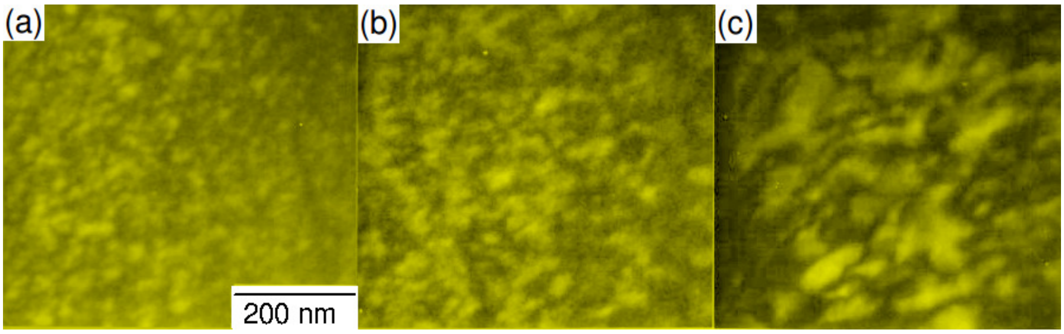

Figure 2.7: (a), (b) and (c) are dark-field images of $La_{0.5}Ca_{0.5}MnO_3$ obtained on cooling from a charge ordering superlattice reflection at temperatures of 142, 124, and 95 K, respectively. As the temperature is lowered, the charge-ordered domains with bright contrast grow in size at the expense of the ferromagnetic charge-disordered domains with dark contrast. The charge-ordered domain in (c) is nearly commensurate as indicated by electron diffraction and residual discommensurations (wavy dark lines) with 70 nm spacing are visible, which considerably darken the contrast of the domain. (From S. Mori, *et. al.*, Phys. Rev. Lett. **81**, 3792 (1998).)

completeness, we will briefly discuss the effect of another kind of disorder due to Mn-site substitution in the manganites.

2.1.3 B site disorder

The zero field metallisation of insulating $Pr_{0.5}Ca_{0.5}Mn_{1-y}Cr_yO_3$ by doping small percentage of Cr at the Mn site started a lot of activity in this direction. It was soon realised that choosing a correct undoped (reference) state i.e., y=0 state and a proper B-site dopant can lead to dramatic effects such as generation of CO from metallic ferromagnets, and novel phase separated states, apart from easy metallisation of insulators. Let us report some of the most important experimental results. Our theory results on these [75, 76] are not discussed in this thesis. The results are reported in the PhD thesis of K. Pradhan from HRI.

B-site doping on the CE-CO-I state: Fig. 2.8.(a) [77] shows the dark field image of a sample at temperature below the CO and CE transition temperatures for 3% of Cr doping in $Nd_{0.5}Ca_{0.5}MnO_3$. The coexistence of FM and CO domains is clearly visible. In the sample without Cr doping the system is a CE-CO-I insulator. Fig. 2.8.(b) [78], shows

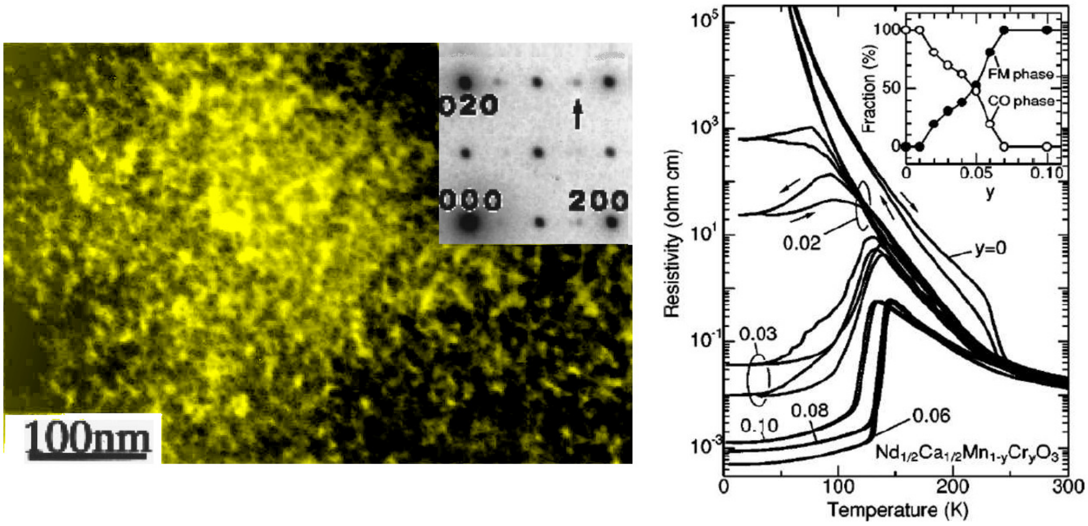

Figure 2.8: (a) Dark field image at 120K (below the transition temperature) for $Nd_{0.5}Ca_{0.5}Mn_{0.97}Cr_{0.03}O_3$. The bright and dark contrast corresponds to the CO and FM domains respectively. (From Y. Moritomo, *et. al.* Phys., Rev. **B 60**, 9220 1999) (b) Different amounts of Cr doping of $Nd_{0.5}Ca_{0.5}MnO_3$, showing temperature dependence and resistivity. Inset: Fraction of FM and CO phase at 30K. (From T. Kimura, *et. al.*, Phys. Rev. **B 62**, 15021 (2000).)

the resistivity vs temperature, for various amounts of Cr doping. Clearly, beyond 2%, the resistivity falls drastically and there is a insulator to metal transition.

The inset shows the volume fraction of the CO and FM regions as a function of Cr doping. These volume fractions are inferred from the structural data in the experiment. Even if we keep the reference state same i.e., the CE-CO-I at half filling, B-site dopants of different valence state are known to have different effects. For example, among +2 and +3 valence state B-site dopants (Al, Zn, Sc, Fe, Ni, Co and Ca) only Cr, Ni and Co are able to create a FM-M out of the CE-CO-I state. Some of these dopants are magnetic while others are non magnetic. Among the non magnetic ones some have full d-shell and others are without d electrons[79].

B-site doping on other states: Counter-intuitive effects of B-site disorder are also seen by choosing other reference states. For example, we saw that although A-site disorder suppresses the T_c in the FM-M state, it does not destroy the metallicity or the FM character, only weaken it. However, B-site doping can convert the FM-M to an insulator.

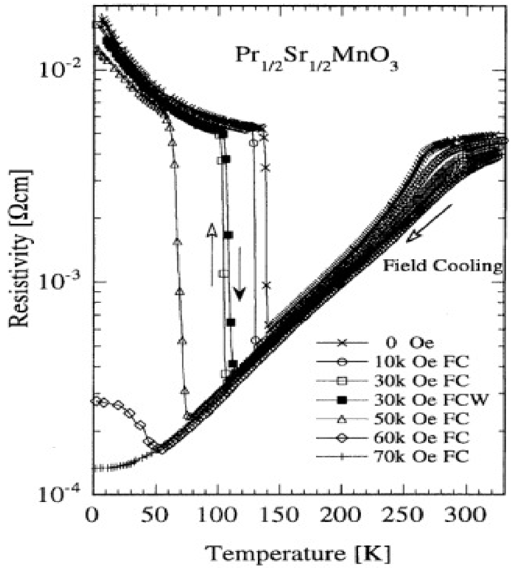

Figure 2.9: Temperature dependence of resistivity for $Pr_{0.5}Sr_{0.5}MnO_3$ for sample cooled in various magnetic field values. The resistivity was measured from 330K to 4.2K under the cooling magnetic field. For the data at 30kOe, both field cooled(FC) and field-cooled warming(FCW) runs are shown. The hysteresis in the FC and the FCW runs indicate the first order nature of the thermal transition. Also notice that beyond the cooling field of 50kOe, there is a drastic change in the resistivity, signalling the inability of formation of the CE-CO-I state. (From Kimura T, *et. al.*, Phys. Rev. **B 62** 15021, (2000).)

Metal to insulator transition has also been observed in experiments on Fe doping in $La_{0.77}Ca_{0.33}MnO_3$ and Mg doping in $Pr_{0.7}Ca_ySr_{1-y}MnO_3$. That these metal to insulator transitions are not due to disorder driven localization has been established by observation of microdomains of CO regions. This implies that such B-site disorder driven metal-insulator transition is caused by transforming the FM-M to a charge ordered state!

While we will not go into further details of these experiments, it is clear, that B-site disorder can convert a CO-I to a FM-M and an FM-M to a CO-I, moreover not all dopants have same effect on the chosen reference state. The valence state of the B-site dopant, its magnetic character, and local Coulomb interactions with the neighbouring Mn sites, have been shown [75, 76] to be crucial in understanding the experiments.

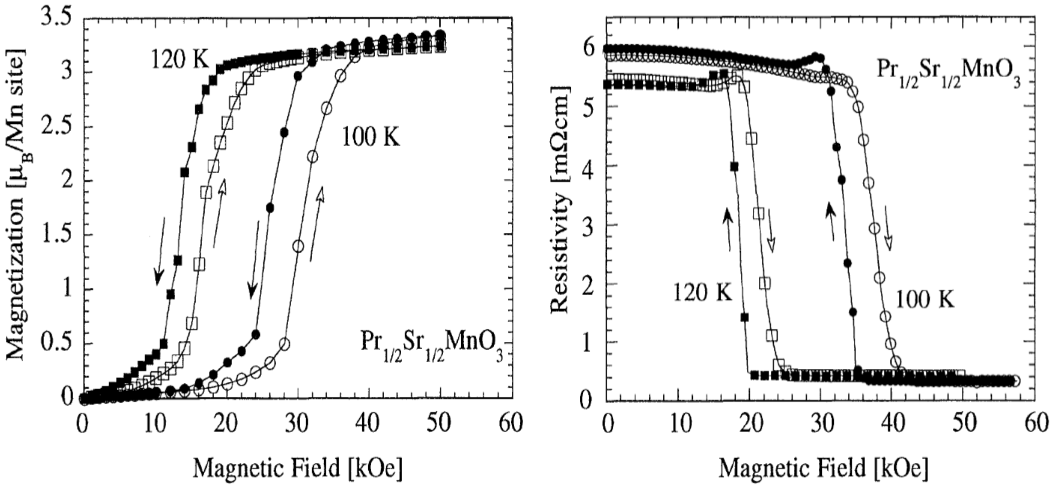

Figure 2.10: Magnetization (left) and resistivity (right), for $\mathrm{Pr_{0.5}Sr_{0.5}MnO_3}$, at 100K and 120K.as a function of magnetic field. Hysteretic response and abrupt first order like transitions are clearly seen in both cases. Also, the collapse of the magnetization is concurrent with the loss of insulating nature, implying magnetic field induced melting of the CO state. (From Kimura T, *et. al.*, Phys. Rev. **B 62** 15021, (2000).)

2.2 Magnetic field response

Given the 'CMR' character of the manganites, there has been significant effort in understanding the field response of these materials at all doping levels, including the insulating CE-CO state. The first report [83] on the magnetic field induced melting of charge order at half doping was followed by several other studies [84, 85, 86]. The intimate coupling of the spin, charge, lattice and orbital degrees of freedom in the CE-CO-I state offers an opportunity to destabilize the CO state by affecting the CE order via a magnetic field. This is at the heart of magnetic field induced melting of charge order.

We looked at one such example in Chapter.1 for $\mathrm{La_{0.5}Ca_{0.5}MnO_3}$. Here let us look at $\mathrm{Pr_{0.5}Sr_{0.5}MnO_3}$, that has a smaller BW. The zero field resistivity and magnetization were shown in Fig. 2.1. Fig. 2.9 shows the resistivity for $\mathrm{Pr_{0.5}Sr_{0.5}MnO_3}$, when the system is cooled at various fixed magnetic fields. Clearly, for cooling fields greater than 50kOe, the magnetic field does not allow formation of the long range CE-CO state and the system remains metallic. Note however, that there can still be short range CE-CO patches that remain in the FM-M after field cooling.

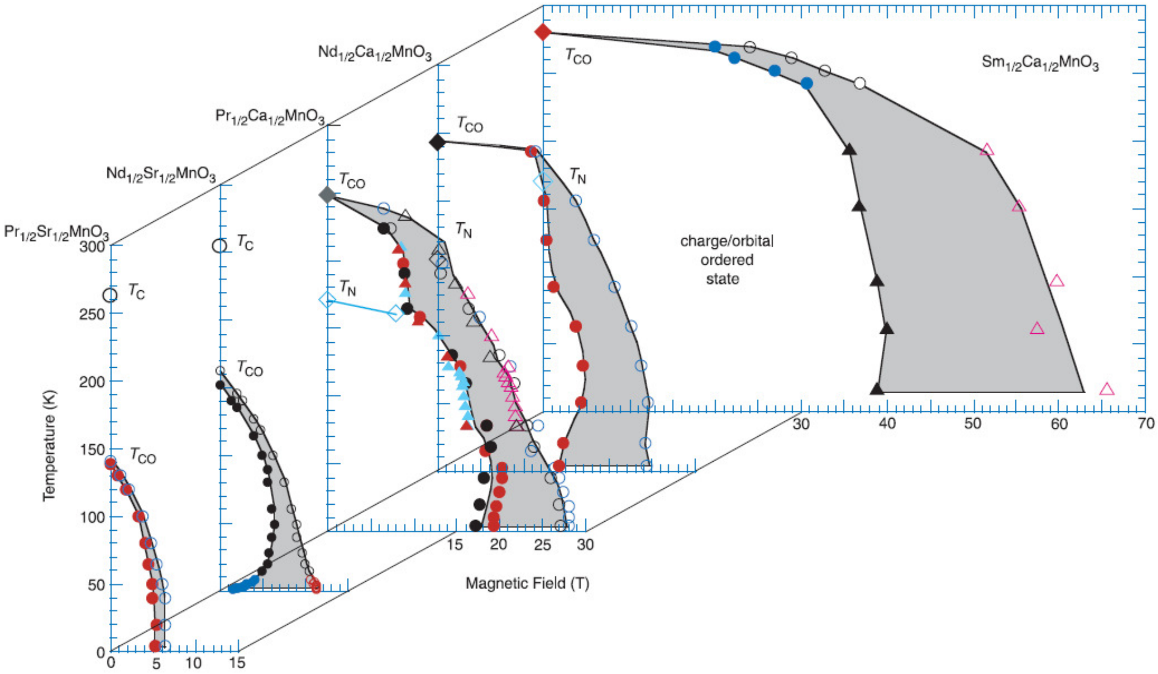

Figure 2.11: The $h-T$ phase diagram of various $RE_{1/2}AE_{1/2}MnO_3$ compounds [69]. The materials involve a systematic decrease in r_A from $Pr_{0.5}Sr_{0.5}MnO_3$ to $Sm_{0.5}Ca_{0.5}MnO_3$. The critical CO melting temperature increases with decreasing r_A. The window of metastability associated with the first order transition tapers with increase in temperature and vanishes at T_{CO}. The Ca family has low disorder and shows re-entrant behaviour in h_c^-, which vanishes at very low bandwidths ($Sm_{0.5}Ca_{0.5}MnO_3$) (SMCO). Further, in the Ca family, the decrease in r_A, also makes the CO state more robust, with SCMO having the largest melting fields. The Sr family has larger disorder (see text) with $Pr_{0.5}Sr_{0.5}MnO_3$ having larger r_A than $Nd_{0.5}Sr_{0.5}MnO_3$. While $Nd_{0.5}Sr_{0.5}MnO_3$ shows marked hysteresis, $Pr_{0.5}Sr_{0.5}MnO_3$ is rather benign. (From Tokura Y., Rep. Prog. Phys. **69**, 797 (2006).)

Systematic study of material trend show a clear contrast in how relatively clean and disordered materials of the same BW respond to a magnetic field. Moreover the field melting transition is first order in nature and experiments have been done to probe the window of hysteresis. The variation of the ‘melting field(s)’ with bandwidth and disorder provides comprehensive data for a theory to address. We start with the field response in the Ca based half-doped manganites, *i.e*, the case of weak A site disorder.

2.2.1 Weak A site disorder

Typical experiments [83, 84, 85, 86], that map out the hysteretic response of the CE-CO-I state to applied magnetic field, are done by cooling the system to a desired temperature in zero field and then applying a magnetic field. The magnetic field is hiked up at a constant rate to a maximum and then swept back to zero at the same rate. This gives us two critical magnetic field values, h_c^+ and h_c^-. These correspond respectively to the CO melting field on upward field sweep, and the field at which CO is 'recovered' on the downward sweep.

One example of such an experimental sweep is shown in Fig. 2.10. We also saw similar results for $\mathrm{La_{0.5}Ca_{0.5}MnO_3}$, where the CO was not recovered at low temperature after field sweep. This experiment on $\mathrm{Pr_{0.5}Sr_{0.5}MnO_3}$ clearly shows large hysteresis both in the magnetization, in (a), and the resistivity, in (b). Some experiments are also done by employing other field cooling and field warming protocols [55, 56, 57, 58]. We will however concern ourselves only with the protocol involving zero field cooling followed by field sweep at fixed temperature.

In the experimental results shown in Fig. 2.11, two lanthanide families have been extensively investigated, the Ca series $\mathrm{Ln_{0.5}Ca_{0.5}MnO_3}$ [84], and the Sr series $\mathrm{Ln_{0.5}Sr_{0.5}MnO_3}$ [85]. The key magnetic field-temperature $(h-T)$ phase diagrams are shown in Fig. 2.11. The materials probed have a monotonic decrease in r_A from $\mathrm{Pr_{0.5}Sr_{0.5}MnO_3}$ (PSMO) to $\mathrm{Sm_{0.5}Ca_{0.5}MnO_3}$. The figure shows that the melting field h_c^+ differ the most from the recovery field h_c^- when $T \rightarrow 0$. This window narrows and vanishes as $T \rightarrow T_{CO}$. The evolution of h_c^- has a 're-entrant' feature, $i.e$, reduction as $T \rightarrow 0$ in the larger BW materials. Further, reducing BW progressively increases the stability of the CO state, with $\mathrm{Sm_{0.5}Ca_{0.5}MnO_3}$ having the largest $h_c^{\pm}$ and T_{CO}.

While this provides the overall perspective, the Sr family has moderate amount of disorder. Let us organise the data in the Ca based manganites as our reference for BW dependence at weak disorder. For our purpose, we will consider this to be 'non disordered', $i.e$, clean, although weak disorder can have some effects on the kinetics of the melting transition. In Fig. 2.12 we present two such 'clean' $h-T$ phase diagrams that are representative of low and intermediate BW cases.

At low temperature h_c^+ is $\sim$ 20T for $\mathrm{La_{0.5}Ca_{0.5}MnO_3}$ and $\sim$ 30T for $\mathrm{Pr_{0.5}Ca_{0.5}MnO_3}$.

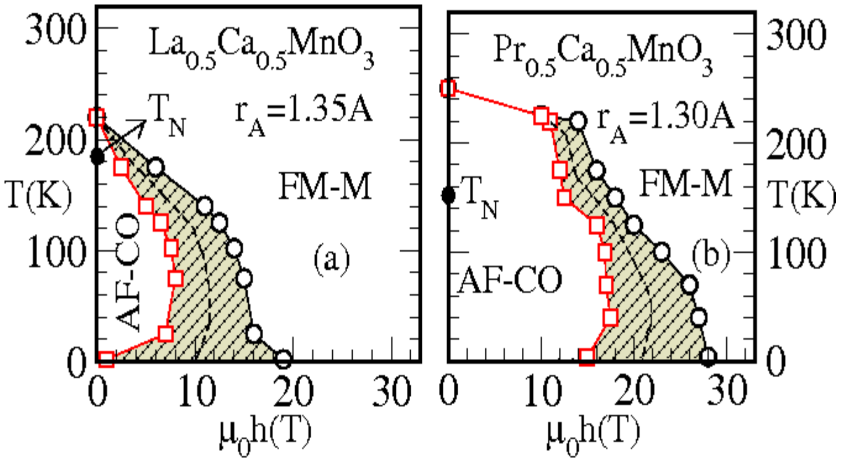

Figure 2.12: $h-T$ phase diagrams. (a)-(b) Experimental phase diagrams in (a) moderate BW $La_{0.5}Ca_{0.5}MnO_3$ and (b) narrow band $Pr_{0.5}Ca_{0.5}MnO_3$. The shaded regions show hysteresis Both FM-M and AF-CO-I states are locally stable in the shaded region. (From M. Respaud, *et. al.* Phys. Rev.**B 61**, 9014 (2000).)

The field h_c^-, at which CO is *recovered* on field reduction, is, however, $<$ 1T in $La_{0.5}Ca_{0.5}MnO_3$, but $\sim$ 15T in $Pr_{0.5}Ca_{0.5}MnO_3$. $h_c^- \sim 0$ at low temperature in $La_{0.5}Ca_{0.5}MnO_3$ indicates that the FM-M is metastable *even at* $h = 0$, while at smaller BW ($Pr_{0.5}Ca_{0.5}MnO_3$) the FM-M is no longer metastable at $h = 0$. The T_{CO} at $h = 0$ for these two systems are $\sim 220K$ and 250K respectively. This is expected, because, $Pr_{0.5}Ca_{0.5}MnO_3$ is further away from the bicritical boundary than $La_{0.5}Ca_{0.5}MnO_3$ which has a larger BW. For the later case the system might remain trapped at low T in the metastable FM-M, when the field is swept back to zero. However at $h = 0$, the FM-M becomes unstable for $Pr_{0.5}Ca_{0.5}MnO_3$ allowing the system to recover the CE-CO-I state.

Similar comparison among various 'clean' half doped materials lead to the material trends presented in Fig. 2.13. The data is extracted from experimental results [84]. It shows that variation of the critical melting fields with changing r_A for the Ca family. The increased stability of the CO state with decreasing BW, due to stronger electron localisation, is clearly seen in the increase in both T_{CO} and $h_c^{\pm}$ scales. The fall of T_{CE} with r_A is a hint of the growing stability of the CO state independent of CE magnetic order.

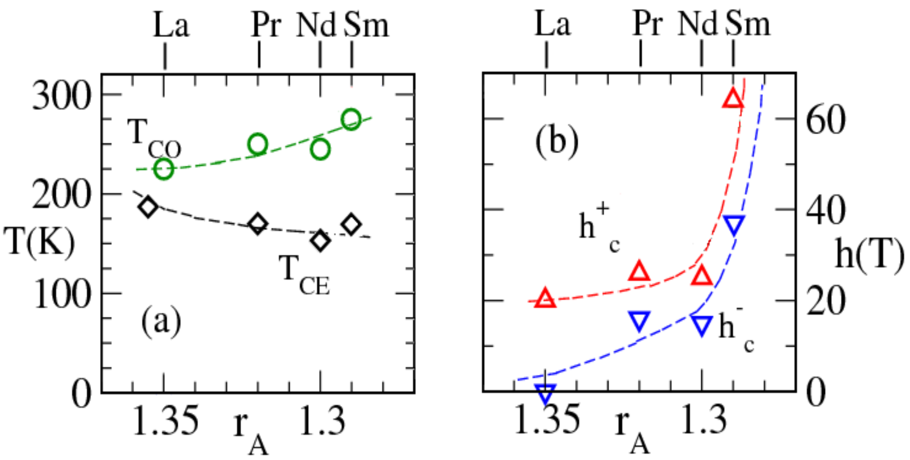

Figure 2.13: T_{CO}, and $h_c^{\pm}$ at low T. Data from experiments: the $\mathrm{Ln}_{0.5}\mathrm{Ca}_{0.5}\mathrm{MnO}_3$ family, with typical $\sigma_A \sim 10^{-3}A^2$, notionally we refer to this as the 'clean system. The lines are a guide to the eye. (From M. Respaud, *et. al.* Phys. Rev.**B 61**, 9014 (2000).)

2.2.2 Moderate A site disorder

The Sr family is our example of moderately disordered half doped manganite. Fig. 2.14 shows that variation of the critical melting fields with changing BW for the Sr family [85]. In marked departure from the BW dependence of $h_c^{\pm}$ and T_{CO} in the Ca family, these scales collapse for Ln=Sm! In the Ca family with reducing r_A these scales grew and in fact were largest for Ln=Sm (Fig. 2.13). This implies that the BW or r_A is *not the only controlling factor* deciding the fate of the $x = 0.5$ state. Disorder effects need to be understood in order to explain these results.

2.3 Disorder effects on kinetics

Recent experiments have explored another aspect of weak and intermediate disorder, *i.e*, disorder induced nonequilibrium coexistent states. In Chapter.1 we saw that during field cooling of LPCMO, the higher temperature AF-CO (micro)phases are trapped at low temperature forming a glassy state. At half doping, as we discuss below, both in weak (Ca) and intermediate (Sr) disorder families, the higher temperature FM-M regions may be trapped in the low temperature CE-CO-I. These disorder induced coexistent states

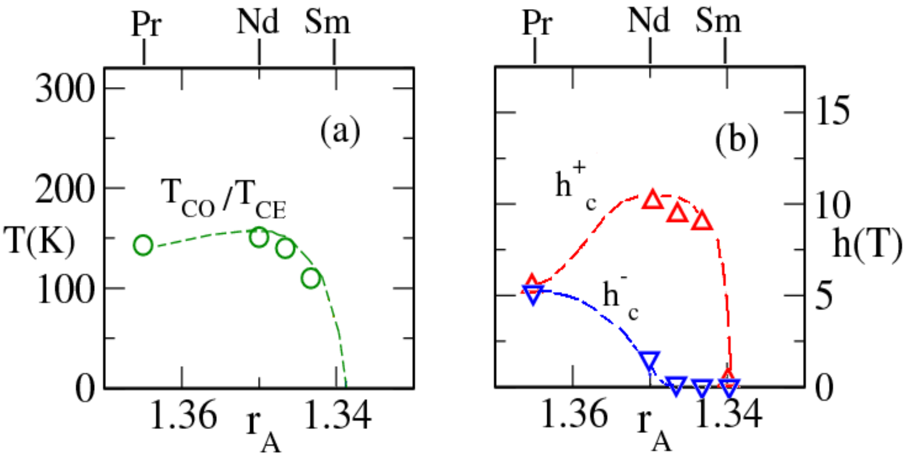

Figure 2.14: T_{CO}, and $h_c^{\pm}$ at low T. Data from experiments: the $Ln_{0.5}Sr_{0.5}MnO_3$ family, that is moderately disordered. The lines are a guide to the eye. (From Y. Tokura, *et. al.* Phys. Rev. Lett. **76**, 3184 (1996).)

remain stable, below a critical temperature T_G, even when the external cooling field is isothermally set to zero. This is due to blocking of the kinetics. Further, the coexistent phases volumes can be tuned.

Fig. 2.15.(a) shows the magnetization of low disorder, $La_{0.5}Ca_{0.5}MnO_3$, samples, that were cooled in 1 Tesla field (blue ellipses) and in a magnetic field of 6 Tesla. These samples were cooled from 320K down to 5K and the magnetic field of 6T is set to 1T, isothermally, at 5K for the 6T cooled sample. Then both the 1 Tesla field cooled sample and the 6T cooled sample were warmed in the 1 Tesla field, depicted by the red line and the green open circles respectively. The observations one can make from the results are: (i) The magnetization of the 6T cooled sample is larger and remains stable, at 5K, even though the magnetic field has been set to 1 Tesla. (ii) This stability is reduced at about 20K, where the magnetization begins to drop and coincides with that of the 1T cooled sample. Fig. 2.15.(b) shows the corresponding resistivities, the only difference being that these measurements are carried out at zero field as opposed to the magnetization measurements that were done at 1T. They show a concomitant increase for the 1T cooled sample and is much lower for the 6T cooled sample. Similarly, heating the 6T cooled sample, after setting the field to zero, causes an increase in resistivity, starting around

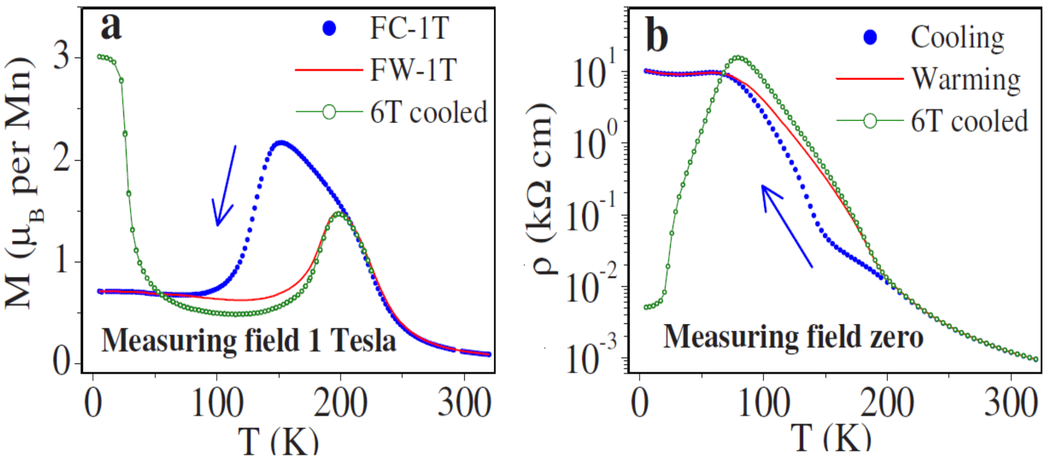

Figure 2.15: Temperature dependence of magnetization (M) in 1 T field and resistivity in zero field of $La_{0.5}Ca_{0.5}MnO_3$ measured under different protocols. (a) M vs T while cooling (FC) from 320 to 5 K and again while warming (FW) from 5K shows the thermal hysteresis accompanying the first order FM to AF transition. After cooling the sample in a 6 T field, the field is reduced isothermally to 1 T at 5 K and M is measured while warming. The large value of M at 5 K reflects a dominant trapped ferromagnetic phase, and its thermal relaxation starts at around 20 K. (b) R vs T also shows hysteresis in the thermal cycling for the zero field cooled sample. After cooling the sample in the 6 T field, the field is reduced isothermally to zero at 5 K and resistivity (R) is measured while warming. The low value of R at 5 K reflects a large fraction of trapped metallic phase, even when the field is brought down to zero. Its thermal relaxation to the AF-CO starts at around 20 K. (From P. Chaddah *et. al.* Phys. Rev. **B 77**, 100402(R) (2008).)

20K and coincides with that of the 1T cooled sample at about ∼ 80K.

The tunability of the coexistent phase fraction in shown in Fig. 2.16 for $Pr_{0.5}Sr_{0.5}MnO_3$, that has intermediate disorder. Fig. 2.16.(a) shows the magnetization and (b) the conductivity of samples cooled in different cooling fields at 5K. The samples were first cooled from 320 K to 5K at the various cooling fields. Clearly, there is a complete range of magnetization that can be attained by cooling in different fields, exhibiting tuanbility of these coexistent states.

While these results have explored the disorder affecting the *thermal* transition we could ask the same question for *field induced* transition at low temperatures. The answer to this is not easy, because of hysteretic tendencies and also possible phase separation in

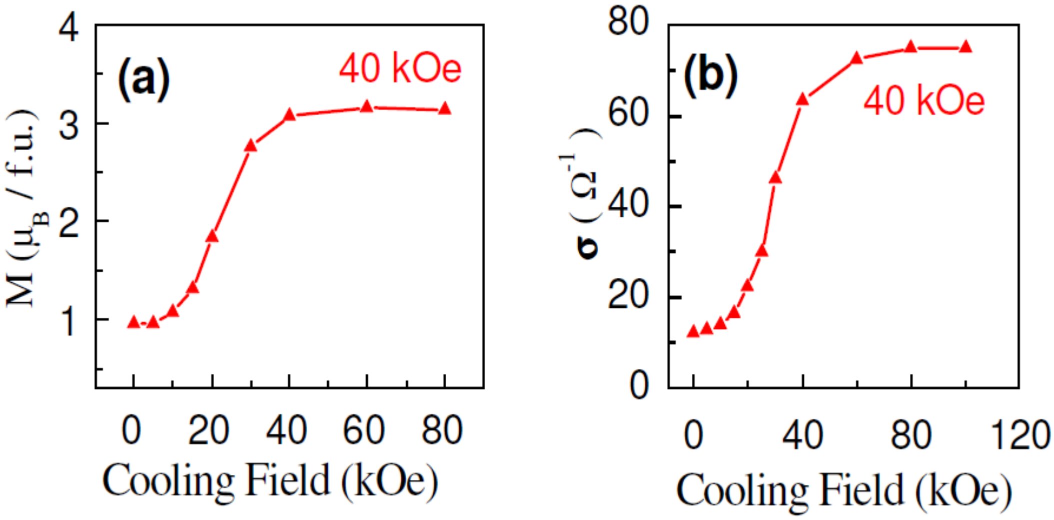

Figure 2.16: $Pr_{0.5}Sr_{0.5}MnO_3$ is cooled each time from 320 K to 5 K in different cooling fields, and then the magnetization is measured after reaching specified measuring field isothermally at 5 K. (a) Different values of magnetization at fixed temperature and field after cooling in different fields for $Pr_{0.5}Sr_{0.5}MnO_3$. In this case the measurement fields are 10 kOe (blue circles) and 40 kOe (red triangles). (b) The multivalued conductivity depending on the cooling field for $Pr_{0.5}Sr_{0.5}MnO_3$. Note that the measurement field is 40 kOe or 4 Tesla. (From P. Chaddah, *et. al.*, arXiv:cond-mat/0703140v1.)

the presence of a magnetic field.

2.4 Puzzles in field melting

Let us conclude this chapter by highlighting the puzzles in the field melting problem.

- *Smallness of the melting fields:* One needs a ‘small’ magnetic field to melt the CO state. In terms of energies, the field melting occurs at a scale much lower than the thermal scale $k_B T_{CO}$. The typical value of T_{CO}, *e.g.* in $Pr_{0.5}Ca_{0.5}MnO_3$, is $\sim$ 250K. The typical magnetic field (average of $h_c^{\pm}$) is about 20 Tesla, equivalent to roughly 20K!

- *Hysteretic response and phase coexistence:* While the thermodynamic critical field can be estimated from energy balance, the upper and lower critical fields that are actually measured define limits of metastability. Material systematics involving non-recovery vs recovery of CO and fate of the field melted state are dependent on the domains of metastability of the competing phases and the sweep rates. This situation is further complicated by possible phase separation tendency in the presence of applied fields.

- *BW dependence of critical melting fields:* One expects $h_c^{\pm}$ to increase with reducing bandwidth, since CO is better stabilised. This indeed happens for lanthanides (Ln) of the form $\mathrm{Ln}_{0.5}\mathrm{Ca}_{0.5}\mathrm{MnO}_3$. However, for members of the $\mathrm{Ln}_{0.5}\mathrm{Sr}_{0.5}\mathrm{MnO}_3$ family, with very similar bandwidth, $h_c^{\pm}$ increases initially with decreasing BW but takes a downturn beyond a critical BW and then drops to zero. This is in sharp contrast to the 'divergence' of $h_c^{\pm}$ seen in the Ca family. Bandwidth apparently is not the 'universal' parameter deciding the melting field. Given that the Sr family has more disorder than the Ca family, disorder seems to play a vital role in this.

- *Disorder effects on kinetics of first order phase transition:* Recent experiments imply that intermediate and even weak disorder can lead to nonequilibrium coexistence at low temperature, and the system is unable to relax to the equilibrium state. Moreover, as evidenced for half doped manganites and LPCMO, coexistence fractions of FM-M and AF-CO are highly dependent on the cooling protocol, making the volume fractions path dependent.

Chapter 3

Model and method of solution

Chapter summary: In this chapter we discuss the manganite model, describe the parameter space, and narrow it down to the regime relevant to the thesis problem. We then describe our computational strategy and the physical quantities tracked in our calculation, and briefly comment on some numerical issues.

3.1 Model

We start by listing out the processes and couplings that enter our model. On the way we will comment on the approximations that we make and the numerical values typical of the relevant energy scales.

3.1.1 Kinetic energy

As we saw in Chapter.1, the two e_g levels on Mn broaden to form the conduction band while the t_{2g} electrons remain localized. The hopping process is described by a 2×2 matrix, connecting the two e_g orbitals on nearest neighbor Mn sites (via the bridging oxygen).

$$H_{\text{kin}} = -\sum_{\mathbf{i}\mathbf{a}\gamma\gamma'\sigma} t^{\mathbf{a}}_{\gamma\gamma'} c^{\dagger}_{\mathbf{i}\gamma\sigma} c_{\mathbf{i}+\mathbf{a}\gamma'\sigma} \tag{3.1}$$

$t^{\mathbf{a}}_{\gamma,\gamma'}$ is the hopping element between d-orbitals (γ and γ') on nearest neighbor Mn sites, in the direction $\mathbf{a}$. The $c_{\mathbf{i}\gamma\sigma}$ and $c^{\dagger}_{\mathbf{i}\gamma\sigma}$ are electron annihilation and creation operators. σ is the spin index and i the site index.

The elements, $t^{\mathbf{a}}_{\gamma,\gamma'}$, are determined by the product of two overlap factors, of Mn d-orbitals with the 2p orbital of the intervening oxygen. The index **a** refers to the spatial orientation of the two Mn orbitals. These overlaps of the Mn d orbital with the oxygen 2p orbital are referred to as $E_{\mathbf{a},\gamma}$ and were worked out by Stater and Koster [87]. The overlap of the $d_{x^2-y^2}$ and the $2p_x$ orbital is given by

$$E_{\mathbf{x},\mathrm{a}}(\ell, m, n) = (\sqrt{3}/2)\ell(\ell^2 - m^2)(pd\sigma), \tag{3.2}$$

and that of the $d_{3z^2-r^2}$ and the $2p_x$ orbital is given by

$$E_{\mathbf{x},\mathrm{b}}(\ell, m, n) = \ell[n^2 - (\ell^2 + m^2)/2](pd\sigma). \tag{3.3}$$

Here, (l, m, n) are the components of a unit vector pointing from the Mn d-orbital towards the oxygen 2p orbital. a, b refer to the two possible e_g d-orbitals and $(pd\sigma)$ is the overlap integral between the $d\sigma$ and $p\sigma$ orbitals. Thus, the various hopping amplitudes can be computed in the following manner.

$$-t^{\mathbf{x}}_{\gamma\gamma'} = E_{\mathbf{x},\gamma}(1, 0, 0) \times E_{\mathbf{x},\gamma'}(-1, 0, 0). \tag{3.4}$$

$$t^{\mathbf{x}}_{\mathrm{aa}} = -\sqrt{3}t^{\mathbf{x}}_{\mathrm{ab}} = -\sqrt{3}t^{\mathbf{x}}_{\mathrm{ba}} = 3t^{\mathbf{x}}_{\mathrm{bb}} = 3t_0/4, \tag{3.5}$$

$$t^{\mathbf{y}}_{\mathrm{aa}} = \sqrt{3}t^{\mathbf{y}}_{\mathrm{ab}} = \sqrt{3}t^{\mathbf{y}}_{\mathrm{ba}} = 3t^{\mathbf{y}}_{\mathrm{bb}} = 3t_0/4, \tag{3.6}$$

and

$$t^{\mathbf{z}}_{\mathrm{bb}} = t_0, t^{\mathbf{z}}_{\mathrm{aa}} = t^{\mathbf{z}}_{\mathrm{ab}} = t^{\mathbf{z}}_{\mathrm{ba}} = 0, \tag{3.7}$$

In our calculations we set $t^{x}_{\mathrm{aa}} = 3t_0/4$ as the scale of kinetic energy t. This is set to unity. All other energies are measured in units of t. The typical estimate is $t \sim 0.2 - 0.3$eV [11] While this sets the rough hopping scale the actual magnitude varies as one changes the ionic radius r_A. There occurs r_A (and hence BW) variation both with changing doping within a family and also between families. These variations were shown in Fig. 1.13.(a) for the Ca and the Sr families.

3.1.2 Interactions

Electron-phonon coupling

As discussed in Chapter.1, we consider only static lattice distortions, *i.e*, work in the strict adiabatic limit. Further, we consider the distortions of the octahedron around each Mn ion to be independent and neglect the effects of 'cooperation' among them.

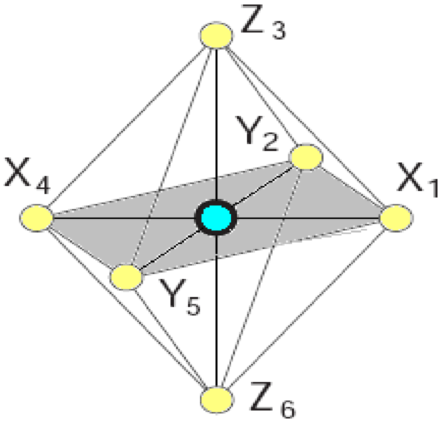

Figure 3.1: MnO_6 octahedron. The labeling of oxygen ions is discussed in the text below. The central ion is Mn.

For an independent octahedron shown in Fig. 3.1, the distortions are given in terms of the oxygen coordinates, as indicated in the figure. Following Kanamori [88], the Jahn-Teller modes are defined in terms of the deviation of the oxygen coordinates around the i^{th} Mn site, as follows:

$$Q_{x\mathbf{i}} = \frac{1}{\sqrt{2}}(X_{1\mathbf{i}} - X_{4\mathbf{i}} - Y_{2\mathbf{i}} + Y_{5\mathbf{i}}), \tag{3.8}$$

and

$$Q_{z\mathbf{i}} = \frac{1}{\sqrt{6}}(2Z_{3\mathbf{i}} - 2Z_{6\mathbf{i}} - X_{1\mathbf{i}} + X_{4\mathbf{i}} - Y_{2\mathbf{i}} + Y_{5\mathbf{i}}), \tag{3.9}$$

These two modes, shown in Chapter.1 Fig. 1.5.(a)-(b), couple to the electrons in the following way:

$$H^{\mathrm{JT}} = g\sum_{\mathbf{i}}(Q_{x\mathbf{i}}\tau^x_{\mathbf{i}} + Q_{z\mathbf{i}}\tau^z_{\mathbf{i}}) \tag{3.10}$$

where,

$$\tau^x_{\mathbf{i}} = \sum_{\sigma}(c^\dagger_{\mathbf{i}a\sigma}c_{\mathbf{i}b\sigma} + c^\dagger_{\mathbf{i}b\sigma}c_{\mathbf{i}a\sigma}), \quad \tau^z_{\mathbf{i}} = \sum_{\sigma}(c^\dagger_{\mathbf{i}a\sigma}c_{\mathbf{i}a\sigma} - c^\dagger_{\mathbf{i}b\sigma}c_{\mathbf{i}b\sigma}). \tag{3.11}$$

are the pseudospin operators. This defines the electron-phonon part of the Hamiltonian at the site i. g is the electron-phonon coupling.

Let us briefly comment on the breathing mode distortion and cooperative nature of phonons that we do not consider in our calculations. The breathing mode couples to the onsite density. The additional term for this would be,

$$H_{br} = \sum_{\mathbf{i}} Q_{1\mathbf{i}}\rho_i + 1/2K_{br}\sum_{\mathbf{i}} Q_{1\mathbf{i}}^2 \tag{3.12}$$

with,

$$Q_{1\mathbf{i}} = 1/\sqrt{3}(X_{1\mathbf{i}} - X_{4\mathbf{i}} + Y_{2\mathbf{i}} - Y_{5\mathbf{i}} + Z_{3\mathbf{i}} - Z_{6\mathbf{i}}) \tag{3.13}$$

The breathing mode distortion prefers to maximize onsite occupancy. As we will see later, the JT phonons *disfavour* double occupancy. Further, the phonons are cooperative, because the oxygen ions are corner shared between adjacent octahedra. The breathing mode and cooperative distortions do affect the quantitative results, but for the issues addressed in this thesis they do not have a qualitative effect. This is confirmed by comparing our results with calculations incorporating these effects [90].

Elastic energy

The elastic cost due to the lattice distortions from the Jahn-Teller modes is given by

$$H^{elas} = \frac{K}{2}\sum_i (Q_{xi}^2 + Q_{zi}^2) \tag{3.14}$$

Here K is the elastic force constant.

Double exchange

Large Hunds rule is incorporated by

$$H^{Hund} = -J_H \sum_i \sigma_i.\mathbf{S}_i \tag{3.15}$$

Here, σ_i is the e_g electron spin at the site i and $\mathbf{S}_i$ is the core t_{2g} spin at the same site. Pushing $J_H \to \infty$ reduces the size of the Hilbert space. To see this we start by adding the kinetic energy term, Eqn. 3.1 to Eqn. 3.15, which is now summed over all sites. This is known as the 'double exchange' Hamiltonian. For $J_H \to \infty$, this problem reduces to 'spinless' e_g electrons moving in the background of the core spins, with the electron spin slaved to the orientation of the local core spin. The double exchange Hamiltonian in this limit is given as:

$$H_{\mathrm{DE}} = -\sum_{\mathbf{i}\mathbf{a}\gamma\gamma'\sigma} t'^{\mathbf{a}}_{\gamma\gamma'} c'^{\dagger}_{\mathbf{i}\gamma\sigma} c'_{\mathbf{i}+\mathbf{a}\gamma'\sigma} - \mu N \tag{3.16}$$

With

$$c'_{\mathbf{i}\gamma} = \cos(\theta_{\mathbf{i}}/2) c_{\mathbf{i}\gamma\uparrow} + \sin(\theta_{\mathbf{i}}/2) e^{-i\phi_{\mathbf{i}}} c_{\mathbf{i}\gamma\downarrow}. \tag{3.17}$$

and

$$t'^{\mathbf{a}}_{\gamma,\gamma'} = (\cos(\theta_{\mathbf{i}}/2)\cos(\theta_{\mathbf{j}}/2) + \sin(\theta_{\mathbf{i}}/2)\sin(\theta_{\mathbf{j}}/2) e^{-i(\phi_{\mathbf{i}}-\phi_{\mathbf{j}})}) t^{\mathbf{a}}_{\gamma,\gamma'}. \tag{3.18}$$

where the classical spins are considered to be unit vectors whose direction are specified by θ_i, and ϕ_i. Further, γ and γ', refer to the d-orbitals on the two sites i and j. All states with e_g electrons at a site with spin opposite to the core spin are projected out.

Antiferromagnetic superexchange

As noted in the first chapter, there is an antiferromagnetic interaction between the core spins. This is incorporated by a Heisenberg term.

$$H_{\mathrm{AFM}} = J \sum_{\langle \mathbf{i},\mathbf{j} \rangle} \mathbf{S}_i \cdot \mathbf{S}_j \tag{3.19}$$

Modeling A-site disorder

As discussed in the introduction, A-site disorder enters the physics of the manganites in two main ways, (i) it randomizes the local electron hopping amplitudes and (ii) it creates a random potential for the e_g electrons on the Mn sites. There has been a careful study of the impact of both these sources of randomness [89]. It reveals that bond disorder is necessary to create the spin glass state at half doping but has negligible effect on the charge order. It is the local scattering centers that have a more pronounced effect on the charge ordered state. So, to minimize the number of parameters in the problem we keep only the random onsite potential. For simplicity the random onsite potential we use is drawn from a binary distribution:

$$H_{dis} = \sum_i \epsilon_i n_i \tag{3.20}$$

where, ϵ_i is picked from:

$$P(\epsilon_i) = \frac{1}{2}(\delta(\epsilon_i - \Delta) + \delta(\epsilon_i + \Delta)) \tag{3.21}$$

The variance of this disorder is $\langle(\epsilon_i - \overline{\epsilon_i})^2\rangle = \Delta^2$. Δ will be a key parameter for us.

Coulomb repulsion

Although the local Coulomb repulsion, *i.e*, the Hubbard interaction, is the largest scale in the problem and inhibits multiple occupancy of the e_g orbital, some of its effects are mimicked by other couplings in the model [90]. Large Hunds coupling rules out the occupancy of e_g states with spin antiparallel to the core spin, so we are left only to consider the occupancy of two e_g states with parallel spin. Here the presence of a large JT coupling penalises multiple occupancy as follows. At large JT coupling, a small polaron (a single electron coupled to onsite distortion) lowers the energy of the system by the polaron binding energy E_{JT}. The unoccupied e_g state is pushed to $+E_{JT}$ while the occupied state is pushed down to $-E_{JT}$. A second e_g electron has to occupy the $+E_{JT}$ state, which is unfavourable compared to occupying another empty site. The value of $2E_{JT}$ is ~ 0.5eV as mentioned in Chapter.1, larger than the kinetic scale (~ 0.2eV). Thus even neglecting Hubbard repulsion, the constraint of 'no double occupancy' can be roughly satisfied.

However, if the system is a ferromagnetic metal the effect of lattice distortions are very weak and the Hubbard interaction becomes relevant. It has been indicated experimentally [17, 18, 19, 20] and shown theoretically [21], that the ground state is a non Fermi liquid, dominated by orbital fluctuations (orbital liquid state). While we do capture an orbital disordered ferromagnetic metal in our calculation, it is a simple 'tight binding' system, without any exotic quantum fluctuations.

Finally, at half doping, starting from a strong electron-phonon coupling regime and using kinetic energy as a perturbation, it is possible to show that a nearest neighbor repulsion scale can emerge, to fourth order in the perturbation. This scale can stabilize the in-plane checkerboard of the charge order in the manganites at half doping.

Overall, to implement a controlled calculation on large systems we neglect the Hubbard effects. As discussed we manage to capture both the CE-CO-I and the FM-M phases, although the correct nature of the metal in the FM state is not captured. There is also the issue of *long range* Coulomb interactions. While we obtain the correct phases ignoring Hubbard and Coulomb effects altogether, the typical sizes of FM-M and CE-CO-I clusters, in a phase coexistent state, would be affected by Coulomb repulsion, particularly in systems with weak disorder. Our cluster coexistent states are controlled by extrinsic disorder, which determine the cluster size.

Magnetic field

The magnetic field is added by coupling it to the core spins. Since we assume $J_H \rightarrow \infty$, the electron spins are slaved to the core spins and need not be coupled directly to the external field. The Zeeman term is

$$H_{mag} = -\sum_i \mathbf{h}.\mathbf{S}_i \tag{3.22}$$

Here, h is the uniform external field, whose direction we choose as the z-axis.

3.1.3 Parameter space

Combining the effects above we write the full model as:

$$\begin{aligned} H &= \sum_{\langle ij \rangle \sigma}^{\alpha\beta} t_{\alpha\beta}^{ij} c_{i\alpha\sigma}^{\dagger} c_{j\beta\sigma} + \sum_i (\epsilon_i - \mu) n_i - J_H \sum_i \mathbf{S}_i.\boldsymbol{\sigma}_i + J \sum_{\langle ij \rangle} \mathbf{S}_i.\mathbf{S}_j \\ & \quad - g \sum_i \mathbf{Q}_i.\boldsymbol{\tau}_i + \frac{K}{2} \sum_i \mathbf{Q}_i^2 - h \sum_i S_{iz} \end{aligned} \tag{3.23}$$

As discussed earlier, the two phonon modes are represented by a two dimensional vector, $\mathbf{Q}$, whose components are Q_x and Q_z. For the numerical calculations we represent $\mathbf{Q}_i$ in polar coordinates, with a length $Q_i = |\mathbf{Q}_i|$ and an angular variable θ_i^Q. The spins $\mathbf{S}_i$ are unit vectors, whose directions are specified by θ_i and ϕ_i.

Given the number of coupling constants, the parameter space to explore is large even if we remain at half doping. To keep the study tractable, we only retain the essential parameters. Firstly we measure all couplings in units of t. As discussed above, we also take the $J_H \rightarrow \infty$ limit. The elastic force constant K is taken to be unity, which amounts to measuring length in units of $\sqrt{K}a_0$, a_0 being the lattice parameter. This scales g by $1/\sqrt{K}$. We define this scaled electron-phonon coupling, $g/\sqrt{K}$, as λ. This leaves λ, J and the disorder variance Δ as the electronic parameters. Magnetic field (h) and temperature (T) will be two control variables.

The parameter space comprises of λ, J and Δ. For notational simplicity we will refer to the dimensionless parameters λ/t, J/t, Δ/t, h/t and T/t as λ, J, Δ, h and T respectively. Further, to reduce the computational cost of the technique employed, we study this model on 2 dimensional lattices. We vary the chemical potential, μ, in our calculations to keep the density $n = 0.50$. Let us briefly discuss the physics contained in this Hamiltonian:

(i) Broad trends: There are roughly two opposing tendencies in the model. The kinetic energy prefers to delocalize electrons, whereas (strong) electron-phonon coupling would like to localize them. Further, delocalization is favored by a ferromagnetic background, while electron localization suppresses the FM exchange and promotes an AF state via the superexchange. If λ and J are small, we should have a ferromagnetic metallic (FM-M) ground state. If both are large we should have a charge ordered polaronic insulator with AF character.

(ii) Strong coupling limit: If $t = 0$, the electrons will be site localised and the spins in a $\{\pi, \pi\}$ antiferromagnetic configuration. The electrons will be *randomly* distributed. Finite t creates an effective short range repulsion between the polarons (from an attempt to gain kinetic energy) and the charges 'order' into a checkerboard. With growing t the AF background can give way to ferromagnetism, still keeping the electrons localised. This is the FM-CO state. This CO state cannot be melted by a magnetic field.

(iii) Phase competition: When λ and t are comparable the FM-CO state is not favored. In this case, for a range of J, the system creates a compromise between the FM and the (π, π) AF state, leading to the 'CE' state. The charge order in this state is aided by the CE order, and disrupting the CE background by a magnetic field can affect the charge order.

(iv) Some issues regarding dimensionality: Let us comment on some general issues related to our 2D calculation.

- Long range magnetic order at finite temperature: given that the system without a magnetic field has $O(3)$ rotational symmetry for the classical spins, the Mermin-Wagner theorem [92] would prevent any long range magnetic order. However, since we would not consider infinite systems, the long wavelength modes that disrupt the long range order are not excited. Moreover d=2 being the lower critical dimension for long range order, one hopes that the suppression of "order" with increasing system size is slower (logarithmic) as opposed to 1D. Thus on small finite systems one can obtain ordered states at finite temperatures, which are progressively destroyed with increasing cluster size. For the system sizes used, in Chapter.4, Sec.4.7, we show explicitly that although the magnetic scales fall with increasing system size, up to 40^2, the fall is slow and T_C remains finite enabling us to estimate the 3D ferromagnetic ordering temperature. Details of conversion of the 2D finite cluster T_C to 3D is presented in Chapter.4.

- Existence of a 'metallic' state: even weak disorder would create an Anderson localized phase in 2D, while we have discussed metallic states in the presence of quenched disorder. However, the finiteness of the systems used suppress the coherent back scattering of the electrons and one can end up with metallic domains of order system size for small clusters, akin to 3D.

- Long range CO in the presence of disorder: with increasing system size the structure factors of the relevant order parameters get suppressed. From random field Ising model (RFIM) studies it is known that d=2 is the critical dimension for ordering of the spins [93]. Systems such as defects in vortex lattices and impurities in charge density wave systems are thought to be represented by the RFIM [94]. Assuming such a mapping of the present checkerboard charge order, we see that although there will be no long range order, domains of finite size might exist in 2D. In Chapter.5 we show that for up to $\sim 40^2$ system sizes, the CO melting scales fall but slowly allowing us to extract an estimate of T_{CO} for the 3D problem.

3.2 Monte Carlo strategy

The adiabatic limit for the phonons and classical treatment of the spins allows these to be treated as a 'fixed' background when solving the electron problem. The background is determined via an annealing process. There are no analytic tools for a solution of the problem at strong coupling and with disorder present. One can use exact diagonalization (ED) of the effective one body problem in the classical spin-phonon background, generating the spin and phonon variables via a variant [95] of standard Monte Carlo (MC).

The annealing of these classical variables is done by choosing a random spin-phonon background to start with, at high temperature, and then cooling the system to progressively lower temperature. We use $\sim$ 4000 sweeps at each temperature. Each sweep consists of sequentially visiting every site of the lattice, locally changing the spin and

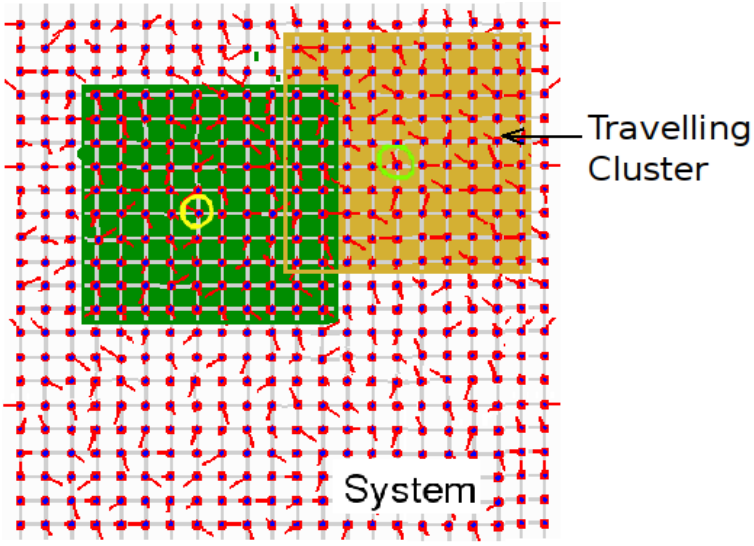

Figure 3.2: Schematic showing the travelling cluster approximation. The system shown consists of random spins. The green and the orange squares are two representative clusters built around the site being updated (site circled within the green and the orange squares.) These moving clusters are employed to anneal the disordered spin background.

phonon variables, and diagonalizing the system to accept or reject the move based on the Metropolis strategy.

In our calculations, we assume a 2-dimensional square lattice in real space with periodic boundary conditions. For a lattice with $N = L^2$ sites, the resulting Hamiltonian matrix has a dimension of $2L^2$, where the '2' comes from the two e_g states at each site. Conventional ED-MC allows access of only small cluster of sites, up to $\sim 8^2$ sites. The main cost comes from the fact that one need to diagonalize the full Hamiltonian at each step of the MC, for determining whether to accept or reject spin/phonon updates. Diagonalization is an $\mathcal{O}(N^3)$ process, and one needs to repeat this N times for a system sweep, so the cost per sweep for this class of problems is $\mathcal{O}(N^4)$, in contrast to the $\mathcal{O}(\mathcal{N})$ cost of a short range classical model.

However, in the presence of even weak (effective) disorder, the the effect of a local MC update does not propagate to large distances. To estimate the energy *change* associated with the move one need not diagonalize the full system. Instead one can consider a smaller region, around the site to be updated, and just diagonalize this small Hamiltonian. If this has a dimension N_C, then the cost of the MC is NN_C^3. This leads to a huge gain, allowing one to go up to 40^2 system sizes. Only while calculating the system properties such as density of states (DOS), *etc.*, does one diagonalize the full system. A typical schematic is shown in Fig. 3.2. This technique is extensively benchmarked in reference [95]. The distinct advantage of accessing large sizes, allowed us to study large scale phase separation tendencies that arises in the problem at hand.

3.3 Field-temperature protocols

As we saw in Chapter.2, typical experiments on the field melting of the CE-CO-I state were done by cooling the systems in zero field and then sweeping up and down in magnetic field (h). In our MC, we too follow the same protocol, *i.e.*, we cool the system in zero field to a desired low temperature and then apply a magnetic field which we first increase till we reach a fixed high field and then sweep it back to zero. The field is swept up and down at a same constant rate. We typically change the magnetic field in in steps of 0.01 measured relative to the hopping scale t. Further, at each step of the field we allow 4000 MC steps or system sweeps.

3.4 Physical quantities

We conclude this chapter with a discussion of the various indicators of order and transport that we will compute and track in our calculation across changing temperature and magnetic fields. These allow us to determine the various phase diagrams and responses.

1. *Structure factors:* We compute the 'one point' distribution of lattice distortions, $P(Q) = \sum_i \delta(Q - Q_i)$, where $Q_i = |\mathbf{Q}_i|$, spatial $Q - Q$ correlations, $D_Q(\mathbf{q}) = \sum_{ij} \langle \mathbf{Q}_i \mathbf{Q}_j \rangle e^{i\mathbf{q}\cdot(\mathbf{r}_i - \mathbf{r}_j)}$, and spin-spin correlations, $S(\mathbf{q}) = \sum_{ij} \langle \mathbf{S}_i . \mathbf{S}_j \rangle e^{i\mathbf{q}\cdot(\mathbf{r}_i - \mathbf{r}_j)}$. Angular brackets represent a thermal average.

2. *Spatial analysis:* We also compute the volume fraction of the charge ordered region in the lattice from direct spatial snapshots of the charge distribution. To measure the volume fraction, we tag a site with a particular color if the site has $n > 0.5$ and is surrounded by the four nearest neighbor sites with $n < 0.5$ and vice versa (i.e. a site with local anti-ferro-charge correlation is marked with a particular color).

Similarly, if the difference between the charge density at a site with its nearest neighbours is less than a threshold, that site is tagged by a different color, *i.e.*, the charge uniform regions are marked by this color. For intermediate cases, we use an interpolative colour scheme. A measure of the volume fraction is necessary for studying inhomogeneous melting because the momentum space structure factors are not a good measure of the local CO in the system. Further, the spatial snapshots also directly provide visual information on the melting process.

3. *Transport:* While the indicators above measure the correlations and spatial evolution, the metallic or insulating character is tracked via (low frequency) conductivity [96], σ_{dc}, and the density of states (DOS), $N(\omega) = \langle \frac{1}{N} \sum_n \delta(\omega - \epsilon_n) \rangle$, where ϵ_n are the electronic eigenvalues in some MC background and the angular brackets indicate thermal average.

We track all the above quantities as a function of temperature and applied magnetic fields for studying the CO melting phenomenon. In the next two chapters we provide our results on the clean system and the disordered systems respectively.

Chapter 4

Melting in 'clean' systems

Chapter summary: In this chapter we present our results on the field melting of the non disordered CE-CO-I state. We begin with a survey of earlier theoretical work. We then present the various states at half doping obtained from our calculation and focus on the parameter window where the CE-CO-I is the ground state. We describe the response of this state to magnetic field sweep at low temperature, clarify the spatial character of the finite field state, and map out the field-temperature phase diagram. We suggest a Landau framework for organising the field response. We conclude with a comparison of our results with experiments and comment on some computational issues.

4.1 Earlier work

Let us start with a brief discussion of earlier attempts to model the field melting of the CE-CO-I state. These calculations are either based on mean field or variational approaches.

To our knowledge, the earliest study [6] of field melting of CO involved a one band double exchange model with on-site and nearest neighbour Hubbard interaction in addition antiferromagnetic superexchange. The model employed was:

$$\begin{aligned} H &= -t \sum_{<i,j>,\sigma} c^{\dagger}_{i,\sigma} c_{j,\sigma} + U_0 \sum_{i} n_{i\uparrow} n_{i\downarrow} + U_1 \sum_{<i,j>,\sigma,\nu} n_{i,\sigma} n_{j,\nu} \\ & -J_{ex} \sum_{<i,j>} S_i S_j - 2J_H \sum_{i} S_i . s_j - \mu \sum_{i,\sigma} n_{i,\sigma} \end{aligned}$$

A (Hartree) mean field study of this was carried out for different configurations of the classical spins and the energy of these states were compared for different values of external

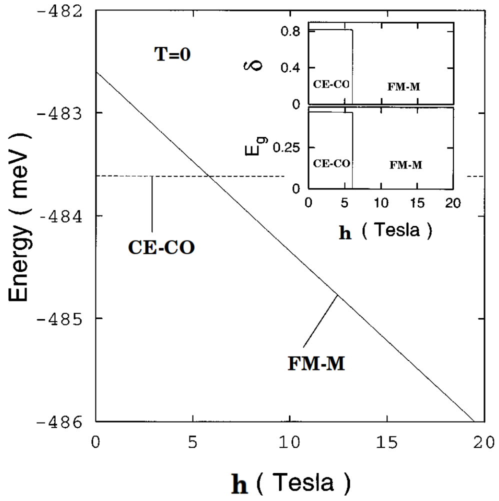

Figure 4.1: Variation of the energies of the CE and the ferromagnetic phases indicating the ’melting’ of the charge-ordered state into a charge-nonordered ferromagnetic state induced by an applied magnetic field h. The variation of the charge-order parameter or disproportionation (δ) and the energy gap (E_g) with h are shown in the inset. (From S. K. Mishra, *et al.*, Phys. Rev. **B 56**, 2316 (1997).)

magnetic field (h), Fig. 4.1. Based on this it was concluded that for sufficiently large h the zero field CE-CO-I state melts into a FM-M through a first order transition at $T = 0$. The result highlighted the existence of a CO state dependent on antiferromagnetism, and its destabilisation on disrupting the AF order. However, the finite T transition was from a CE-CO-I to an FM-CO, with a much reduced charge disproportionation ($\delta \sim 0.2$), not to a metallic phase.

A more appropriate model [5] for the manganites, taking into account the coupling of electrons to Jahn-Teller phonons has also been explored. A variety of magnetically ordered states, in a homogeneous or charge ordered background, were examined in the presence of a field. It was shown that a CE-CO state could be melted by applying a magnetic field. This effect was tracked for varying BW of the manganite model, and the authors observed an increase in the melting field with decreasing BW, a key experimental trend shown in Fig 4.2. The panels show the $h - T$ phase diagram at successively increasing BW. The lines demarcate the phase boundaries. At low T, with increasing BW it becomes easier to destabilise the CE phase, with the CE-phase not being present at all in the rightmost panel. However, such calculations cannot capture non-equilibrium aspects such as the

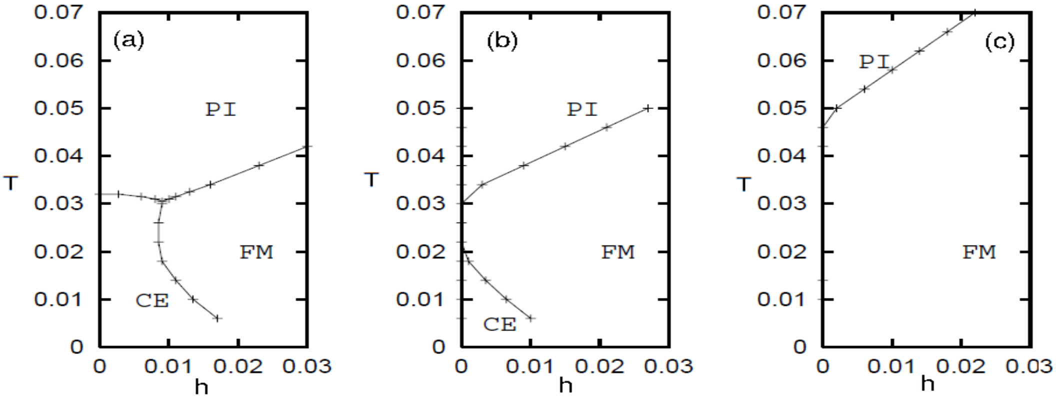

Figure 4.2: Phase diagrams as function of temperature and magnetic field, for three choices of bandwidth, increasing left to right. (From S. Fratini, *et. al.*, Eur. Phys. J. **B 22**, 157 (2001).)

hysteretic response or the real space nature of the field melted state.

Another recent effort is the study of a two orbital model, much like what we study here, with a large family of variational states [7]. This established that the smallness of the (thermodynamic) melting fields is due to the closeness in energy of the CE-CO-I and FM-M phases. It also suggested that the field melted state could be inhomogeneous, since at finite h a CE-CO state with "defects" seems preferable to the homogeneous CE-CO-I or FM-M.

The attempts above have added valuable insight to the field melting problem but have left the following issues unexplored:

- The spatial character of the high field state.
- Hysteresis and metastability in the field response.
- The impact of disorder on the melting process.
- Interplay of disorder and strong coupling in melting.

By employing a real space Monte Carlo technique on large lattices, we settle most of these issues in the present thesis.

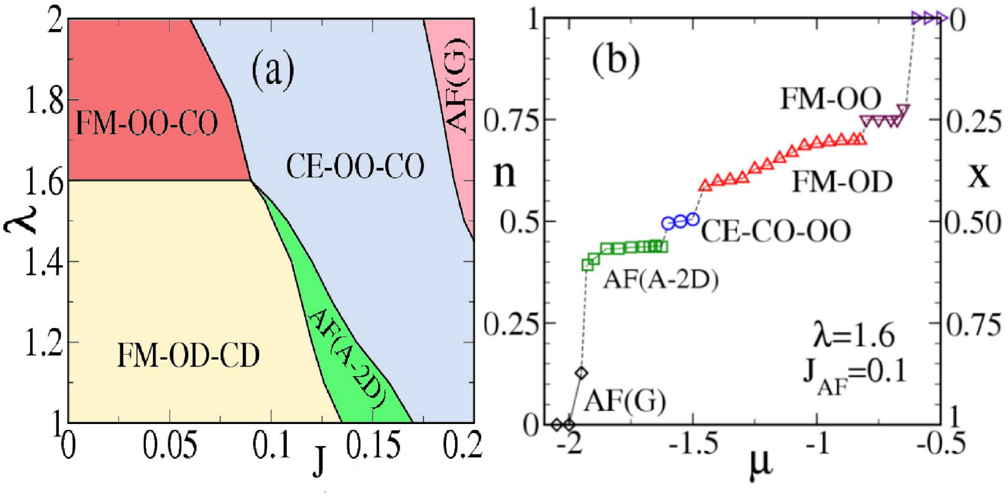

Figure 4.3: (a) The ground state at $x = 0.50$ for varying J and λ, in the absence of disorder. (From D. Akahoshi, *et. al.* Phys. Rev. Lett. **90**, 177203 (2003).)(b) The doping ($n = 1 - x$) dependence of the ground state for varying chemical potential μ and typical electronic couplings, $\lambda = 1.6$ and $J = 0.1$, near the FM-OD-CD & CE-CO-OO phase boundary. The phases in the vicinity of $x = 0.5$ are expected to show up in a cluster pattern on introducing disorder at $x = 0.5$.

4.2 Results at zero field

In this chapter we set $\Delta = 0$, *i.e.*, consider only clean systems. As discussed in Chapter.2, these results are of relevance for either specially prepared ‘ordered’ systems or ‘alloy’ structures with low cation mismatch, as in the Ca manganites $Ln_{0.5}Ca_{0.5}MnO_3$. These calculations allow us to obtain the phases for different combinations of JT coupling (λ) and AF coupling (J) at low temperature, and identify the parameter region where the CE-CO-I is the ground state. Based on this we choose parameter sets $\{\lambda,\ J\}$ that are appropriate to the manganites we wish to understand. We also identify the competing phases in the neighbourhood of the CE-CO-I state at half doping.

The nature of the competing states suggest external agencies that can be used to destabilise the CE-CO state. For example, the proximity of a FM-M state implies that a small magnetic field can convert the CE-CO-I to a FM-M. This suggests how we can tune parameters to control the ‘melting’ field. In addition, given phase separation tendencies in manganite models, it is necessary to explore *off half doping* phases as well. In the next subsection we discuss these issues in detail.

4.2.1 $\lambda - J$ phase diagram

Figure 4.3.(a) shows the various states that arise in the half doped system [97]. At low λ and low J double exchange is the dominant interaction and kinetic energy optimisation leads to a homogeneous ferromagnetic state without any orbital or charge order (FM-OD-CD). This phase has a finite density of states at the Fermi level ϵ_F and is metallic.

As J is increased, keeping the JT coupling small, a magnetic state emerges with peaks in the structure factor $S(\mathbf{q})$ at $\mathbf{q} = \{0, \pi\}$ or $\{\pi, 0\}$. This is the two dimensional analog of the 'A type' AF and we call it the A-2D phase. At larger J an orbital ordered but uniform density CE phase occurs, with simultaneous peaks in $S(\mathbf{q})$ at $\mathbf{q} = \{0, \pi\}, \{\pi, 0\}$, and $\{\pi/2, \pi/2\}$. At even larger J the dominant correlations are 'G type' with a peak at $\mathbf{q} = \{\pi, \pi\}$. By contrast, increasing λ at weak J keeps the system ferromagnetic but leads to charge and orbital order (FM-CO-OO) for $\lambda \gtrsim 1.6$.

In this phase diagram we now restrict ourselves to the region where the CE-CO-I state occurs. Such a state shows up when both λ and J are moderately large as seen from Fig.4.3. Keeping in mind the experimental melting fields we choose to remain near the FM-M boundary in the CE-CO-I phase. This should yield 'small' melting fields, as a small Zeeman energy can change the free energy balance in favor of the FM-M state. The TCA based phase diagram is broadly consistent with previous variational results [98, 99, 100, 101] and with ED-MC on small systems [102].

Phase separation (PS) tendencies in the clean system, and the resulting coexistence of phases [103, 104] *of different densities* require us to explore the phases off half doping as well. The various phases for the density window $n = [0, 1]$ and the phase separation windows are shown in Fig.1.(b) for $J = 0.10$ and $\lambda = 1.6$. For these couplings the clean system is a CE-CO-I phase at $x = 0.5$, a FM-M for $x \lesssim 0.4$, and an A-2D type AF for $x \gtrsim 0.55$. While the above results are on the ground state, a lot of information, such as the thermal transition and the λ dependence of the CE-CO-I state is discussed in the context of the $\lambda - T$ phase diagram. These will provide systematics that can be compared with the material trends shown in Fig. 2.4 in Chapter.2.

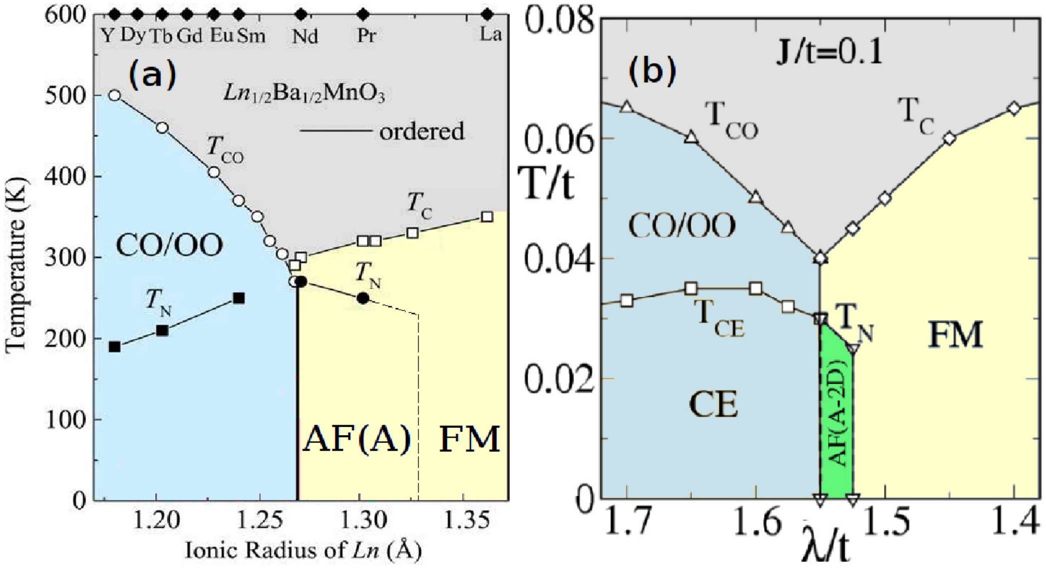

Figure 4.4: (a) Experimental ‘bicritical’ phase diagram in the $x = 0.5$ manganites obtained for ordered structure. (From D. Akahoshi, *et. al.* Phys. Rev. Lett. **90**, 177203 (2003).) (b) Our results: phase diagrams at $x = 0.5$ for $\Delta = 0$. The long range CE-CO-OO for $\lambda > 1.55$ and the FM-M below 1.52 are separated by a A-2D antiferromagnetic phase.

4.2.2 $\lambda - T$ phase diagram

Fig. 4.4.(a) shows the Ln radius-vs-T phase diagram for ‘ordered’ half doped manganites. The decrease of Ln radius is equivalent to decrease in the mean cation radius r_A and, for us, an increase in λ/t. In this spirit, we also show in Fig. 4.4.(b) our results on the clean system.

At $T = 0$ as λ is increased there is a transition from a FM-M to the A-2D phase at $\lambda \sim 1.52$, and then a transition to a CE-CO-OO phase at $\lambda \gtrsim 1.55$. On the FM-M side, $\lambda \leq 1.52$, there is only a single thermal transition at T_C as one cools the system. At large λ, however, cooling first leads to a CO-OO phase, at T_{CO}, without magnetic order, followed by strong features in $S_{\mathbf{q}}$ at $\mathbf{q} = \{0, \pi\}$ and $\{0, \pi\}$, showing up at T_{SR}, indicative of stripelike correlations. Finally, at a lower T the system makes a transition to CE order. Note, that our 2D magnetic ’T_C’ correspond to correlation length $\xi(T_C) \approx L$. There is no genuine T_C for $L \to \infty$ in 2D. However we can still use a crude scaling between the infinite 3D T_C and one obtained in our finite 2D clusters. If we set $t = 0.2$eV, and use a factor of 3/2 to convert transition scales between 2D and 3D our T_C at bicriticality would

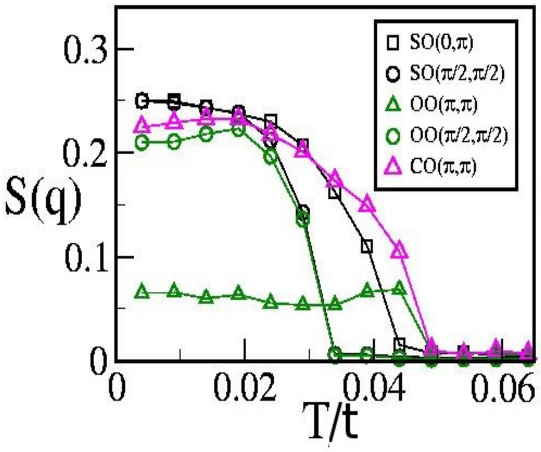

Figure 4.5: Structure factors at $J = 0.1$ and $\lambda/t = 1.6$. The T dependence of the major peaks in the structure factor for spin order (SO), orbital order (OO) and charge order (CO) in the clean limit. Note the clear separation of scales between T_{CO} and T_{CE}.

be $\sim$ 150K. This '3/2' factor arises from the ratio of coordination numbers in 3D and 2D.

The increase of T_{CO} with increasing λ implies strengthening of the CO state. Notice that T_{CE} falls with increasing λ. This signals a gradual 'decoupling' of the spin and the charge degrees of freedom with increasing λ, the CO becomes progressively independent of the antiferromagnetic order. The same is also seen in Fig. 4.5, where we plot the evolution of features in the the magnetic structure factor $S(\mathbf{q})$ with T. There is a clear separation between the temperature at which the CO sets in and that at which the CE order is stabilized. The $\mathbf{q} = \{\pi, 0\}$, $\{0, \pi\}$ features indicate stripe like magnetic correlations with CO but no long range CE order.

We end this section with a look, in Fig. 4.6, at the spatial pattern that we obtain by mapping out the nearest neighbour magnetic correlation (left), the charge density profile (center), and the magnetic structure factor (right) for the CE-CO-I state at $J = 0.10$ and $\lambda = 1.6$. The pattern of the magnetic bonds show ferromagnetic (red) zigzag chains coupled antiferromagnetically (green) between them. These correlate with the $\mathbf{q} = \{0, \pi\}$, $\{\pi, 0\}$ and $\{\pi/2, \pi/2\}$ features in the magnetic structure factor.

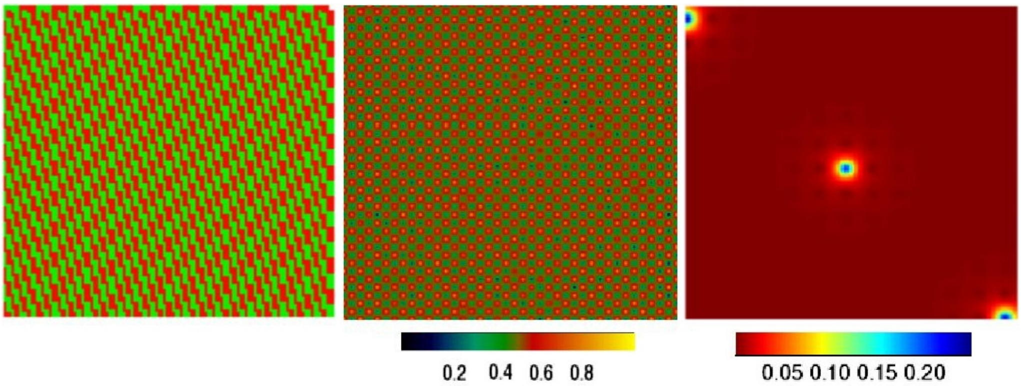

Figure 4.6: MC snapshots and magnetic structure factor at low temperature, $T = 0.01$, size 40×40. These are for $\lambda = 1.6$ and $J = 0.1$. Left panel shows the nearest neighbour magnetic correlation $\mathbf{S}_i.\mathbf{S}_{i+\delta}$, where $\delta = x$ or y. The red bonds are ferromagnetic and the green ones are antiferromagnetic. Middle panel shows the corresponding charge density $\langle n_i \rangle$. The right panel shows the MC averaged $S_{mag}(\mathbf{q})$. In the right panel $\mathbf{q} = \{0, 0\}$ at the bottom left corner, $\mathbf{q} = \{\pi, 0\}$ at the bottom right corner, *etc.*

4.3 Finite field response

The field-temperature protocol we use involves zero field cooling and then sweeping up and down in magnetic field. In Fig.4.3.(a), we have a large parameter space where the system presents a CE-CO-I ground state. We have done MC calculations sampling the entire CE-CO-I window in the phase diagram, and notice very different field response in different parts of the window. We attempt an organisation of this variety below, postponing the detailed field response to the next section. Fig 4.7.(a) is the same as Fig.4.3 with various lines demarcating regions that have distinct response to low T field sweep.

These distinct regimes are determined by simultaneously tracking the $\mathbf{q} = (0, 0)$ component of the magnetic structure factor $S(\mathbf{q})$, the charge order volume fraction V_{CO}, and the $\mathbf{q} = (\pi, \pi)$ component of the charge structure factor $D_Q(\mathbf{q})$ as a function of h. The detailed indicators allowing this classification are discussed in the next section, here we just present the classification and motivate it in terms of competing phases and proximity to phase boundaries.

(i) The red line shows the boundary above which the CO state does not melt however large the magnetic field, although the magnetic state is fully polarised. All melting phenomena are confined to CE-CO-I regions below this boundary. Below this line there

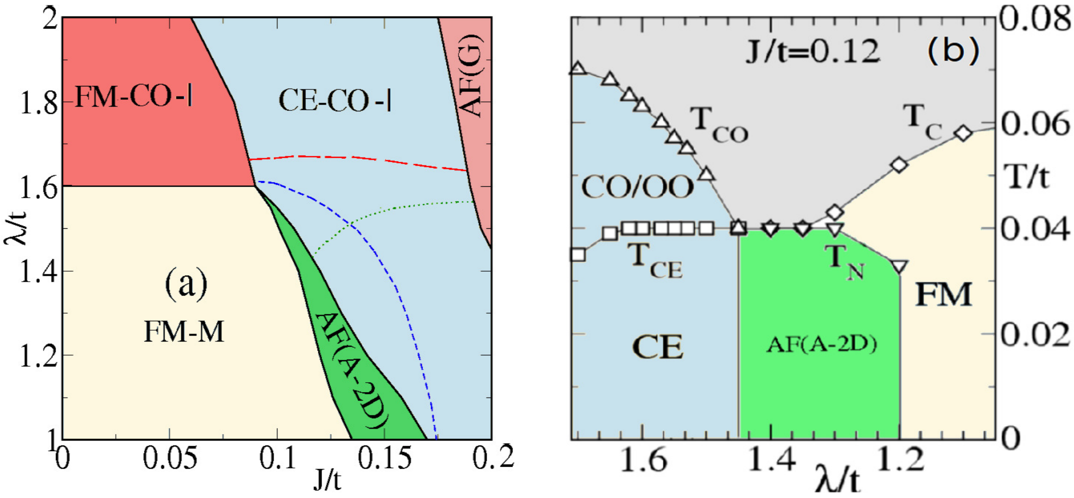

Figure 4.7: (a) The $\lambda - J$ phase diagram at $T = 0.01$. The various phases are indicated in colors separated by solid lines. The dashed/dotted lines, demarcate various parameter regimes in the CE-CO-I phase terms of their response to the applied fields. For large λ, above the big-dashed line, the CO state does not melt on applying a magnetic field. Below this line, the CE-CO-I state melts in response to an applied magnetic field. This region can be classified into one that recovers the CO state in a low T field cycle (between the big-dashed line and finely-dashed line) and another that does not recover CO (below the finely-dashed line). Below the dotted line the field melting yields a homogeneous FM-M and above it, the melting forms an inhomogeneous state. (b) The clean $\lambda - T$ phase diagram at $J = 0.12$. Note, in (b) λ increases from right to left. Since, these are thermal evolution with λ at the fixed J, the AF (A-2D) region separating the FM-M and CE-CO-I phases at low T, is smaller for the $J = 0.1$ (Fig. 4.4.(b)) cross section as compared to that at $J = 0.12$.

are CE-CO-I regions that either share first order boundary with FM-CO for $\lambda \sim 1.6-1.65$ or with the A-2D phase at lower λ. Melting of the CO can happen at low λ by a transition to the FM-M phase. It is not expected that the region $\lambda \sim 1.6 - 1.65$ which shares boundary with FM-CO, will lose CO with applied field. However, we shall later see that at intermediate fields the system phase separates between *off half-filling* charge ordered and non ordered regions. At large fields however, the system recovers a weak CO phase.

(ii) The green (dotted) line separates regions with different kinds of hysteretic response. Between the green and the red lines the CO state melts with increasing h and recovers when h is swept back. Between the blue line and the AF(A-2D) boundary the melted CO state does not recover when the magnetic field is swept back to zero. This non-recovery suggests the existence of a metastable FM-M minimum, close by in energy to the CE-CO-I absolute minimum even when $h = 0$. Thus, when the field is swept back to zero the system can have a FM-M volume fraction in the final state. Deeper into the CE-region, beyond the blue line, the FM-M minimum is no longer metastable at $h = 0$ and the CE-CO-I is recovered on field reduction.

(iii) Finally, the blue line is the boundary between inhomogeneous (or partial) melting and homogeneous melting. The system melts homogeneously below this line and inhomogeneously above it. The inhomogeneous melting at fields beyond h_c^+ cannot be explained in terms of the zero field half doping phases. It is related to phase separation into *off* half doping phases at intermediate magnetic fields.

A lot of information can be obtained by exploring the λ dependence at fixed J. If we are in a parameter regime where the FM-M and CE-CO-I phases are very close, $\lambda \sim 1.6$ and $J \sim 0.10$, we can drive a CE-CO-I to FM-M transition by applying a small magnetic field. In the present work we restrict ourselves to two choices, $J = 0.1$ and $J = 0.12$. While $J = 0.10$ allows closer agreement with experimental temperature and field scales, it does not allow much room to explore the λ dependence. The available λ window ($\Delta\lambda$) is ~ 0.1. At the lower end one hits the AF-M phase and at the upper end (above the dashed red line) the CO-state cannot be destabilised using a magnetic field. For exploring the BW dependence in more detail we choose $J = 0.12$ allowing a window $\Delta\lambda \approx 0.2$. The corresponding $\lambda - T$ phase diagram is shown in Fig. 4.7.(b). While it is qualitatively similar to Fig. 4.3.(b), the A-2D phase is wider, implying that the thermodynamic melting fields would be larger than at $J = 0.10$. We now look at the indicators that helped us classify the field response.

4.3.1 Low temperature field sweep

The field response are shown for the different regions in Fig. 4.8(a)-(d). We show the CO volume fraction, V_{CO}, and the $\mathbf{q} = (0, 0)$ magnetic structure factor in the top panels, and the corresponding resistivity $\rho(h, T)$ in the bottom panels.

Intermediate and large λ regime:

Let us consider two CO states, (i) at $\lambda = 1.55$ where the CO ‘melts’ in response to increasing h, and (ii) $\lambda = 1.70$, where it does not. These are the last two columns

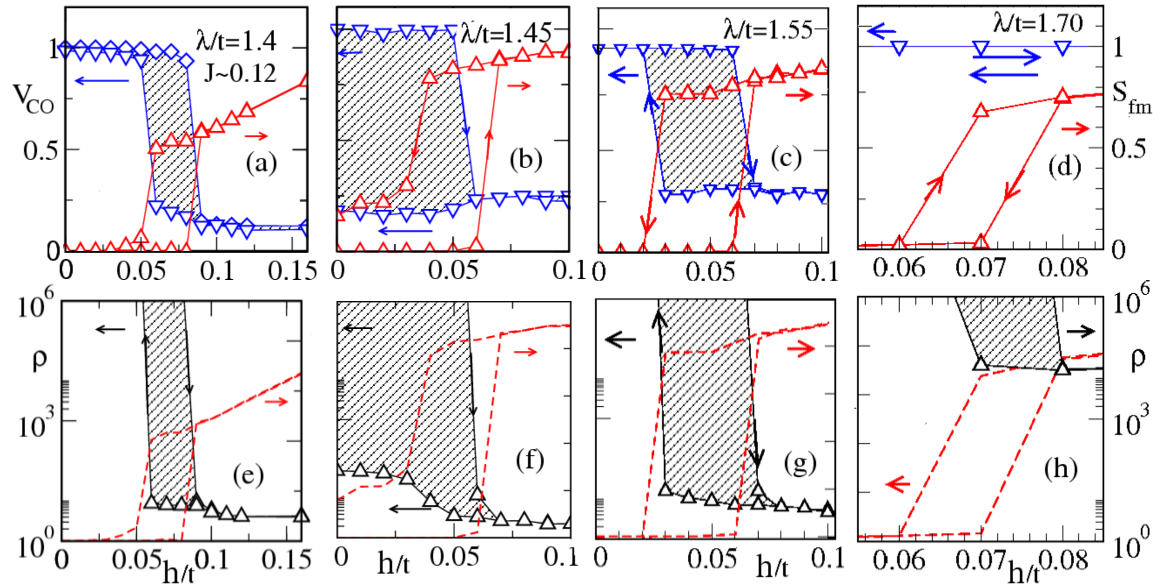

Figure 4.8: Distinct response to field cycling for different λ. Top panel shows V_{CO} and $S_q(0,0)$ and bottom panel shows the corresponding resistivity as a function of the applied magnetic field. The λ/t values for the systems are indicated and $J = 0.12$. All results are obtained at T=0.02. In the top panel, with increasing λ, the forward switching fields h_C^+ increase and for $\lambda = 1.7$, the CO does not melt. The corresponding resistivities show a concurrent switching with an abrupt change in V_{CO}. Hysteresis is seen in all four cases, except that hysteresis for $\lambda = 1.7$ occurs only in the magnetic sector, while it occurs for all, V_{CO}, S_{fm} and ρ, in the first three cases. With increasing λ, the melted state has successively large amounts of residual CO, which increases to unity for $\lambda = 1.7$. Further, at intermediate $\lambda \sim 1.45$, the system doenot recover the CO state when the magnetic field is cycled back to zero, signalling that the FM-M is is metastable even at zero field.

in Fig. 4.8. These λ lie on opposite sides of $\lambda \sim 1.65$ in the $\lambda - J$ phase diagram, Fig. 4.7.(a). Above $\lambda \sim 1.65$, the FM-CO state does not melt with any magnetic field, *i.e* the CO is not dependent on CE magnetic order for its survival. For lower λ the CO melts. In both these cases the applied field transforms the CE order to FM. For $\lambda = 1.55$ there is a sharp reduction in the CO volume fraction V_{CO}, while for $\lambda = 1.70$ the V_{CO} does not change (there is, however, a decrease in the charge disproportionation). Fig. 4.8.(g)-(h) show $\rho(h)$ at low T. For $\lambda = 1.55$ there is a large drop in resistivity associated with the magnetic transition (shown in dashed red lines). The V_{CO}, although dropping sharply has a finite value. This state with a finite V_{CO} and a 'low' resistivity is likely to be a percolative metal.

However, this by it self does not guarantee that the true ground state is phase

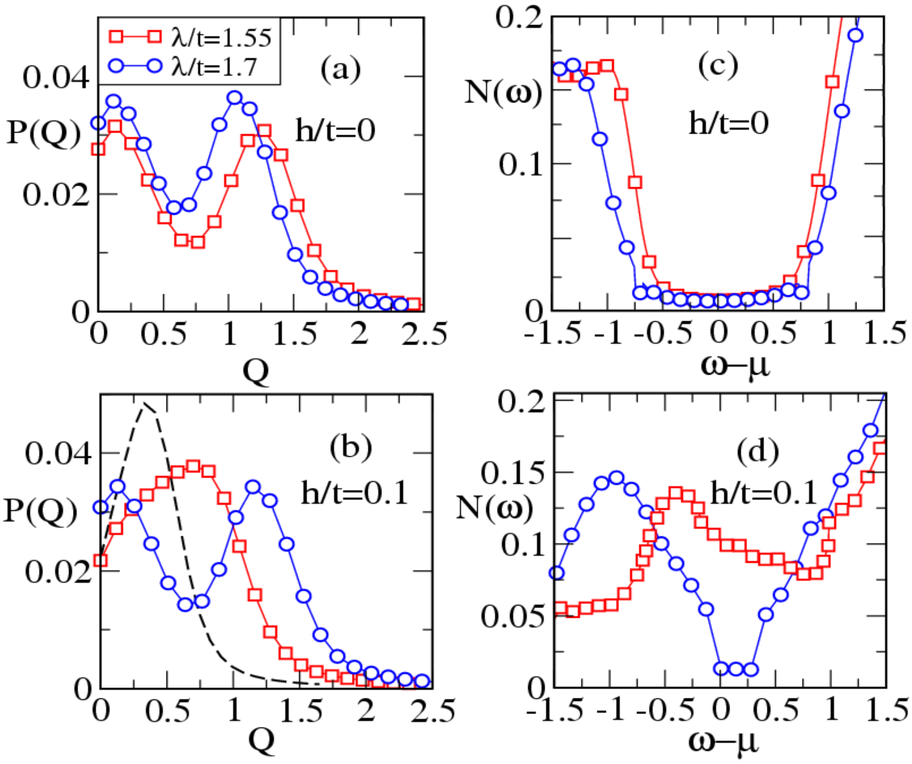

Figure 4.9: Comparison of field response of two systems on either side of the critical $\lambda(\sim 1.65)$, beyond which the CO state does not melt with magnetic field. (a)-(b), $P(Q)$ vs Q at $h/t = 0$ and $h/t = 0.1$ respectively. (c)-(d), $N(\omega)$ vs $\omega - \mu$ at $h/t = 0$ and $h/t = 0.1$ respectively. In (b), the dashed line is the $P(Q)$ for $\lambda = 1.0$, where the ground state is a uniform metal.

separated. This is because low T field sweeps in the presence of multiple free energy minima can lead to trapping into a non equilibrium state. Here we tentatively treat the result as an indication of an inhomogeneous *equilibrium* state. We will separate out cases of equilibrium coexistence from nonequilibrium trapping in later sections. Contrast this with the system at $\lambda = 1.70$ where the resistivity continues to be very large and the V_{CO} stays unity even at large h.

For these two cases we now look at the distribution, $P(Q)$, of lattice distortions, and the DOS, $N(\omega)$, to gain some insight into the melted state. Fig. 4.9.(a)-(b) show $P(Q)$ at $h = 0$ and 0.10 respectively. For $\lambda = 1.55$, at $h = 0$ the $P(Q)$ is bimodal. The two peaks in $P(Q)$ imply a possible spatial modulation of the lattice distortion and a checkerboard CO ground state. This state melts into a metal at $h \sim 0.07$, see Fig. 4.8.(g).

The $P(Q)$ at $h = 0.1$, Fig. 4.9.(b), shows a broad hump signalling finite regions with localized charges as was also seen from the volume fraction data at this field value. Thus this indicator too points towards inhomogeneous melted state. For comparison, in the same panel we have shown data corresponding to $\lambda = 1.0$ (the dashed line), where the ground state is a uniform metal and the $P(Q)$ is distinctly peaked close to zero. The small shift in $P(Q)$ is due to the nature of the 2D tight binding band structure that prefers small Q_z values at every site. In a metallic state, where every site has equal average particle density, it leads to $P(Q)$ which has this signature. For $\lambda = 1.7$, the data in panel Fig. 4.9.(a)-(b) shows that $P(Q)$ is virtually independent of the magnetic field: the high field state is a ferromagnetic charge ordered insulator.

Fig. 4.9.(c)-(d) show the DOS for these λ and h combinations. These correlate well with the $P(Q)$, with the field generating a finite DOS at the Fermi level for $\lambda = 1.55$, while there is only a gap reduction (but no closure) for $\lambda = 1.7$. The gap reduction is related to the increase in effective BW in the CO phase as the magnetic order changes from CE to FM, removing the magnetic blocking of electron hopping. Let us elaborate on this a bit more. At large λ, the CO can be stabilized without the CE order on applying a magnetic field, of which $\lambda = 1.7$ is an example. This CO state is stabilized by kinetic energy gain from local excursion of the electrons as was discussed in Chapter.3. In this case, the transition from the CE to a FM background, implies four of its nearest neighbours (as opposed to two in the CE phase) have their spin parallel to the central spin. This increase in coordination allows for greater gain from local hops, making it easier to remove an electron from the CO state. This causes the reduction of the band gap seen in Fig. 4.9.(d).

To sum up, we see two different kinds of response to the applied field for systems with different λ, and the V_{CO} and $P(Q)$ results suggest inhomogeneous melting at intermediate λ. We now address the λ dependence more systematically.

Low λ regime:

We now take up Fig. 4.8.(a)-(b) and their resistivities shown in Fig. 4.8.(e)-(f), and discuss how they connect with the remaining plots in Fig. 4.8 that we discussed above. Fig. 4.8.(a) & (e) are at a slightly larger J than $J = 0.12$ to avoid hitting the FM-M phase as is seen from Fig. 4.7.(a). The rest of the plots in Fig. 4.8 are at $J = 0.12$.

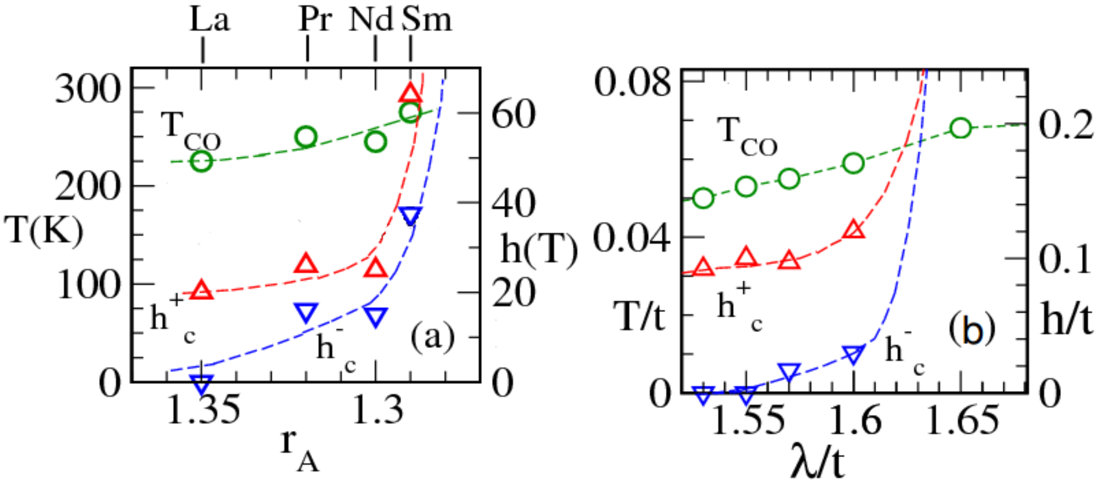

Figure 4.10: T_{CO}, and $h_c^{\pm}$ at low T - comparing experiment and theory. (a) Data from experiments, the $\mathrm{Ln_{0.5}Ca_{0.5}MnO_3}$ family, with weak disorder. Notice the rapid increase in $h_c^{\pm}$ with decreasing r_A at $r_A \sim 1.29$ in (a). (b) Our results on the λ dependence of T_{CO}, T_{CE} and $h_c^{\pm}$.

- The data at $\lambda = 1.40$ is shown to illustrate homogeneous melting of the CO state as opposed to inhomogeneous melting at higher λ. As Fig. 4.9.(a) shows, the V_{CO} reduces to less than 10% for $h/t > 0.09$ but the CO state recovers on reducing h. The small remnant value is related to low temperature field sweep rate, as is discussed in Sec. 4.4.2. Note that recovery of the CO happens for this 'low' λ system even though it does not for $\lambda \sim 1.45$, Fig. 4.9.(b). At $\lambda \sim 1.40$ the A-2D phase is much wider, probably rendering the FM-M unstable, rather than metastable, at $h = 0$.

- For $\lambda = 1.45$, the A-2D region is small and the FM-M remains metastable at $h = 0$ and the CO state is not recovered even when the field is swept back to zero. Further, in Fig. 4.8.(b) the system retains $\sim$ 25% of CO volume beyond h_c^+.

- In 4.8 (c) the system retains $\sim$ 30% of CO volume beyond h_c^+, and recovers the CE-CO-I state on field reduction.

- At $\lambda \sim 1.70$, as discussed earlier, the system retains a global CO at *all* h. The 'melting' field grows and diverges as λ increases beyond ~ 1.60.

Let us summarize our findings here. The increase in the melting fields with λ and systematics of recovery/non recovery of the CO with λ bear out what was discussed in Sec. 4.3.

If the system is close to the phase boundary, Fig. 4.7.(a), it would not be able to recover the CO state. Finally with increase in λ from 1.40 to 1.65, there is monotonic growth in the residual CO volume fraction in the field melted state, indicating inhomogeneous melting. Also if one takes into account the resistivity shown in the lower panel, over a certain λ regime it would imply that the system is a percolative metal.

While the results are suggestive, they do not prove that the finite field equilibrium state is inhomogeneous for the entire $\lambda = [1.40 - 1.65]$ window. The presence of metastable states can lead to trapping and complicate genuine phase separation. We shall elaborate upon this in Sec. 4.4, where we perform alternate calculations, using different protocols, to settle this issue.

Let us conclude this subsection by discussing a plot of T_{CO} and $h_C^{\pm}$ as a function of λ. Fig 4.10.(a) shows the variation of T_{CO}, and $h_c^{\pm}$ with r_A, for low disordered Ca family. These trends were discussed in Chapter.2. Here, we compare our results on the BW dependence of thermal and magnetic CO melting scales for disorderless (clean) system, Fig 4.10.(b). These scales were obtained from the data discussed earlier in this Chapter. While we will make detailed quantitative comparison later, here we observe that akin to the experiments, the melting scales increase with increasing λ or reducing r_A. Beyond a critical λ, the CO does not melt at any field. Finally we see that for $\lambda \sim 1.45 - 1.55$, the CO does not recover as happens for larger BW materials show in Fig 4.10.(a). Let us now look at the h-T phase diagrams at various λ values.

4.3.2 $h - T$ phase diagrams

Based on the indicators discussed, we can construct the $h - T$ phase diagrams at various λ values. This data allows for a comparison of trends between theory and the available experimental data in the low σ_A (Ca based) manganites as shown in Fig. 2.11. We will make qualitative comparisons in this subsection, and present results on the spatial character of melting in the next.

Fig. 4.11 shows the $h - T$ phase diagrams obtained at $J = 0.12$ and λ values indicated. These phase diagrams are obtained by sweeping in magnetic fields at various temperatures, by first cooling to the relevant temperature in zero field. h_c^+ and h_c^- denote the boundary of hysteresis and are taken as the field at which there is a sharp increase,

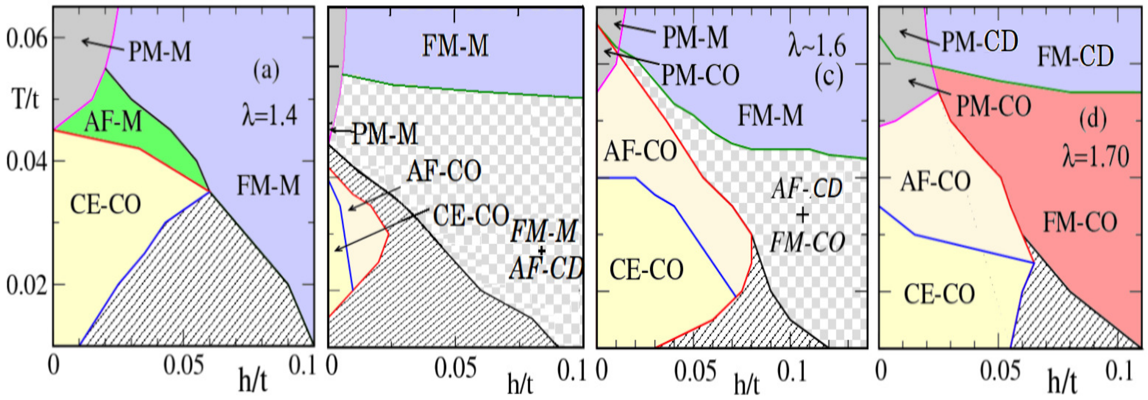

Figure 4.11: The $h - T$ phase diagrams obtained at various λ as indicated. The shaded regions imply hysteresis, light checkerboard regions imply phase separation and colored areas indicate equilibrium phases. At low T the hysteresis window shifts to higher fields as the CO correlations grow with λ. At low T both at low $\lambda(= 1.40)$ and high $\lambda(= 1.7)$, the system is uniform beyond the magnetic transition. At intermediate λ, $\sim 1.50 - 1.60$, the system phase separates beyond h_c^+. The hysteresis window for $\lambda = 1.50$ extends down to zero field, implying non recovery of the CO state. Increasing λ to ~ 1.60, recovers the CO state.

or drop, in the FM structure factor. We chose this convention because there is always a field driven CE to FM transition, although the CO may not melt.

The low temperature phases & general features: The evolution of the low T phases with increasing λ, Fig. 4.11, show the trends discussed earlier: (i) the increase in the melting fields with increasing λ, (ii) the homogeneous melting and subsequent recovery at $\lambda \sim 1.40$, (iii) the inhomogeneous melting at larger λ, and (iv) the absence of CO melting for $\lambda > 1.65$.

While we had seen the $P(Q)$ and the density of states for $\lambda = 1.55$ and $\lambda = 1.7$ earlier, Fig. 4.12 shows the same for $\lambda = 1.4$. The $P(Q)$ at $h = 0.1$ has a single peak close to zero, and the corresponding DOS has a finite weight at the Fermi level. This allows us to conclude that the melting is homogeneous. Note however, that the $P(Q)$, although, single peaked, has a broad feature which is related to some residual lattice distortions due to annealing issues, as will be discussed later.

The hysteresis window shrinks with increasing λ, an increase in temperature also narrows the hysteresis window. This window tapers off and closes at T_{CO}. The T_{CO} itself grows with increasing λ, as is also seen from Fig. 4.11. The increase in T_{CO} is

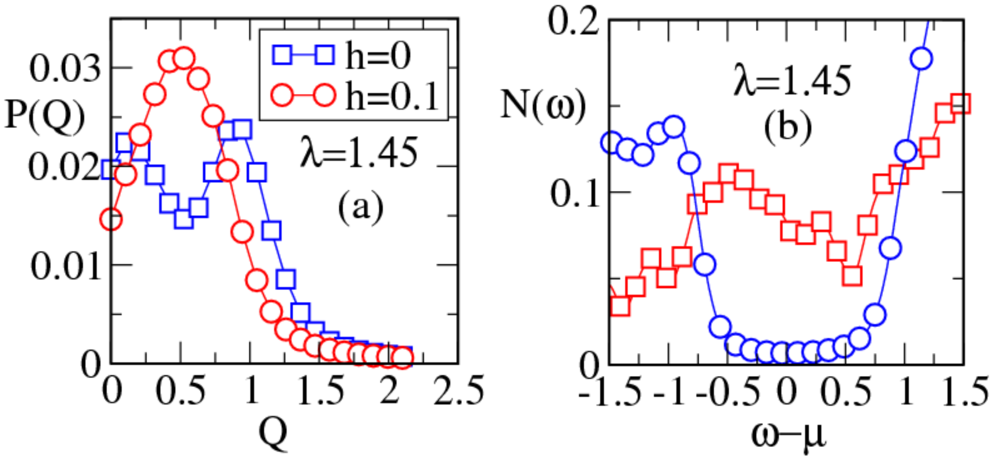

Figure 4.12: (a) The backround data at $\lambda = 1.4$, $J \sim 0.12$. (a) Low temperature (0.02) $P(Q)$ at zero field and at $h = 0.1$. (b) The corresponding density of states around the Fermi level.

due to increasing stability of the CO state with increasing λ. This increase in stability also manifests in shifting of the hysteresis window, at low T, to higher field values from left to right (Note that in Fig. 4.11.(d), the CO does not melt at all and the hysteresis corresponds only to the CE to FM transition).

Thermal evolution at low fields: At low λ, ~ 1.40, the loss of the CE pattern drives the system metallic, with no residual CO correlations. With increasing λ, however, the system has CO correlations surviving at progressively higher temperatures although the long range ($\mathbf{q} = (\pi, \pi)$) correlations get suppressed. The accompanying magnetic state at intermediate temperatures is a line like AF phase with $\mathbf{q} = (0, \pi)$ and $\mathbf{q} = (\pi, 0)$ correlations. This can be looked at as a precursor to the low temperature CE phase, where the $\mathbf{q} = (\pi/2, \pi/2)$ correlations (crucial to the CE phase) do not form at intermediate temperatures.

Further increasing the temperature essentially makes the system lose all spin-spin correlations and the systems end up in a PM phase. This is accompanied, at smaller $\lambda \sim 1.4 - 1.5$, by a metallic state, and at higher $\lambda \sim 1.6 - 1.7$, by a evolution into a charge disordered phase only after going through a CO one. The thermal PM-CO to PM-M transition, for $\lambda \sim 1.5 - 1.6$, signals thermal liberation of trapped carriers. This clearly brings out the stability of charge order at larger λ quite independent of the spin order. For $\lambda > 1.6$, to the temperatures accessed here, we observe only the conversion of the PM-CO to a PM-CD (shown for $\lambda = 1.7$). Here the PM-CD is a charge disordered (randomly pinned) polaronic insulator.

Thermal evolution at large fields: Let us contrast the low field evolution with that at large finite fields ($h > h_c^+$). Both for small λ (1.4) and large (1.7), the $h > h_c^+$ system loses AF correlations. At small λ the CO is lost completely at high fields. For $\lambda \sim 1.70$ where the CO does not melt, the systems evolve into a FM-CO phase. Increasing T will convert the FM-CO to a FM-M with thermal excitation of polaronic carriers although, as mentioned above, we observe only the FM-CO to FM-CD conversion.

Up to $T \sim 0.06$ the magnetic field prevents loss of the FM order. In contrast to the simple evolution at small and large λ, the intermediate λ situation (b)-(c) is complicated by phase separation. Beyond h_c^+ these systems separate into phases that are off $n = 0.50$. The constituents vary with changing λ. At $\lambda \sim 1.5$, the coexisting phases are ‘FM-M (n_1) + AF-CD (n_2)’ and those at $\lambda \sim 1.6$ are ’FM-CO (n_1)+AF-CD(n_2)’. The densities indicated in brackets are off half doping.

This phase separation is the origin of the inhomogeneous melted state and (for a slow field sweep) would make the melting transition continuous. These regions are indicated, in Fig. 4.11.(b) and (c), by light colored checkerboard. For both these λ’s the corresponding phase separated states evolve into a $n = 0.5$ FM-M. If the field were large enough to polarise all spins then for $\lambda \leq 1.60$, the system would be a $n = 0.5$ FM-M and above that it would be a $n = 0.5$ FM-CO.

At high temperature, the large field FM-M state, in (a) to (c), eventually give way to a PM-M phase with decreasing field, while in (d) the FM-CD on decreasing field gives way to a PM-CD. Also in (d), the FM-CO goes over to a AF-CO at $T \sim 0.03 - 0.05$ and to a PM-CO for $T \sim 0.05$. Further note that the green region in (a), that is absent in all other plots, is due to proximity to the AF-M phase in the $\lambda - J$ parameter space. To sum up, the $h - T$ phase diagrams highlight the following issues:

- Hysteresis associated with the field induced transitions.
- Increased stability of the CO state with increasing λ.
- Spin charge ‘decoupling’: CO independent of CE order at large λ.
- Phase separation tendency at intermediate λ and finite field.

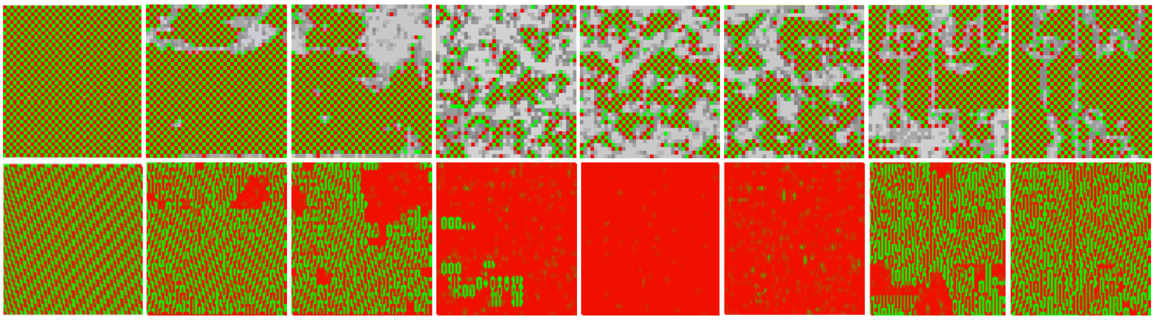

Figure 4.13: The spatial snapshots of charge ordered region (top panel) at $\lambda = 1.55$, $J = 0.12$ and the corresponding magnetic bonds (lower panel) at various magnetic fields. The red-green checker-board regions are the CO regions while the grey regions are the metallic (M) regions. For the lower panel, the red are the FM bonds while the green signifies AF bonds. The magnetic field sequence from left to right are $h/t =$ 0, 0.05, 0.06, 0.08, 0.20, 0.08, 0.02, 0 where, first the field is swept up starting at zero field, up to a maximum of 0.2 and then swept down back to zero field. Clearly, system recovers the CE-CO-I state after going through a percolative metallic phase at intermediate magnetic fields.

The detailed temperature evolution of low T phases in the $h - T$ phase diagrams in Fig. 4.11, that have not been experimentally reported yet, would be interesting to verify. We have not yet clarified the evolution of the PS state to the homogeneous limit at large h. However, before launching into that, we present real space snapshots lending support to inhomogeneous melting.

4.3.3 Spatial evolution of the CE-CO state

The spatial data that we provide here are snapshots of the real space charge density field and nearest neighbour magnetic correlations. These are tracked at different fields and low temperature.

We start with a CE-CO-I system at $\lambda = 1.55$. From the discussion in the previous sections, we know that a system at this λ melts and recovers CO on field sweeping. However, the melting appears to be inhomogeneous, given the residual V_{CO}. We will demonstrate that this is indeed an equilibrium effect in the next section. The spatial patterns are shown in Fig. 4.13, at various fields as indicated in the caption. The results are for a 40^2 system and have been obtained from a run in which h is increased from 0 to 0.2 in steps of 0.01, at $T = 0.02$, and then reduced to zero in the same sequence. The top panel shows the spatial charge ordering, while the lower panel shows the corresponding magnetic bonds (see figure caption for color convention). The primary steps in the evolution are:

- Nucleation of the FM-M within the CE-CO-I at low fields (as seen in the second and third columns from left).
- Sharp fall in the CO volume fraction, where the system becomes a patchwork of FM-CO, AF-CD and FM-M (fourth column).
- FM-M and FM-CO coexistence at very large field, $h = 0.20$ (fifth column).
- Partial recovery of the CE-CO state on downward sweep (columns 6-8).

On nucleation of the FM-M droplet the CE phase breaks up into regions of opposite ‘handed’ zigzag chains. These create CE domains. Within each domain the CO state survives but its stability is *locally* reduced at the domain boundaries. This reduction is small and is apparent in columns two and three where the system started out in the CO state at $h = 0$. It is also seen in the last two panels, where the system attempts to recover global CO from the melted state. Clearly in these cases some of the domain boundaries between CO regions coincide with magnetic domains boundaries of opposite handed CE regions. This makes it difficult to recover long range CO on large systems.

In column four, the system is in a coexistent state with FM-M, AF-CD and FM-CO coexisting simultaneously. This shows explicitly the inhomogeneous nature of melting arising out of the phase separation. Column five is for $h = 0.2$ which is large enough to polarize all the spins. This is deliberately shown to bring out the effects of low lying metastable states that can affect the numerics. For this λ the spin polarized problem has a global FM-M ground state. However, as seen, we find a coexisting FM-M and FM-CO. This happens because of the large region of metastability of the FM-CO phase, in which the system gets partially trapped. This affects the results even in column four and one needs an alternate calculation to extract the actual constituents of the *equilibrium* phase separated state. This is achieved via a fixed μ calculation, allowing the system to access relevant homogeneous states at finite h, described in the next section.

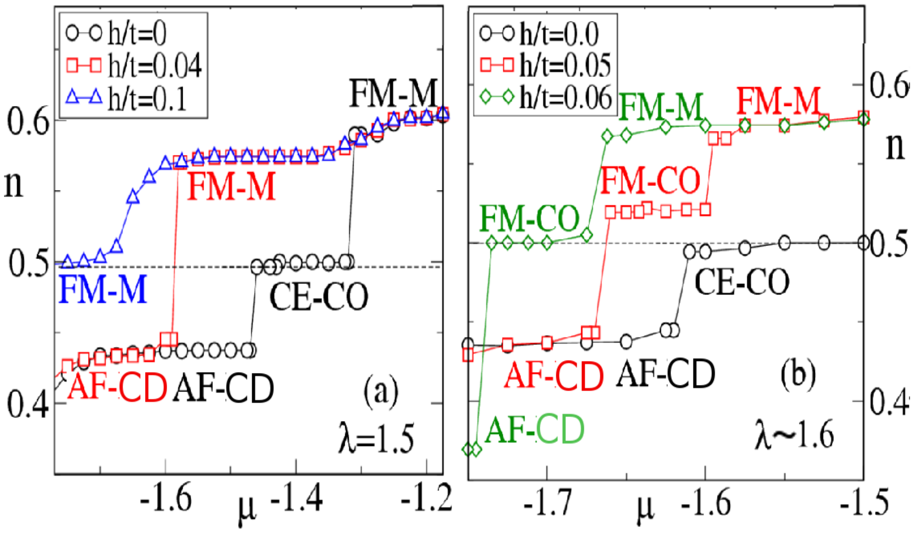

Figure 4.14: (a) and (b) show the $n-\mu$ curves at $\lambda = 1.50$ and $\lambda = 1.6$ respectively, at various fields as indicated. In both cases at intermediate fields, the system passes through phase separated states comprising of AF-CD and FM-M for $\lambda = 1.5$, and AF-CD and FM-CO for $\lambda = 1.6$. Further, at high fields both the system are characterized by uniform FM-M and FM-CO in (a) and (b) respectively. All results are obtained staying at $T = 0.02$ and $J = 0.12$.

4.4 Relation to the equilibrium state

4.4.1 Equilibrium phase separation

We need to verify that the equilibrium state is indeed phase separated at intermediate fields. This would be distinct from partial trapping of the system in some metastable state. We address this via a fixed μ calculation described below.

We cool the system at different μ, not necessarily targeting half-filling, to explore the vicinity of the $x = 0.50$ state at finite field. This yields the $\mu - n$ characteristic, and the various ground states, at finite h for a specific choice of electronic parameters. The $\mu - n$ curves are obtained from low temperature μ scans of the system, at fixed h, in a protocol that does not retain the memory of previous μ steps during the μ sweep.

These MC sweeps without memory avoid path dependence, since the system is annealed *ab initio* for each μ, and the fixed μ character allows the system to choose the 'best' possible n, thereby allowing access to the correct phase at any h. Moreover, we ensured that the system has annealed well enough by checking that our results hold up to large number (8000) of Monte Carlo steps at each μ. This ensures that the results are well annealed and free from low temperature Monte Carlo problems.

As seen in Fig. 4.14.(a), for CE-CO-I systems close to the FM-M phase ($\lambda \sim 1.5$) the CO is lost beyond $h \sim 0.02$. At a slightly higher field, the system prefers a FM-M state with $n = 0.57$ up to a certain μ and then directly goes to an 'A-type' AF phase at $n = 0.44$. If we were to stay at mean density $n = 0.50$ that state would be phase separated, the constituents being the FM-M and the AF-CD phases. This is true for all systems at $\lambda \sim 1.45-1.6$, and intermediate h. The situation is different for larger coupling, $\lambda \sim 1.6 - 1.65$. For a typical case, $\lambda \sim 1.6$ in Fig. 4.14.(b), at intermediate h the system prefers a FM-CO at $n = 0.52$ up to a certain μ and then an AF-CD at $n = 0.44$. Again, if we were to stay at mean density $n = 0.50$ the system will phase separate into the above constituents creating an inhomogeneous state. At larger fields, both in Fig. 4.14.(a) and (b), the $n = 0.5$ state becomes stable, recovering the correct asymptotic limits of FM-M for $\lambda = 1.5$ and FM-CO for larger $\lambda \sim 1.6$. Apart from confirming the earlier conclusion of inhomogeneous melting, this calculation helps identify the participants in the PS state.

If we look at the spatial snapshots for $h = 0.08$ and $h = 0.20$ in the field increasing run in Fig. 4.13, we find that the existence of the FM-CO in the ground state (for $\lambda = 1.55$) was due to its wide domain of metastability. This is not surprising, because at large h (spin polarised limit) the FM-M and FM-CO share a first order boundary. For the same reason FM-M fractions are trapped in the large field FM-CO ground state, for $\lambda \sim 1.60 - 1.65$.

4.4.2 Sweep dependence

From the $\mu - n$ calculations it is apparent that the melting is inhomogeneous for a window of couplings. For quasistatic variation of the applied field, for low λ (~ 1.4) and high λ (> 1.65), the expected transitions are abrupt. For intermediate λ, $\sim 1.45 - 1.65$, the expected transition is continuous. However as we will see, typical experiments and also our rate of sweeping the field do not allow for enough relaxation making both kinds of transitions appear abrupt. Here we discuss a schematic of such a transition. We use the ferromagnetic structure factor as an indicator for this discussion. For intermediate coupling the magnetic phase separation is between an FM and AF states. From their densities one can work out the volume fractions of the two constituent magnetic phases.

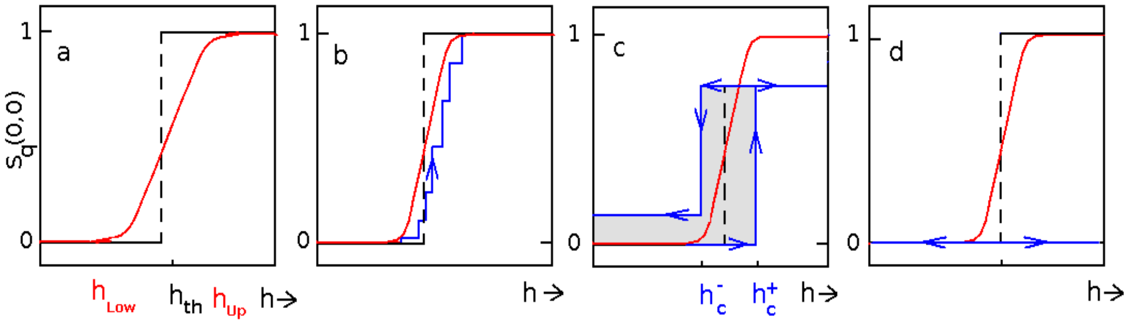

Figure 4.15: Schematic sweep rate dependence of the switching at intermediate couplings (λ). (a) Equilibrium evolution of the magnetization, $S_q(0,0)$, with h (red, solid line). h_{th} is a notional value at which a first order transition would have occurred in the absence of PS. The evolution of $S_q(0,0)$ (blue curves) for different sweep rates is shown in (b)-(d). (b) Slow sweep, (c) fast sweep (our regime, see text), and (d) ultrafast sweep. The text discusses the sweep rates in detail. In (c) the shaded region depicts hysteresis.

Fig. 4.15.(a) shows the magnetization with increasing field. The dashed line shows the notional abrupt (first order) transition which is the average of the critical field for transition in the forward and the backward field sweeps.The continuous line depicts the *expected* ‘transition’ whereby the magnetization grows continuously (from CE-type AF state) with increasing h to a FM state. The blue lines are a schematic for the MC response. The hysteresis that is observed occurs in the background of the unusual equilibrium physics involving phase separation. Since the magnetisation trace, *i.e*, the ‘switching’ in hysteresis, depends on the sweep rate let us clarify the experimental and simulation timescales.

The *local* relaxation time τ_{loc} in electronic systems is $\sim 10^{-12}$ seconds, but collective relaxation times τ_{coll}, say, can be macroscopic, $\sim$ 100 seconds in the CO manganites [105]. This measurement was at $\sim 0.9T_{CO}$ and τ_{coll} is likely to be much greater at low T. The field cycling periods τ_{per} that we could infer from field melting experiments were $\sim$ 10ms [106]. Overall $\tau_{loc} \ll \tau_{per} \ll \tau_{coll}$. Our MC results are broadly in the same window. The ‘microscopic’ timescale is the MC step. The sweep periods were $10^3 - 10^4$ MC steps (bigger in smaller systems) but still $\ll 10^{12}$ that one would need to avoid trapping in a metastable state.

The sweep rate dependence of the switching is illustrated schematically in Fig. 4.15, for an intermediate coupling system. The left panel, (a), is for a quasistatic sweep, $\tau_{per} \gg \tau_{coll}$. In this case there would be only progressive melting and no hysteresis, the

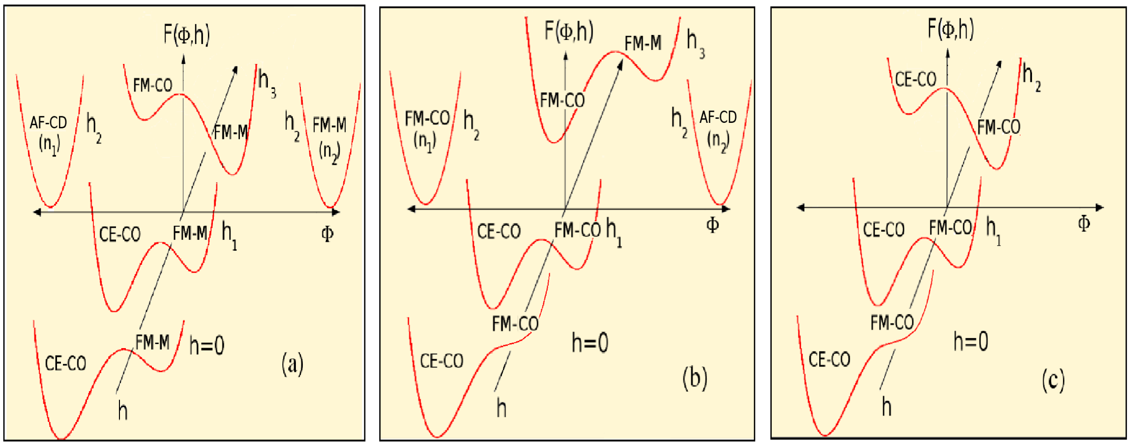

Figure 4.16: The low temperature Landau free energy landscape with the magnetic field axis going into the plane of the paper and the other axis, Φ, being the general order parameter axis. The three panels (a), (b) and (c) are representative of $\lambda = 1.5$, $\lambda = 1.6$ and $\lambda > 1.65$ respectively. All the phases are at electron density $n = 0.5$, except the ones for which a density are shown in brackets along with the name of the phase. The intervening A-type AF region is not shown to avoid cluttering.

system is always in equilibrium. Panel (b) illustrates the regime $\tau_{per} \sim \tau_{coll}$, where the sweep rate is still ‘slow’ but the system cannot quite track the equilibrium state. In this case there could be successive switching. This regime is also out of computational reach for the system sizes we use. Panel (c) is for our regime $\tau_{loc} \ll \tau_{per} \ll \tau_{coll}$. The system switches at h_c^+ on field increase, but not necessarily to the underlying equilibrium state. The magnetization, V_{CO}, etc, are determined by the presence of metastable states. For $h \gg h_c^+$, where the equilibrium state is a homogeneous FM (at this λ) the low temperature system can still remain trapped in the metastable state. Finally, (d) is for an ultrafast sweep, $\tau_{per} \sim \tau_{loc}$, where the system is unable to respond at all to the changing field.

As shown in panel (c), for sweep rates typical in the experiments and in our calculation, the high field state is influenced by the equilibrium PS *and* nearby metastable states. So, in any low T field sweep, for $\lambda = 1.55$ say, the observed state arises from a combination of equilibrium AF-M + FM-M phase coexistence and a metastable FM-CO. Increasing h converts the AF-M to FM-M but the metastable FM-CO fraction (also seen in Fig. 4.13, at $h = 0.2$) can be removed only by thermal annealing. At larger coupling, $\lambda \geq 1.6$, the high field low T state would have stable (equilibrium) FM charge order.

4.5 Landau framework for field melting

Over the earlier sections, we drew a number of conclusions regarding the λ dependence of the magnetic response. Here we suggest a Landau free energy landscape involving the relevant competing phases and organize the field response within a single framework.

While we do not present a Landau functional here, based on our results we schematically show an energy landscape in terms of some generalized order parameter. While deriving such a theory from the microscopic model is difficult, a heuristic construction could still be useful as an organising tool. A Landau theory with the provision of stabilizing both commensurate CO at half doping and incommensurate order off half doping [107] and the concomitant magnetic order has been studied before. This reproduces the qualitative $x-T$ phase diagram around half doping and exhibits phase coexistence in absence of either strain or disorder. Our landscape can help improve such constructs.

From the previous sections we know that the melting can either be homogeneous or inhomogeneous. For $\lambda < 1.6$ the system can melt the CO simply by lowering the energy of the FM-M minimum with increase in h. The increase in field can either lead to a simple first order transition, as happens for $\lambda \sim 1.40$ or lead to PS as happens for intermediate λ. In either case the loss of CO volume fraction is guaranteed. However for $\lambda \sim 1.6 - 1.65$, the FM-CO is closest in energy to the CE-CO-I (and also the true ground state in the limit of $h \to \infty$). Without the intermediate h phase separation, the CE-CO-I would have simply gone over to the FM-CO phase, as happens for $\lambda > 1.65$. The phase separation is crucial for the destabilisation of the CO for this λ window.

With this general understanding, let us discuss the Landau landscape shown in Fig. 4.16. This has three panels depicting the underlying free energy landcapes with increasing mangetic fields for three increasing values of λ.

Small λ response: Panel.(a) of Fig. 4.16 corresponds to $\lambda \sim 1.5$, where the CO state melts beyond a critical field but does not recover when the field is swept back. The $h = 0$ landscape has CE-CO-I as the global minimum and the FM-M is metastable. This metastable FM-M is responsible for the non recovery of the CE-CO-I state when h is swept back to zero. From $h = h_1$ to h_2, the FM-M minimum lowers as expected with increasing field. If the λ is small, ~ 1.4, this continues leading to a first order transition to a homogeneous FM-M. However, if $\lambda \sim 1.5$, at h_2 the system phase separates into off half doping phase (AF-CD + FM-M), these two minima are depicted in panel (a). On further increasing the field the system evolves into the large field $n = 0.50$ FM-M ground state. The phase that is closest in energy to this is the FM-CO, as is seen in Fig. 4.7.(a) at low J and $\lambda \sim 1.5$. Given the tendency to get trapped in the FM-CO, we depict this state as metastable at large fields.

Intermediate λ response: Panel.(b) shows a similar landscape for the $\lambda \sim 1.60 - 1.65$ range. There are a few important differences compared to panel.(a). (i) From Fig. 4.7.(a) the FM-CO phase is the closest to the CE-CO-I phase, that can be accessed by a magnetic field. (ii) Since we know that the CE-CO phase is recovered when the field is swept back, in the $h = 0$ landscape the FM-CO has to be unstable, as opposed to the FM-M being metastable at $h = 0$ in (a). (iii) The phase separation at intermediate fields is between FM-CO and AF-CD as depicted, which are off half doping phases. (iv) Finally, at large h the FM-CO is the global minimum and the FM-M minima is metastable, as is seen Fig. 4.7.(a) at low J.

Large λ response: This is shown in panel.(c). Like the small λ systems, the large λ systems have a simple field evolution. As in (b), the phase closest in energy to the CE-CO is the FM-CO and since the CE-CO state is recovered when the field is swept back to zero, this FM-CO state should be unstable at $h = 0$. With increasing h the FM-CO energy would lower and finally replacing the CE-CO as the global minimum. At large fields (not shown) the CE-CO would become unstable. Note here the CO does not melt and, in this view, if the intermediate h PS did not occur for $\lambda \sim 1.60 - 1.65$, CO melting would not have been possible.

To sum up, we have described the qualitative evolution of the free energy landscape with magnetic field. Let us now make a more quantitative comparison with the experiments.

4.6 Comparison with experiments

We end this section by making a quantitative comparison of various melting temperatures and melting fields with those found in the experiments. The table provided gives the normalised and absolute values (in Kelvin) of T_{CO} and $h_C^{\pm}$, for $J/t = 0.1$ and $J/t = 0.12$ for a couple of λ values. The normalised T_{CO} values are converted to Kelvin, using a hopping

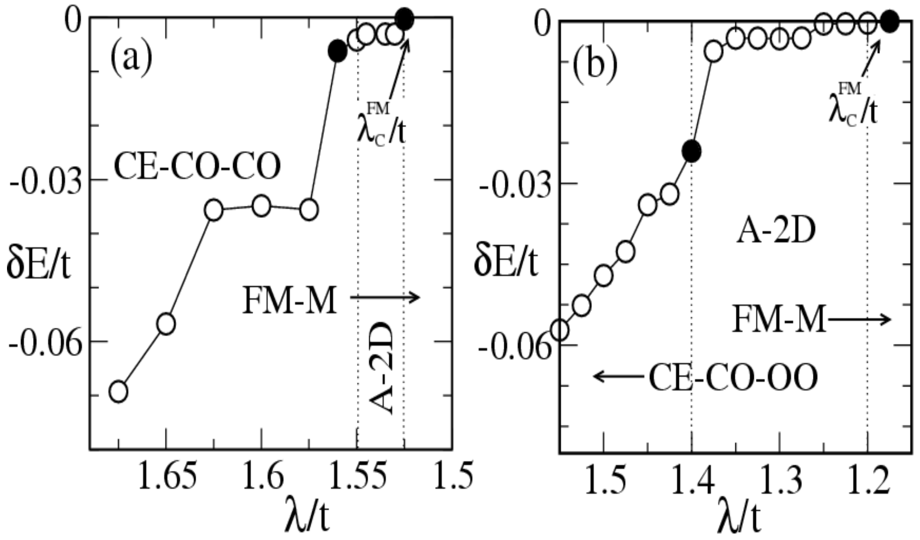

Figure 4.17: The energies of various phases obtained as a function of λ, measured from the energy of the FM-M phase closest to the FM-M, A-AF phase boundary of Fig. 4.7.(a). The black dots indicate the the energy difference between points closest to the A-AF region from both the FM-M and the CE-CO-I sides. (a) is for $J = 0.1$ and (b) is for $J = 0.12$. Note here A-AF refers to the line-like A-2D phase separating the FM-M and the CE-CO-I phases. Also 'closest' to a phase, say FM-M refers the closest we could approach the phase boundary within numerical accuracy.

scale $t \sim 0.2eV$ [7], and crude 2D to 3D factor of 3/2. The critical fields are converted to Kelvin using $g\mu_B h_C/t \equiv h$, again with $t = 0.2eV$. We find that for $J/t = 0.10$, the melting field are much smaller than the corresponding melting temperatures. Further, from Fig. 2.11, as a typical low disorder example, $\mathrm{Pr_{0.5}Ca_{0.5}MnO_3}$, has $T_{CO} = 250K$, while $h^+_{CO} \sim 27K$ and $h^-_{CO} \sim 17K$, giving the mean $h_{CO} = 22K$.

λ	J	$T_{CO}(K)$	$h^+_C(K)$	$h^-_C(K)$	$\frac{h^+_C+h^-_C}{2}(K)$
1.60	0.12	200	170	65	102.5
1.64	0.12	230	200	65	132.5
1.60	0.10	150	80	0	40
1.62	0.10	165	90	20	55

The smallness of the melting fields is better achieved if one tunes parameters close to $J/t = 0.1$ as compared to $J/t = 0.12$. The reason for this is seen in Fig. 4.7.(a), where, at $J/t = 0.10$, the CE-CO-I and FM-M phases are close by, while for $J/t = 0.12$, the two phases are separated by a bigger region of A-type AF phase. Fig. 4.17.(a) and (b) show the difference of the ground state energies (per site) between the CE-CO-I and A-type

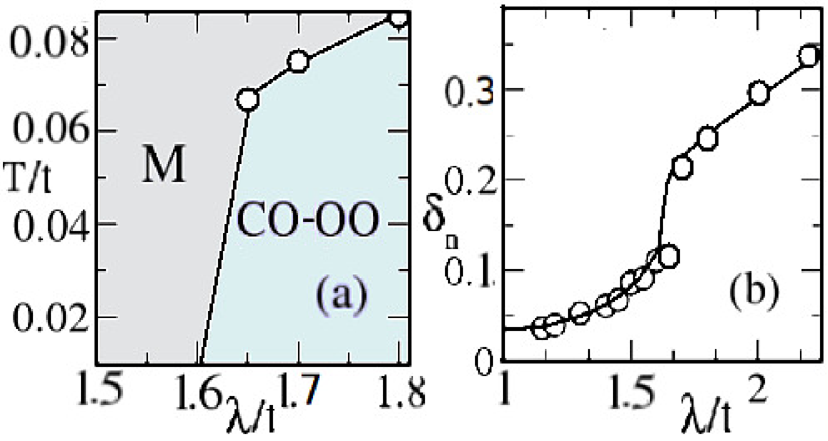

Figure 4.18: (a) The $\lambda - T$ phase diagram for the frozen classical spin case. (b) The disproportionation δ_n as a function of λ.

AF as a function of λ/t, from the FM-M phase, which is taken to be the reference phase.

$$\delta E = \frac{E_{FM}^{\lambda_{max}} - E^{\lambda}}{N}$$

where N is the system size. It is clearly seen that the case with $J = 0.10$ has the CE-CO-I ground state energy closer to the FM-M ground state energy, while the minimum possible difference between the two for $J/t = 0.12$, is ~ 0.03. Crudely, this is the barrier to be overcome by the applied field at low T. The smallest melting field achievable for $J/t = 0.12$ would be $\sim 42T$, for $\lambda/t \sim 1.4$. In principle if one tunes to J close to 0.1, such that the A-type AF region vanishes, one can get $h_c \rightarrow 0$.

4.7 Limiting case & numerical issues

4.7.1 Large field limit

All through, we have maintained that the homogeneous state at large fields is rather difficult to capture in the field sweep protocol. The infinite field or spin polarized limit would yield the critical λ below which the system is a FM-M and above which it is a FM-CO. Since this limit is spin polarized, we are effectively on the $J = 0$ axis of Fig. 4.7.(a). There are two equivalent ways of determining the critical λ. One is setting $J = 0$ and annealing the system at zero field from high to low temperature. The other is to freeze all the classical spins to a fixed direction and then to anneal the orbital/lattice variables.

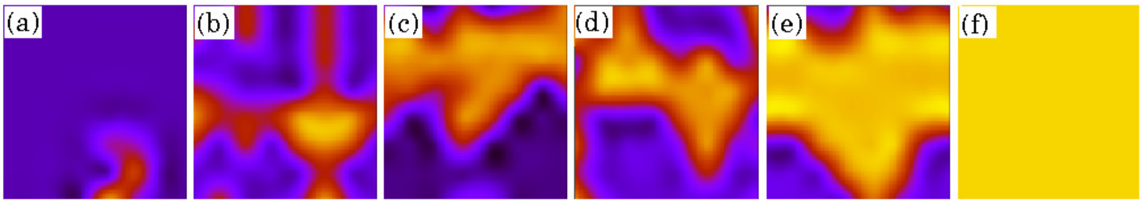

Figure 4.19: Real space map of CO (yellow) and metallic (blue) regions for the Janh-Teller problem (frozen spins). The λ values from (a) to (f) are, 1.4, 1.45, 1.5, 1.55, 1.6 and 1.65, respectively. These are taken at low temperature T=0.02.

Fig. 4.18.(a) presents the $\lambda - T$ phase diagram of the later approach. The parameter space, at low temperature, is divided into weak coupling ($\lambda < 1.6$) metallic phase and strong coupling ($\lambda \geq 1.6$) CO-OO phase. The T_{CO} increases with increasing λ/t as is expected. Let us now look at the electronic charge disproportionation δ_n as a function of λ/t. This is calculated by averaging the absolute value of the variation of n_i about 0.5, $\delta_n = \frac{1}{N}\sum_{i=1,N}|0.5 - n_i|$. Although this is a bulk measurement, judging by the trend of monotonic growth in δ_n in Fig. 4.18.(b), it is clear that even for $\lambda/t < 1.6$, there is some residual *local* CO regions. We have checked this explicitly by looking at snapshots as shown in Fig. 4.19. While above $\lambda = 1.6$, the system has global CO, the residual CO in the lower λ case are due to trapping in the CO metastable state.

So, although we have cooled the system and there is no low temperature sweep involved, there is still some amount of phase mixing due to the wide domain of metastability of the FM-CO. Thus it is bound to affect the low T field sweeps in the earlier calculations. We briefly discuss some general numerical issues below regarding stability of the results on annealing time and mention some general approaches to ascertain if a phase coexistent state is an equilibrium state or a result of metastable trapping.

4.7.2 Numerical checks

1. *Stability of phase separated state against MC relaxation:* Although TCA gains much in accessing large system sizes, accessing MC sweeps longer than $\sim 10^3$ on large systems is computationally very demanding. To ensure that we have annealed well enough, we repeated a few calculations on smaller systems employing standard exact diagonalization based Monte-Carlo. This was particularly done at parameter points

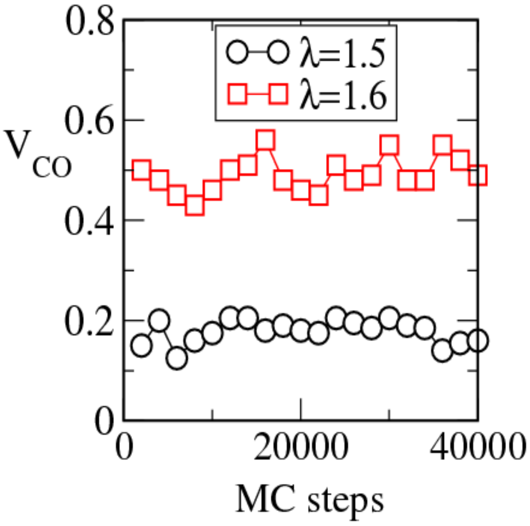

Figure 4.20: Remnant CO volume fraction vs number of MC steps after cooling the system in zero field to T=0.02 and increasing h in steps of 0.01, up to h=0.1. Then the system is allowed to relax for the 40000 MC steps at T=0.02 and h=0.1. The V_{CO} shown is for these 40,000 steps. Data is shown for two values of λ with different amounts of V_{CO}.

where the system phase separated in the TCA calculations. We studied the state obtained using the same protocol to large annealing times, $\sim$ 40000 MC steps. The phase separation remained stable even after such long runs. This is seen in Fig 4.20, where we plot the V_{CO} as a function of the number of MC steps. Note that the data is shown only for the relaxation steps after having cooled to T=0.02 and swept upwards in applied field and brought to $h = 0.1$. Then the system is allowed to relax for 40,000 steps at the same field and temperature point where the CO volume fractions are calculated.

2. *Long range magnetic order in 2D at finite temperature:* As we mentioned in Chapter.3, on finite 2D clusters, the 'ordering temperature' decreases with increase in system size. There is no long range order in 2D for an O(3) spin system. While this is true, the suppression of T_c is slow with increasing system sizes (up to 40^2). This allows us to extract a reliable effective excgange from large 2D clusters. Fig 4.21 shows the evolution of the magnetic structure factor S_q at $\mathbf{q} = (\pi/2, \pi/2)$ with temperature. This component is crucial and along with the $\mathbf{q} = (0, \pi)$ and $\mathbf{q} = (\pi, 0)$ forms the long range CE pattern. Note, the $\mathbf{q} = (0, \pi)$ and $\mathbf{q} = (\pi, 0)$ components

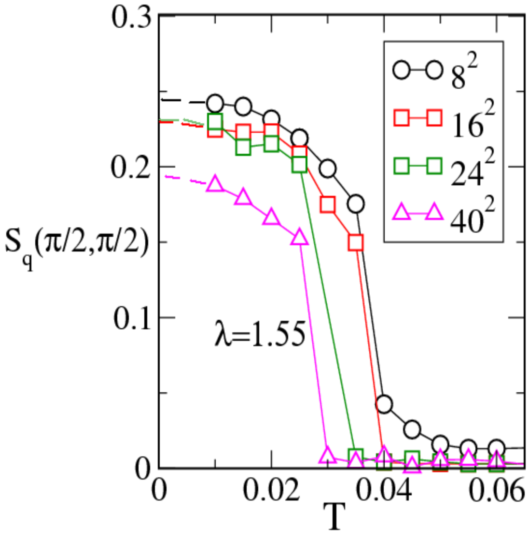

Figure 4.21: The variation of $S_q(\pi/2, \pi/2)$, crucial to form long rage CE magnetic order, with temperature at $\lambda = 1.55$ for different system sizes. This gives a measure of T_{CE}.

by themselves do not lead to long range order and only lead to short line-like stripes as was discussed in the beginning of this chapter. Thus the magnetic ordering scale is determined by the $\mathbf{q} = (\pi/2, \pi/2)$ component of S_q. In Fig 4.21, this is shown for different system sizes for a typical $\lambda(= 1.55)$ as a function of temperature. With increasing system sizes from 8^2 to 40^2, the T_{CE} gets suppressed from 0.04 to 0.03. Thus given the shift is not too large one can estimate the effective 2D exchange, and extrapolate to a rough 3D T_c from there.

4.8 Conclusions

We have discussed results on the field melting of charge order in half doped manganites using an unbiased Monte Carlo method. In this chapter we have dealt with the ‘clean’ case, mapping out the $h - T$ phase diagram exhibiting both hysteresis and re-entrant features. We found the melting to be inhomogeneous at intermediate fields and this stands as a testable prediction. We have made extensive comparison of the thermal and field melting scales between our calculations and experiments. Finally, from our numerical results we have established how the free energy landscape evolves with increasing field and changing λ. We take up disorder effects on the CO melting in the the next chapter.

Chapter 5

Melting in disordered systems

Chapter summary: This chapter discusses the field induced melting of charge order in the presence of disorder. We start with an analysis of the zero field CE-CO-I state in the presence of disorder. We then move to the field response of the disordered system and examine the spatial signatures and critical fields associated with melting. We continue with a discussion of low temperature field sweeps. Our results suggest a connection between the melting fields and the charge order 'stiffness' of the CE-CO phase, and allow us to identify the general principle controlling the melting phenomenon in half doped manganites. We conclude by comparing our results to experiments.

5.1 Disorder effects at $h = 0$

This chapter probes the effect of disorder on field induced melting of charge order in half-doped manganites. We will use a variety of indicators, *e.g*, (i) the volume fraction of charge order, V_{CO}, in a sample, (ii) the charge order structure factor, $D_Q(\mathbf{q})$ at $\mathbf{q} = \{\pi, \pi\}$, probing long range charge order, (iii) the magnetic structure factor, $S(\mathbf{q})$, and (iv) analysis of spatial snapshots of the charge density field n_i and short range magnetic correlation. These results, when combined with the lessons from the 'clean' problem, offer an unified explanation of the trends seen in the experiments.

Let us quickly recapitulate the kind of disorder and how it is parametrized. As discussed in Chapters.1, 2 and 3 we model A-site disorder via onsite potential fluctuations. The variance of this disorder Δ^2. From Fig 2.5, the Ca family, the Sr family, and the Ba family have progressively larger disorder. In Chapter.4 we compared our results on 'clean'

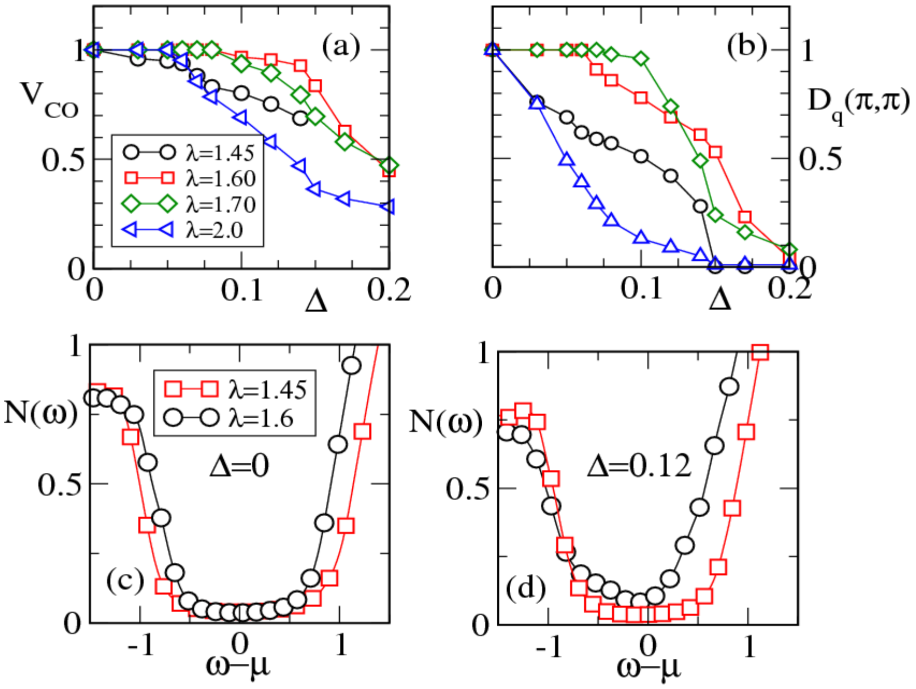

Figure 5.1: The variation of (a) volume fraction of charge order(CO) and (b) the long range nature of the CO state, i.e., the CO structure factor $D_q(\pi, \pi)$, with disorder strength at various electron phonon coupling (λ). Note the fall in the V_{CO} and $D_q(\pi, \pi)$ with disorder is most rapid for the low and large λ cases. Also note that long rangeness of the CO regions is lost much more rapidly with increase in disorder than the volume fraction of the CO itself. (c) and (d) show the density of states for weak and intermediate λ for clean and disordered cases as indicated. Note the formation of disorder induced pseudogap in (d) for $\lambda = 1.45$. All results are obtained for 16^2systems and are averaged over 20 disorder realisations.

systems to the low disorder Ca family, while the Ba based manganites did not support long range CE-CO due to their large disorder. In this chapter, the Sr family is of primary interest.

We begin by examining the effect of disorder in two limiting cases: (a) weak electron-phonon (EP) coupling (or large bandwidth) and (b) large EP coupling. At weak coupling, $\lambda \sim 1.45$, the CO state is "weak" with small modulation of the charge density. At strong coupling, $\lambda \sim 2$, the CO charge modulation is larger, almost $[0, 1]$ on alternate Mn sites. So, while the charge ordering is weak at weak coupling, the CO stiffness is weak at strong coupling as well, due to suppression of the kinetic energy that controls intersite correlation. The intermediate coupling regime, where both the charge modulation and the CO stiffness are reasonably large, will turn out to be more robust to disorder. The robustness of the clean zero field CO phase affects its response to disorder and applied fields.

Fig 5.1.(a) shows the disorder averaged volume fraction of charge order for various λ, while panel.(b) shows the corresponding $\mathbf{q} = (\pi, \pi)$ charge order structure factor. For both small λ, ~ 1.45 and large λ, ~ 2.0, the volume fraction of charge order decreases relatively quickly with increase in Δ. For intermediate λ, $\sim 1.60 - 1.70$, the CO volume fraction remains robust till $\Delta \sim 0.12$ and then drops. For $\lambda = 1.70$ V_{CO} falls slightly more rapidly than for $\lambda \sim 1.60$.

The CO structure factor provides a clearer picture of the way disorder destabilizes the CO state. For small (1.45) and large (2.0) λ values, V_{CO} remains relatively flat with small suppression in the CO volume fraction till $\Delta \sim 0.08$. But $D_Q(\pi, \pi)$ is already significantly reduced with respect to $\Delta = 0$. This indicates while local CO correlations survive, disorder induced domain walls reduce the long range coherence between different CO regions. For intermediate λ the system presents a single CO domain (in our small systems) till $\Delta \sim 0.12$, beyond which the order is destroyed quickly. These indicators demonstrate that the robustness of the CO state to disorder depends *non monotonically* on the electron-phonon coupling (or BW). As we will see later this is due to the weak CO stiffness at small and large λ where disorder easily disrupts long range order.

Fig 5.1.(c)-(d) show the density of states for weak and intermediate λ. The gap in the clean system at $\lambda = 1.60$, in (c), changes very little in the presence of moderate disorder, (d). For $\lambda = 1.45$, disorder softens the gap. As we show later, this ‘soft’ gap closes gradually on applying a magnetic field thereby ‘rounding off’ any abruptness in the melting transition. For large $\lambda > 1.65$, although the CO state is destabilized, the system remains insulating and the corresponding DOS shows no softening of the charge gap. The easy metallisation of the moderately disordered CO state at low λ is due to the formation of metallic droplets as spatial snapshots will reveal. For large λ, the disorder manages to disrupt the long range order by forming domains, but not metallise the system.

Fig. 5.2 shows the real space snapshots of the charge density n_i at three values of disorder (increasing from top to bottom: 0.08, 0.1 and 0.15) for four λ values (increasing left to right: 1.45, 1.6, 1.7 and 2.0). Fig. 5.3 shows the snapshots of the corresponding nearest neighbour magnetic correlations. CO domains boundaries in Fig. 5.2 and CE

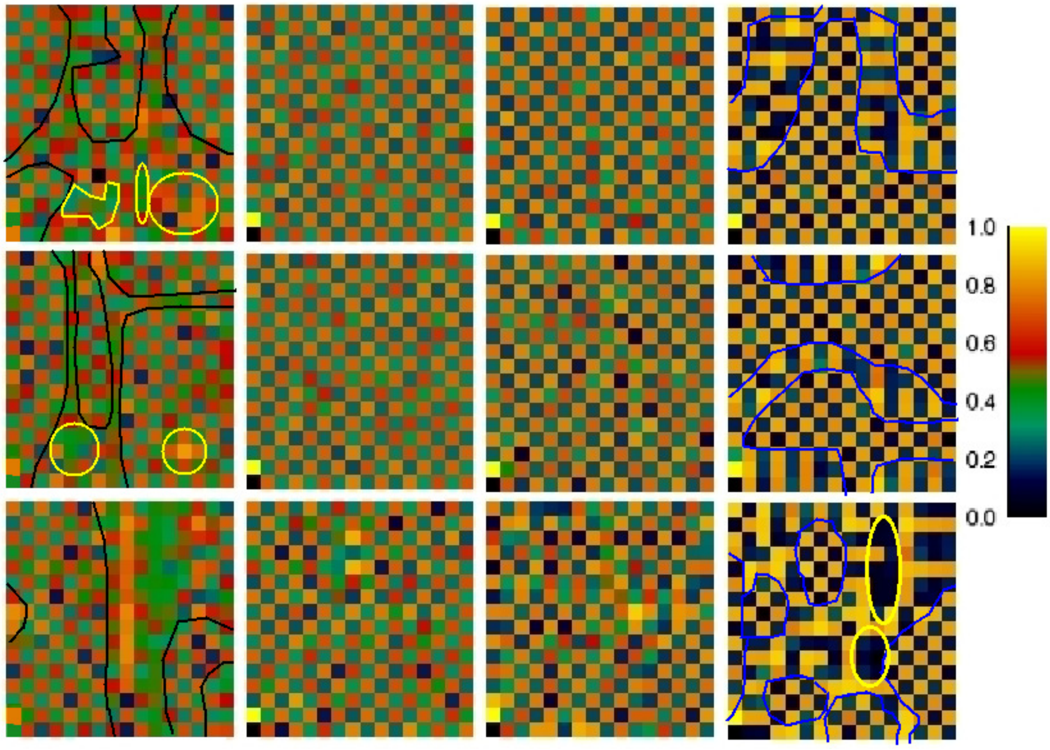

Figure 5.2: The spatial variation of the electronic charge densities for four λ values $(1.45, 1.6, 1.7, 2.0)$, from left to right. Top to bottom: weak ($\Delta \sim 0.08$), intermediate ($\Delta = 0.10$) and strong ($\Delta = 0.15$) disorder. For $\lambda = 1.45$, the CO domain boundaries are marked by black lines and typical small metallic (charge uniform) regions, green or orange in color, are encircled in yellow for $\Delta = 0.08$ and 0.1. The large metallic patch is seen at $\Delta = 0.15$. For $\lambda = 2$ the CO domain boundaries are marked in blue for all three disorder values and two regions almost devoid of electronic density are encircled in yellow for $\Delta = 0.15$. Note that the size of the CO domains, for $\lambda = 2$, decrease with increasing disorder.

domain boundaries in Fig. 5.3 are traced out by black lines.

(i) *Weak and strong coupling:* At small disorder, the low $\lambda(= 1.45)$ case (extreme left column of Fig. 5.2) develops small metallic patches (uniform green or yellow regions, typical regions are encircled in yellow), associated with local disruption of the CE chains leading to small FM or line like A type regions. With increase in disorder, the number and size of the metallic regions grow along with appearance of line-like AF and FM regions, as seen for $\Delta = 0.15$ in Fig. 5.3. While the domain wall formation between CO patches, as indicated in Fig. 5.2, accounts for the rapid suppression of the $D_Q(\pi, \pi)$, the decrease of V_{CO} with disorder is due to formation of metallic regions.

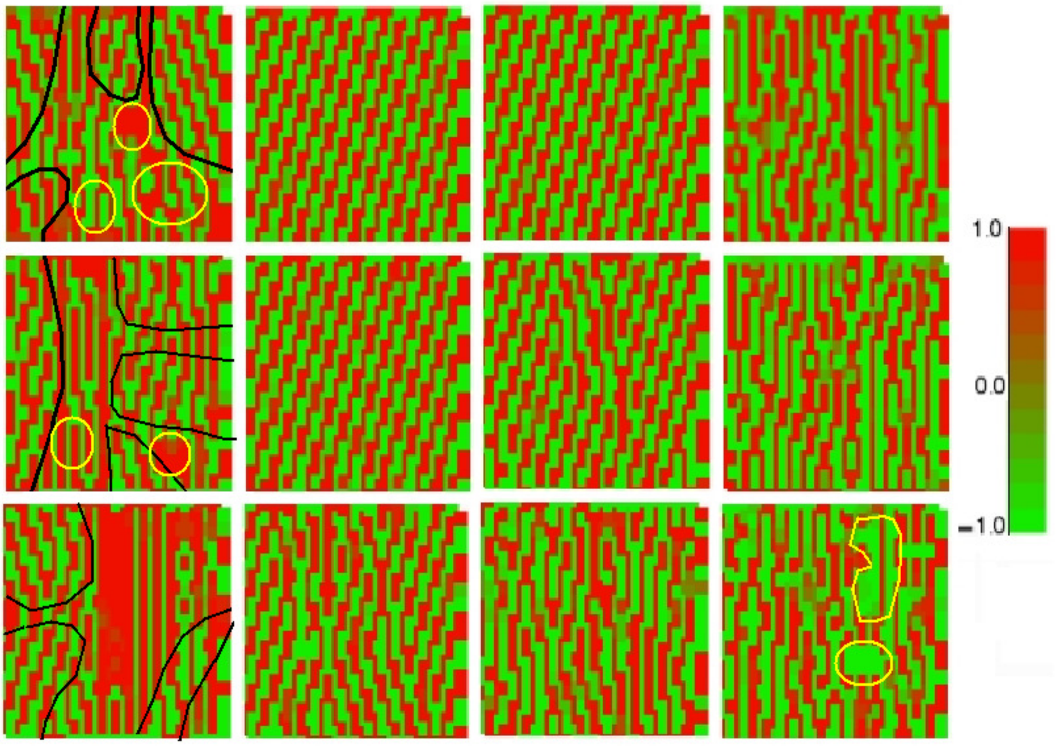

Figure 5.3: Snapshots of the nearest neighbour magnetic correlation corresponding to the charge density profile shown in the earlier Fig. 5.2. As earlier, the patterns are for four λ values $(1.45, 1.6, 1.7, 2.0)$, from left to right, at weak (~ 0.08), intermediate(0.10) and strong(0.15) disorder strengths. In the color code, minus one (green) indicates perfect antiferromagnetic bonds and plus one (red) indicates perfect ferromagnetic bonds. For $\lambda = 1.45$, the CE domain boundaries are marked in black. Also, encircled in yellow, are some regions where disruption of the CE order lead to metallic region (marked in yellow in Fig. 5.2).

At strong coupling $\lambda = 2$, the CO state involves site localised electrons with virtual hops stabilising the checkerboard order. Disorder converts this to polaronic insulator with 'randomly' located electrons having short range charge correlations. In Fig.5.2, the orange-black contrast in the CO domains are almost $n_i = 0/1$ (see the color bar in the figure). This is typical of CO at large λ. The size of the CO domains shrink with increasing disorder, with the intervening region having randomly pinned electrons as is seen with increasing disorder.

In the regions where $n_i \sim 0$, the antiferromagnetic superexchange dominates and leads to G-type magnetic order, (corresponding regions are marked in the right bottom corner in Fig. 5.3). So, the suppression of $D_Q(\pi,\pi)$ is due to disordered polaronic insu-

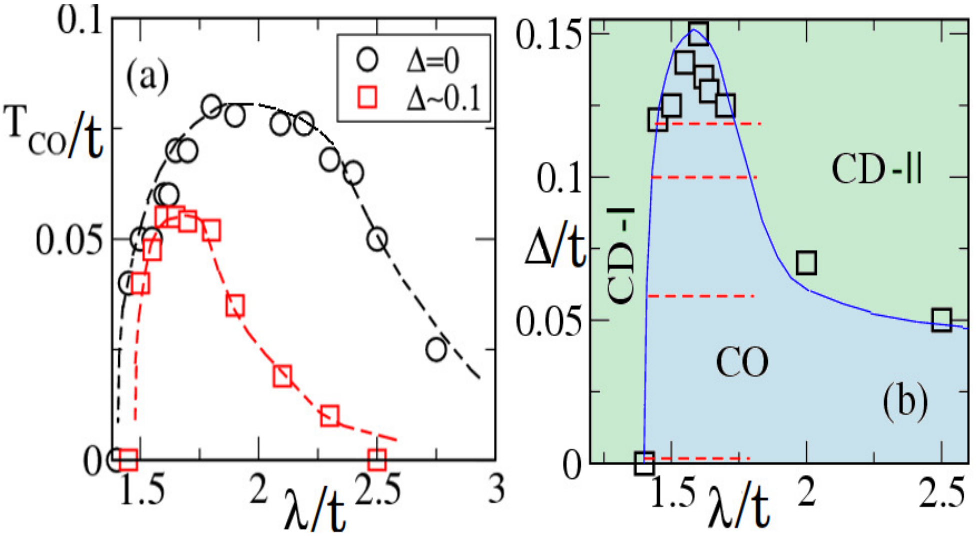

Figure 5.4: (a) The variation of T_{CO} with λ at $\Delta = 0$ and $\Delta \sim 0.1$. (b) The $\lambda - \Delta$ phase diagram. Note, the charge disordered regions at weak $\lambda < 1.45$ is different from that which occurs at larger $\lambda > 2.$. The weaker λ (CD-I) is a disordered ferromagnetic metal (on our small systems). The large λ, the CD region, CD-II, is a charge disordered polaronic insulator.

lating regions separating the CO domains and the suppression of V_{CO} is due to shrinking of the CO domains with increasing disorder.

At small λ, the CO disproportionation is small, so weak potential fluctuations can disrupt the CO. At large λ, the CO stiffness is weak and a small random potential can affect this stiffness by randomizing the energy gain from local hops. The sensitivity of the CO state to disorder increases with increasing λ, beyond a threshold λ.

(ii) *Intermediate coupling:* At intermediate λ the CO state remains robust to moderate disorder. This lack of sensitivity to disorder, in contrast to the weak and strong λ cases, can be understood as follows. In Chapter.4 we saw an increase in the T_{CO} with increase in λ, crudely signalling the increase of the CO stiffness. However, we will see that beyond $\lambda \sim 1.9$ the T_{CO} falls with increasing λ. The response of the CO state to disorder can be understood in terms of the non-monotonicity of the $\Delta = 0$ CO stiffness with changing λ. Clearly since the CO stiffness reaches its maximun at intermediate λ, the CO is most stable to disorder in this regime.

5.1.1 The $\lambda - \Delta$ phase diagram

Fig 5.4.(a) shows the variation of T_{CO} with λ at $\Delta = 0$ and at $\Delta \sim 0.1$. The $\Delta = 0$ case bears out our earlier description of the CO being most stable at intermediate λ. The $\Delta \sim 0.1$ case is *qualitatively similar* to the clean problem. From this data we can put together the $\lambda - \Delta$ phase diagram shown in Fig 5.4.(b). This will be of value in understanding the experiments. The $\lambda - \Delta$ phase diagram shows the CO region between two charge disordered regions CD-I and CD-II. CD-I is a FM-M at $\Delta = 0$ and a disordered FM-M at finite disorder (in our small clusters). CD-II is the disordered polaronic insulator, with randomly pinned electrons, at large λ that we discussed above.

If we look to extend this phase diagram to larger λ, it will asymptotically go to zero for $\lambda \to \infty$, as the CO stiffness will go to zero. This is so because at $\lambda = \infty$, the electrons are perfectly site localized and there is no gain from the kinetic term that otherwise allowed for local electronic excursions. Thus at any large but finite λ, there is a small Δ that will disrupt the CO state.

The effect of disorder on the CO state at large λ is akin to the effect of a random field on Ising systems as in random field Ising model (RFIM), where the magnetic exchange competes with the random field [110]. Our problem at large λ is similar, with the effective exchange being replaced by the charge order stiffness as embodied in the T_{CO} scale. At low λ the CO region is bounded by the weak λ homogeneous phase. The window of CO rapidly narrows with increasing Δ and there seems to be no CO phase beyond $\Delta \geq 0.15$. We shall look at the effect of system size on the critical disorder later.

5.2 Field sweep in presence of disorder

Let us now look at the field response of the CE-CO-I state in the presence of disorder. We track the field induced melting of the CE-CO-I in the disordered background and compare to what we found in the clean case.

Fig 5.5 and Fig 5.6 depict aspects of the evolution of the CE-CO-I state as we sweep the magnetic field after cooling the system (in zero field) to low temperature. Fig 5.5 tracks bulk properties such as V_{CO}, $S_q(0,0)$ and ρ, as a function of applied magnetic field in the clean (a), (c), and disordered (b), (d), cases. Fig 5.6 looks at the actual

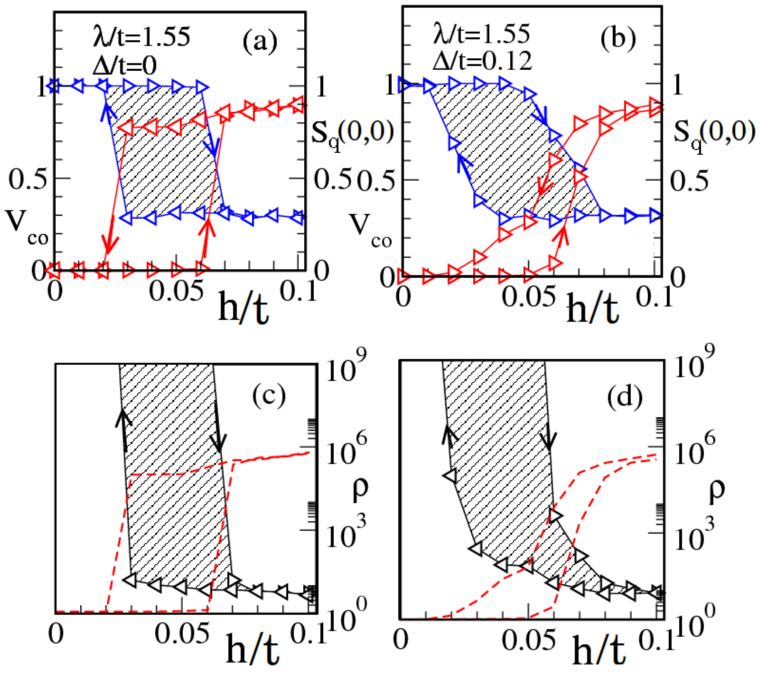

Figure 5.5: The comparison of various physical quantities V_{CO}, $S_q(0,0)$ and ρ for the clean and the disordered cases. The sharp transitions, in (a), in the clean case are replaced by a smoother and 'rounded' transition in V_{CO}(blue curves) in (b). The accompanying S_{FM} ferromagnetic order parameter(red curves) reaches its maximum (unity) through a series of small steps in (b) as opposed to a sharp jump in (a). The resistivity(black curves) in (d) also similar behaviour of changing in small steps in contrast to the sharp change in (c).

spatial profile of CO melting. The spatial profile in Fig 5.6, for the clean system (top panel) is seen to sustain CE-CO-I up to $h/t = 0.06$, beyond which it abruptly goes to a percolative FM-M state. The disordered case (bottom panel) shows a more gradual trend in the melting. It starts by creating small metallic regions which grow with increasing h to reach the percolative metallic state. This gradual loss of CO volume fraction is corroborated by Fig 5.5.(b) and the abruptness of the transition on the clean case is correlated with Fig 5.6.(a).

The metallic character is seen from the resistivities shown in Fig 5.6.(c) and (d) which track the abrupt change in V_{CO} in the clean case and gradual change in disordered case. The field induced transition occurs through a phase separation at intermediate fields. If tracked quasistatically it will show a continuous change in the volume fraction and the magnetization. However, the experimental sweep period (and that of our simulation in

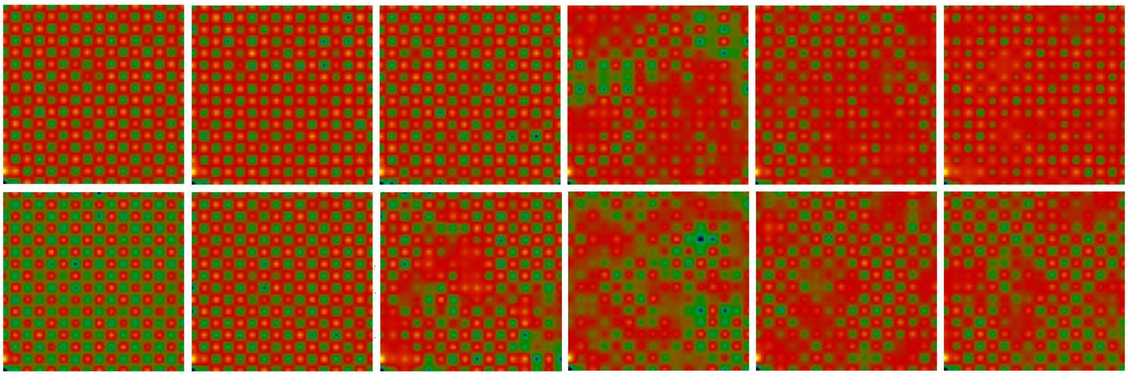

Figure 5.6: The spatial snaphots of charge densities for zero field cooled samples, which are then subjected to a sweep in the magnetic field at low temperature for clean (Top panel) and disordered($\Delta = 0.12$) (Bottom panel). The snapshots are shown for field values (h/t=0.04, 0.05, 0.06, 0.07, 0.08, 0.09) from left to right, for the increasing part of the field cycle. The corresponding CO volume fractions are shown in Fig 5.5.(a) and (b). Clearly, in the clean case, the CO remains stable up to $h \sim 0.06$ and then collapses within a window of $\Delta(h) = 0.01$ to a state with about 30% CO regions and 70% FM-M. The disordered case however, starts losing the CO state beyond $h = 0.05$ and collapses, within a window of $\Delta(h) = 0.04$ into a percolative metallic state with roughly similar composition as in the clean case.

Monte Carlo steps) is much smaller [51] than the typical relaxation time of the system [52]. The abruptness in the clean transition is due to this.

At the same rate of field sweep, the field induced transition in the disordered system is already rounded. As seen in Fig 5.7 the soft charge gap at $h = 0$ and low λ evolves continuously with increasing field. The corresponding distribution function of lattice distortion, $P(Q)$, shown in Fig 5.7.(a) also loses the twin peak profile at low h to a broad hump, signalling an inhomogeneous state. This transition to the inhomogeneous state is also gradual. At large fields, the metal in Fig 5.5 is inhomogeneous. A remnant volume fraction in the clean case, Fig 5.5.(a), was due to the PS tendency in the presence of the magnetic field. We see a similar remnant CO volume fraction in the disordered case. It is difficult to separate the inhomogeneity induced by disorder and PS tendencies. However the disorder induced nonequilibrium coexistence can be removed by thermal cycling.

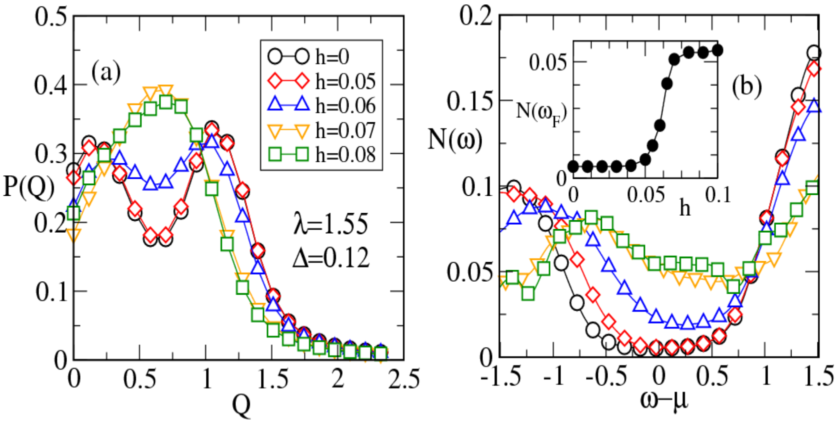

Figure 5.7: (a) $P(Q)$ and (b) DOS at various magnetic field values for $\lambda = 1.55$ and $\Delta = 0.12$. The disorder induced smoothing of the transition is clearly seen. Inset in (b) shows the gradual increase in the weight at the Fermi level with increasing fields.

5.2.1 Melting trends with disorder

Let us examine the thermal and field melting scales for varying coupling strength and disorder. To help make a comparison with experiments, we quickly restate the key experimental results. For systems with $\sigma_A \sim 10^{-3}A^2$ (e.g. the Ca family), the melting field increases with decreasing r_A, but for systems with $\sigma_A \sim 10^{-2}A^2$ (e.g. the Sr family) the melting scales initially increase and then collapse for decreasing r_A. These results are discussed in Chapter.2. We follow the same $h - T$ protocols as in the experiments, *i.e*, we sweep up and down in h at low T after cooling at $h = 0$. In terms of the numerics we start from zero field, increase the field up to $h/t \sim 0.2$, and then reduce to zero in steps of 0.01. As discussed earlier, the forward melting field is defined as h^+_{CO} and that in the downward sweep is h^-_{CO}. Fig 5.8.(a)-(d) show the variations of T_{CO} starting with $\Delta = 0$ (in (a)) to strong disorder $\Delta \sim 0.12$ (in (d)). Fig 5.8.(e)-(h) show the variations of the corresponding melting fields.

Apart from the expected overall suppression of melting scales with disorder, there is a gradual *downturn* with increasing λ in the disordered case. In (a) and (e) the thermal melting scale increases and the melting fields diverge, i.e., the CO state is stable without CE order beyond a critical λ. In (b) and (f) the melting fields become finite in the same λ regime, and both the thermal and the magnetic melting scales start to dip towards the higher λ end. They begin to get strongly suppressed in (c)-(g) and (d)-(h) where the

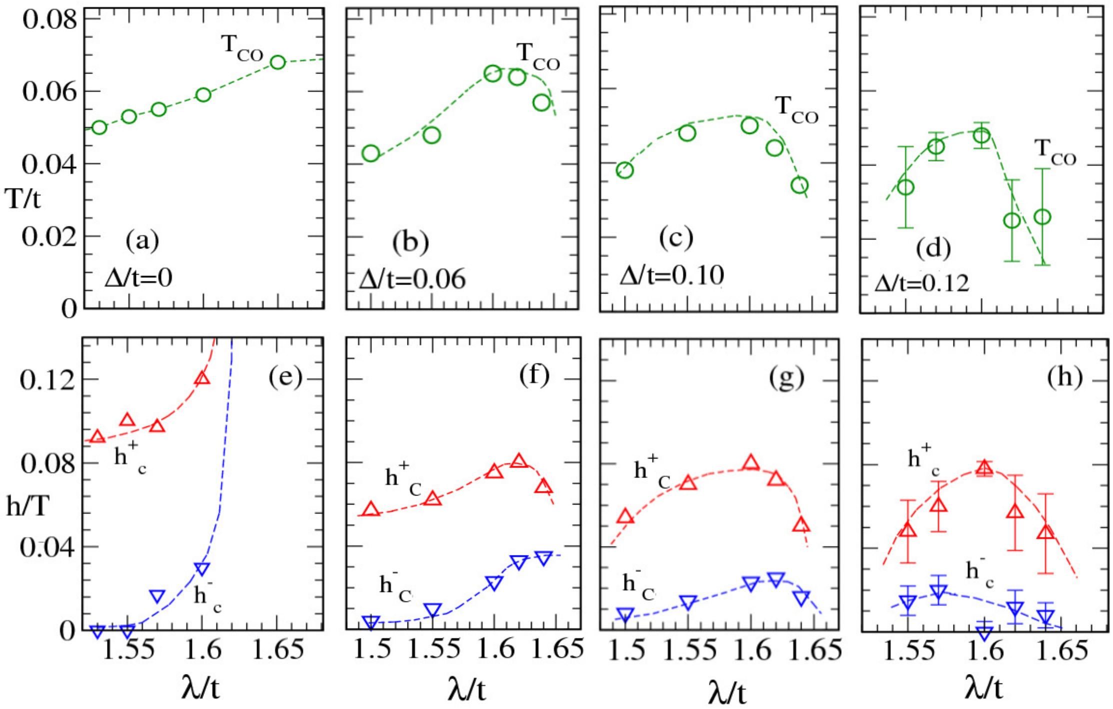

Figure 5.8: (a) to (d) show the λ dependence of the disorder averaged T_{CO} and (e) to (h) the corresponding h_{CO}^{+} and h_{CO}^{-}, for $\Delta = 0, 0.06, 0.1, 0.12$ respectively. While for $\Delta = 0$, the melting fields diverge beyond a critical λ and the T_{CO} grows, in the λ window shown, increasing the strength of disorder Δ not only suppresses the overall melting scales, but also changes the λ (or r_A) dependence qualitatively. Within the same λ window, increasing disorder causes a gradual downturn in all the melting scales at weak disorder and finally strongly suppresses these scales at strong disorder $\Delta \sim 0.12$. Error bars for the strong disorder case (d) are the largest and are given as an estimate of the maximum error in the numerics.

disorder is larger.

To explain the results we refer back to Fig 5.4.(b), the $\lambda - \Delta$ phase diagram. There we have marked the (λ,Δ) combinations used here by red dashed lines.

From Fig 5.4.(b) it is clear that at $\Delta = 0$ the system has only one boundary with the CD-I region, so the melting scales are the smallest at $\lambda \sim 1.45$ and increase with increasing λ. For all other dashed lines the system encounters boundaries with CD-I and CD-II, so there is a suppression in the magnetic and thermal melting scales at both λ ends. The presence of disorder causes a competition between the long range order of the CO state and random pinning effects of disorder which weakens the effective CO stiffness

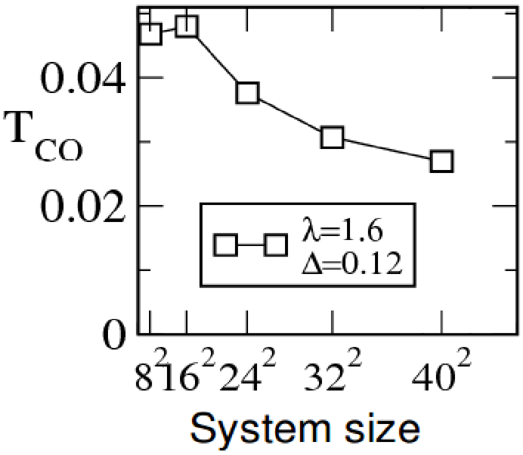

Figure 5.9: Variation of T_{CO} with system size at $\Delta = 0.12$.

and hence the melting temperatures and melting fields.

The large λ weakening of the CO state and the presence of the FM-M at low λ places the CE-CO-I in a relatively narrow λ window. A qualitative match can be made if we consider the Ca family to be at low Δ, the Sr family, in the same λ regime, to be at $\Delta \sim 0.12$, and the Ba family to be at $\Delta > 0.15$. The $\lambda - \Delta$ phase diagram gives a natural framework to unify the clean and disordered field melting phenomena. Further, as discussed earlier, the nonmonotonic response of the CO stiffness actually stems from the $T_{CO}(\lambda)$ in the $h = 0$ non disordered case.

As discussed in Chapter.3, to check the reliability of extracting T_{CO} from these disordered finite 2D systems, we look at the scaling of the T_{CO} with system size. Fig. 5.9 shows the fall in T_{CO} with system size at largest disorder we have used to compare with experiments ($\Delta = 0.12$). We see that there is a fall in the thermal melting scale with system size, however for the disorder used the fall is not too rapid allowing us to estimate the melting scales.

5.2.2 Comparison with experiments

We conclude this chapter by making some comparison with experimental data. In Chapter.4, Sec. 4.6 we discussed the quantitative comparison with experiments of the magnetic melting scales and their smallness compared to the thermal melting scales. Based on the discussion in this chapter, now we present the full comparison of the bandwidth depen-

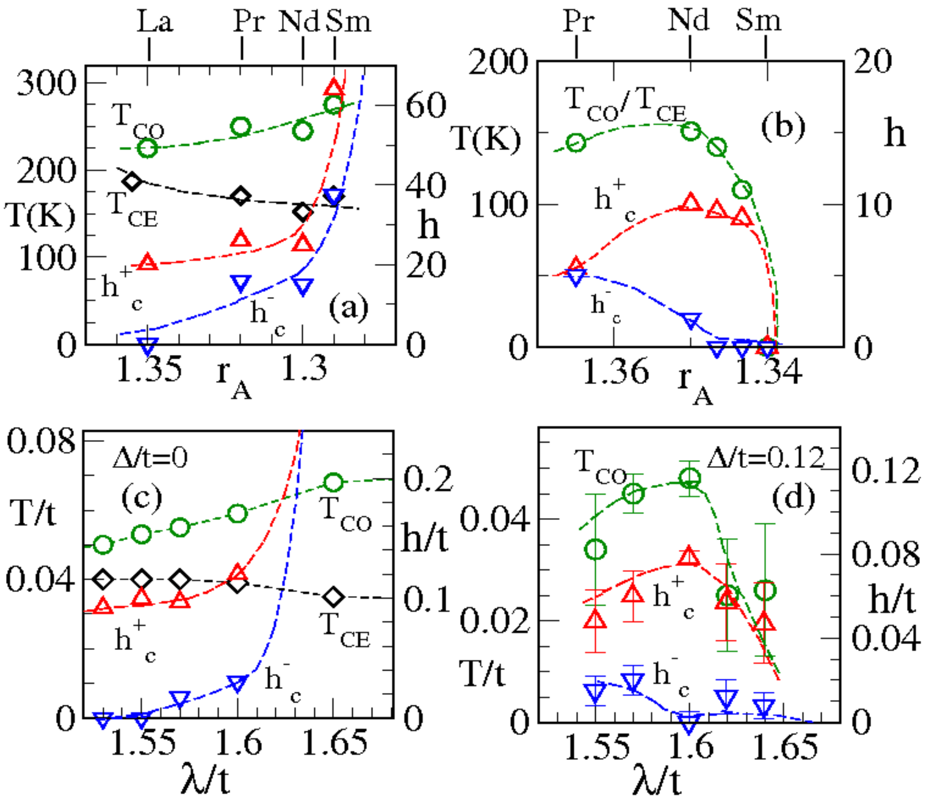

Figure 5.10: T_{CO}, and $h_c^{\pm}$ at low T - comparing experiment and theory. (a)-(b) Data from experiments: (a) the $\mathrm{Ln_{0.5}Ca_{0.5}MnO_3}$ family, with typical $\sigma_A \sim 10^{-3}A^2$, (b) the $\mathrm{Ln_{0.5}Sr_{0.5}MnO_3}$ family with typical $\sigma_A \sim 10^{-2}A^2$. Notice the rapid increase in $h_c^{\pm}$ with decreasing r_A at $r_A \sim 1.29\ A$ in (a), and the *collapse* of $h_c^{\pm}$ with decreasing r_A at $r_A \sim 1.34$ in (b). (c)-(d) Our results on the λ/t dependence of T_{CO}, T_{CE} and $h_c^{\pm}$. (c) Clean limit $\Delta/t = 0$, (d) disordered systems, $\Delta/t = 0.12$. The lines are a guide to the eye.

dence melting in the clean and disordered cases.

Fig 5.10.(a)-(b) show the experimental data on the bandwidth dependence of the CO melting scales both for the clean and moderately disordered half doped manganites. In the clean case, the Ca family, from $r_A = 1.35$ to $r_A = 1.32$, the T_{CO} and the $h_c^{\pm}$ grow with decrease in λ. In sharp contrast, in the moderately disordered Sr family, in a similar bandwidth range, these scales are strongly suppressed with decreasing r_A. Fig 5.10.(c)-(d) show the same trends as calculated in our work. In Fig 5.10.(c), the increase of the thermal melting scales and the divergence of the magnetic melting scales with decrease in λ is clearly due to increase in the robustness of the CO state with increasing λ up to some critical $\lambda \sim 2.0$, as discussed. In the same range, the moderately disordered case, Fig 5.10.(d), clearly captures the non-monotonic dependence of the melting scales as seen in the experiments, Fig 5.10.(b). We also notice there is an overall suppression of all the melting scales in the disordered cases compared to the clean results.

5.3 Conclusions

Results:

Using a real space Monte-Carlo scheme we have shown how the charge ordered state in the half-doped manganites is affected by the presence of disorder and an applied magnetic field. We illustrated the disorder induced broadening of the melting transition and how the zero field disordered state reacts to field sweep. We could explain the counter-intuitive bandwidth dependence seen in the Sr based manganites. We demonstrated that the non-monotonic behavior of the CO stiffness with λ in the clean problem, and random pinning effects of disorder, leads to an unified picture, via the $\lambda - \Delta$ phase diagram.

Unsolved issues:

The issues that we did not clarify relate to the effects of disorder on the kinetics of the phase transition. As discussed in Chapter.2, thermal transition in presence of different cooling fields can lead to tunable nonequilibrium coexistence states at low temperature. Such effects can also occur in low temperature field sweep causing a first order transition in presence of disorder. In particular, the non recovery of the CO state for CE-CO systems close to the FM-M phase could be due to hysteresis. However, the lifetime of such states can depend on the kinetics of the transition, which can be blocked even by weak disorder making such trapped states 'longlived' on experimental time scales.

However using the technique that we employed it is difficult to address this issue as the presence of hysteresis and phase separation tendency makes it very difficult to disentangle these effects. Techniques like kinetic Monte Carlo should be employed to study such issues.

Bibliography

[1] G. H. Jonker and J. H. van Santen, Ferromagnetic compounds of Manganese with perovskite structure, Physica (Utrecht), 16: 337-349 (1950).

[2] R. von Helmolt, J. Wecker, B. Holzapfel, L. Schultz and K. Samwer, Phys. Rev. Lett. **71** 2331 (1993).

[3] S. Jin, T. H. Tiefel, M. McCormack, R. A. Fastnacht, R. Ramesh, and L. H. Chen, Science **264**, 413 (1994).

[4] Y. Tokura, A. Urushibara, Y. Moritomo, T. Arima, A. Asamitsu, G. Kido, and N. Furukawa, J. Phys. Soc. Japan **63** 3931 (1994).

[5] S. Fratini, D. Feinberg, and M. Grilli, Eur. Phys. J. B **22** 157 (2001).

[6] S. K. Mishra, Rahul Pandit, and Sashi Satpathy Phys. Rev. B 56, 2316 - 2319 (1997).
Z. Popovic and S. Satpathy, Phys. Rev. Lett. **88**, 197201 (2002).

[7] O. Cepas, H. R. Krishnamurthy and T. V. Ramakrishnan, Phys. Rev. **B 73**, 035218 (2006).

[8] P W Anderson and H Hasegawa, *Phys. Rev.* **100**, 67 (1955).

[9] Q. Li, J. Zang, C. M. Soukoulis, and A. R. Bishop, *Phys. Rev.* **B56**, 4541 (1997).

[10] Jinwu Ye, Yong Baek Kim, A. J. Millis, P. Majumdar, Z. Tesanovic arXiv:cond-mat/9905007

[11] See, e.g, *Colossal Magnetoresistive Oxides, edited by Y. Tokura, Gordon and Breach, Amsterdam* (2000).

[12] J. Inoue and S. Maekawa, *Phys. Rev.* **B74**, Number 17 (1995).

[13] A. J. Millis, *Phys. Rev.* **B55**, Number 10, (1996).

[14] Igor Solovyev and Noriaki Hamada, *Phys. Rev.* **B53**, Number 11 (1996).

[15] T. Saitoh, A. Sekiyama, K. Kobayashi, T. Mizokawa, A. Fujimori, D. D. Sarma, Y. Takeda, and M. Takano, Phys. Rev. **B56**, 8836 (1997).

[16] J. Zaanen, G. A. Sawatzky, and J. W. Allen, Phys. Rev. Lett. **55**, 418 (1985).

[17] Y. Okimoto, T. Katsufuji, T. Ishikawa, A. Urushibara, T. Arima, and Y. Tokura, Phys. Rev. Lett. 75, 109 (1995).

[18] D. D. Sarma, N. Shanthi, S. R. Krishnakumar, T. Saitoh, T. Mizokawa, A. Sekiyama, K. Kobayashi, A. Fujimori, E. Weschke, R. Meier, G. Kaindl, Y. Takeda, and M. Takano, Phys. Rev. B 53, 6873 (1996).

[19] A. Chainani, M. Mathew, and D. D. Sarma, Phys. Rev. B 47, 15 397 (1993) .

[20] C.-H. Park, D. S. Dessau, T. Saitoh, Z.-X. Shen, Y. Moritomo, and Y. Tokura (unpublished).

[21] S. Ishihara, M. Yamanaka, and N. Nagaosa, Phys. Rev.**B 56**, 686 (1997).

[22] J. Kanamori, J. Appl. Phys. Suppl. 31, 145 (1961).

[23] J. B. A. A. Ellemans, B. vanLaar, K. R. vanderVeer, and B. O. Loopstra, J. Solid State Chem. 3, 238 (1971).

[24] A. J. Millis, Boris I. Shraiman, and R. Mueller, Phys. Rev. Lett. 77, 175 - 178 (1996).

[25] P. G. Radaelli, M. Marezio, H. Y. Hwang, S-W. Cheong and B. Batlogg, Phys. Rev. **B 54**, 8992 - 8995 (1996).

[26] J. L. Cohn, J. J. Neumeier, C. P. Popoviciu, K. J. McClellan and Th. Leventouri, Phys. Rev. **B 56**, R8495 - R8498 (1997).

[27] S. Yunoki, A. Moreo, and E. Dagotto, Phys. Rev. Lett. **81**, 5612 - 5615 (1998).
A. J. Millis, et al., Phys. Rev. Lett. **74**, 5144 (1995)
H. Roder, et al., Phys. Rev. Lett. **76**, 1356 (1996).
A. J. Millis, et al., Phys. Rev. **B 54**, 5405 (1996).

[28] J.-H. Park, C. T. Chen, S.-W. Cheong, W. Bao, G. Meigs, V. Chakarian, and Y. U. Idzerda, Phys. Rev. Lett. **76**, 4215 (1996).

[29] Y. Okimoto, T. Katsufuji, T. Ishikawa, A. Urushibara, T. Arima, and Y. Tokura, Phys. Rev. Lett. **75**, 109 (1995).

[30] A. Bocquet, T. Mizokawa, T. Saitoh, H. Namatame, and A. Fujimori, Phys. Rev. **B46**, 3771 (1992).

[31] T. Arima, Y. Tokura, and J. B. Torrance, Phys. Rev. **B 48**, 17006 (1993).

[32] T. Saitoh, A. Bocquet, T. Mizokawa, H. Namatame, A. Fujimori, M. Abbate, Y. Takeda, and M. Takano, Phys. Rev. **B 51**, 13942 (1995).

[33] M. N. Iliev, M. V. Abrashev, H.-G. Lee, Y. Y. Sun, C. Thomsen, R. L. Meng, and C. W. Chu, Phys. Rev. **B 57**, 2872 (1998).

[34] T. G. Perring, G. Aeppli, Y. Tokura, Phys. Rev. Lett. **80**, 4359 (1998).

[35] R. Maezono, S. Ishihara, and N. Nagaosa, Phys. Rev. **B 58**, 11583 (1998).

[36] T. Nakajima, Hiroshi Kageyama, Hideki Yoshizawa and Yutaka Ueda, J. Phys. Soc. Jpn. **71**, 2843 (2002).

[37] Sang-Wook Cheong and Harold Y. Hwang, in *Colossal Magnetoresistive Oxides, edited by Y. Tokura, Gordon and Breach, Amsterdam* (2000).

[38] Y. Yamada, O. Hino, S. Nohdo, and R. Kanao, T. Inami and S. Katano, Phys. Rev. Lett. **77**, 904 (1996).

[39] A. P. Ramirez, P. Schiffer, S-W. Cheong, C. H. Chen, W. Bao, T. T. M. Palstra, P. L. Gammel, D. J. Bishop, and B. Zegarski, Phys. Rev. Lett. **74**, 5108 (1995).

[40] Despina Louca, T. Egami, E. L. Brosha, H. Rder, and A. R. Bishop, Phys. Rev. **B 56**, R8475 - R8478 (1997).

[41] Y. Tomioka and Y. Tokura, Phys. Rev. **B 70**, 014432 (2004).

[42] M. Uehara, S. Mori, C. H. Chen and S. W. Cheong, Nature 399, 560-563 (1999).

[43] E. Dagotto, T. Hotta, A. Moreo, Phys. Rep. 344, 1 (2001).

[44] E. Dagotto, Nanoscale Phase Separation and Colossal Magnetoresistance (Springer-Verlag, Berlin, 2002).

[45] J. Burgy et al., Phys. Rev. Lett. **87**, 277202 (2001).

[46] J. Burgy, A. Moreo, E. Dagotto, Phys. Rev. Lett. **92**, 097202 (2004).

[47] S. Yunoki et al., Phys. Rev. Lett. **80**, 845 (1998).

[48] E. Dagotto, Science, **309**, 257 (2005).

[49] D. Akahoshi, M. Uchida, Y. Tomioka, T. Arima, Y. Matsui and Y. Tokura, Phys. Rev. Lett. **90**, 177203 (2003).

[50] S. Mori, C.H. Chen and S-W. Cheong, Phys. Rev. Lett. **81**, 3792 (1998).

[51] Tokunaga M., Miura N., Tomioka Y. and Tokura Y., Phys. Rev. **B 60**, 6219 (1999).

[52] Sacanell J., Parisi F., Levy P. and Ghivelder L., Physica B 354/1-4, 43-46 (2004).

[53] G. Xiao, E. J. McNiff Jr., G. Q. Gong, A. Gupta, C. L. Canedy and J. Z. Sun, Phys. Rev. **B 54**, 6073 (1996).

[54] R. Mathieu, D. Akahoshi, A. Asamitsu, Y. Tomioka, and Y. Tokura, Phys. Rev. Lett. **93**, 227202 (2004)

[55] W. Wu, C Israel, N. Hur, S. Park, S-W Cheong A. Lozanne, Nat. Mater., **5**, 881, (2006).

[56] A. Trokiner, S. Verkhovskii, A. Yakubovskii, K. Kumagai, P. Monod, K. Mikhalev, A. Buzlukov, Y. Furukawa, N. Hur, and S.-W. Cheong, Phys. Rev. **B 77**, 134436 (2008).

[57] C.H.Chen, S. Mori, and S-W. Cheong, Phys. Rev. Lett. **83**, 4793 (1999)
C.H.Chen and S-W. Cheong, Phys. Rev. Lett. **76**, 4042 (1996).

[58] P. Chaddah, K Kumar, and A. Banerjee, Phys. Rev. **B 77**, 100402 (2008).

[59] K. Kumar, A. K. Pramanik, A. Banerjee, P. Chaddah, S. B. Roy, S. Park, C. L. Zhang, and S.-W. Cheong, Phys. Rev. **B 73**, 184435 (2006).

[60] F. Parisia, and L. Ghivelder, Physica B **398** 184 (2007).

[61] Ghivelder, L. and Parisi, F. Phys. Rev. B 71,184425 (2005).
Sharma, P. A., Kim, S. B., Koo, T. Y., Guha, S. and Cheong, S.-W., Phys. Rev. **B 71**, 224416 (2005).

[62] Wollan, E. O. and Koehler . W. C. *Neutron Diffraction study of the Magnetic Properties of the Series of Perovskite-Type Compounds [$La_{1-x}Ca_xMnO_3$], Phys. Rev.* **100** (1955) 545 - 563.

[63] Jirak Z., Krupčka S., Šimša Z., Dlouha M. and Vratislav S. J. Magn. Magn. Mater. **53** (1985), p. 153-166 *Neutron Diffraction Study of $Pr_{1-x}Ca_xMnO_3$ Perovskites*

[64] Jirák Z., Krupička S., Nekvasil V., Pollert E., Villeneuve G. and Zounová F. *Structural and Magnetization Study of $Pr_{1-x}Ca_xMnO_3$* , J. Solid State Chem. *100* (1992), pp. 292?300.

[65] J.B. Goodenough, Phys. Rev. **100** (1955), p. 564-573 *Theory of the Role of Covalence in the Perovskite-Type Manganites [$La, M(II)$]MnO_3.*

[66] J. van den Brink, G. Khaliullin, and D. Khomskii, Phys. Rev. Lett. **83**, 5118 (1999).

[67] G. Jackeli, N. B. Perkins, and N. M. Plakida, Phys. Rev. B **62**, 372 (2000).

[68] T. Hotta, A.-L. Malvezzi, and E. Dagotto, Phys. Rev. B 62, 9432 (2000).
S. Yunoki, T. Hotta, and E. Dagotto, Phys. Rev. Lett. 84, 3714 (2000).

[69] Tokura Y., Rep. Prog. Phys. **69**, 797 (2006).

[70] Phys. Rev. **100**, 675 (1955).

[71] Z. Jirak, E. Pollert, A. F. Andersen, J. C. Grenier, and P. Hagenmuller, Eur. J. Solid State Inorg. Chem. **27**, 421 (1990)

[72] L. M. Rodriguez-Martinez and J. P. Attfield, Phys. Rev. **B 54**, R15624 (1996).

[73] L. M. Rodriguez-Martinez and J. P. Attfield, Phys. Rev. **B 63,** 024424 (2000),

[74] Y. Tomioka and Y. Tokura , Phys. Rev. **B 70**, 014432 (2004).

[75] Kalpataru Pradhan, Anamitra Mukherjee, Pinaki Majumdar, Phys. Rev. Lett. **99**, 147206 (2007).

[76] Kalpataru Pradhan, Anamitra Mukherjee, Pinaki Majumdar, Europhys. Lett. **84**, 37007 (2008).

[77] Y. Moritomo, A. Machida, S. Mori, N. Yamamoto and A. Nakamura, Phys. Rev. **B 60**, 9220 (1999).

[78] T. Kimura, R. Kumai, Y. Okimoto, Y. Tomioka and Y. Tokura, Phys. Rev. **B 62**, 15021 (2000).

[79] A. Machida, Y. Moritomo, K. Ohoyama, T. Katsufuji, and A. Nakamura, Phys. Rev. **B 65**, 064435 (2002).

[80] K. H. Ahn, X. W. Wu, K. Liand C. L. Chien, J. Appl Phys. **81**, 5505 (1997).

[81] H. Sakai, K. Ito, T. Nishiyama, X. Yu, Y. Matsui, S. Miyasaka and Y. Tokura, J. Phys. Soc. Jpn. 77, 124712 (2008).

[82] A. Maignan and B. Raveau, Z. Phys. B 102, 299 (1997).

[83] H. Kuwahara, Y. Tomioka, A. Asamitsu, Y. Moritomo, Y. Tokura, Science **270**, 961 (1995).
Y. Tomioka, A. Asamitsu, Y. Moritomo, H. Kuwahara, and Y. Tokura, Phys. Rev. Lett. **74**, 5108 (1995).

[84] M. Respaud, A. Llobet, C. Frontera, C. Ritter, J. M. Broto, H. Rakoto, M. Goiran, and J. L. Garcia-Munoz, Phys. Rev.**B 61**, 9014 (2000).

[85] Y. Tokura, H. Kuwahara, Y. Moritomo, Y. Tomioka, and A. Asamitsu, Phys. Rev. Lett. **76**, 3184 (1996).
M. Kawano, R. Kajimoto, H. Yoshizawa, Y. Tomioka, H. Kuwahara, and Y. Tokura, Phys. Rev. Lett. **78**, 4253 (1997).
H. Kuwahara, Y. Moritomo, Y. Tomioka, A. Asamitsu, M. Kasai, R. Kumai, and Y. Tokura, Phys. Rev. **B 56**, 9386 (1997).

[86] A. Kirste, M. Goiran, M. Respaud, J. Vanaken, J. M. Broto, H. Rakoto, M. von Ortenberg, C. Frontera, and J. L. Garcia-Munoz, Phys. Rev. **B 67**, 134413 (2003).

[87] J. C. Slater and G. F. Koster, Phys. Rev. **94**, 1498 (1954).

[88] J. Kanamori, J. Appl. Phys. Suppl. **31**, 14S (1960).

[89] Sanjeev Kumar and Arno P. Kampf, Phys. Rev. Lett. **100**, 076406 (2008).

[90] See, T. Hotta and E. Dagotto, in *Colossal Magnetoresistive Manganites, edited by T. Chatterji, Kluwer Academic Publishers, Dordrecht, Netherlands (2002),*

[91] G.M. Zhao, K. Conder, H. Keller, and K.A. Muller, Nature London **381**, 676 1996.
A.J. Millis, P.B. Littlewood, and B.I. Shraiman, Phys. Rev. Lett. 74, 5144 (1995).

[92] N. D. Mermin and H. Wagner, Phys. Rev. Lett. **17**, 1133 (1966).

[93] Y. Imry and S-K Ma, Phys. Rev. Lett. **35**, 1399 (1975).

[94] M Grant and J. D. Gunton Phys. Rev. **B 29**, 6266 (1984). (and references there in)

[95] S. Kumar and P. Majumdar, Eur. Phys. J. **B 50**, 571 (2006).

[96] S. Kumar and P. Majumdar, Eur. Phys. J. B, **46**, 237 (2005).

[97] K. Pradhan, A. Mukherjee and P. Majumdar, Phys. Rev. Lett. **99**, 147206 (2007).

[98] J. van den Brink *et al.*, Phys. Rev. Lett. **83**, 5118 (1999).

[99] L. Brey, Phys. Rev. **B 71**, 174426 (2005).

[100] O. Cepas *et al.*, Phys. Rev. Lett. **94**, 247207 (2005).

[101] S. Dong, *et al.*, Phys. Rev. **B 73**, 104404 (2006).

[102] S. Yunoki, *et al.*, Phys. Rev. Lett. **84**, 3714-3717 (2000).

[103] Adriana Moreo, *et al.*, Phys. Rev. Lett. **84**, 5568 (2000).

[104] S. Kumar and P. Majumdar, Phys. Rev. Lett. **92**, 126602 (2004).

[105] Sacanell J., Parisi F., Levy P. and Ghivelder L., Physica B 354/1-4, 43-46 (2004).

[106] Tokunaga M., Miura N., Tomioka Y. and Tokura Y., Phys. Rev **B 60**, 6219 (1999).

[107] G. C. Milward, M. J. Calderon and P. B. Littlewood, Nature 433, 607 (2005).

[108] A. Mukherjee and P. Majumdar, preprint, arXiv 0811.3563.

[109] A. Mukherjee, K. Pradhan and P. Majumdar, preprint, Europhys.Lett. **86** 27003 (2009).

[110] E. T. Seppala, *et al.*, Phys. Rev. **E 63**, 066109 (2001).